Thermodynamic Tuning of Lithium Borohydride Using Various Metallic Sources

by Oliver Deavin, MChem

Thesis submitted to The University of Nottingham

for the degree of Doctor of Philosophy, August 2017

The University of Nottingham

Contents

List of Figures **8**

Abstract **19**

Acknowledgements **20**

1 Introduction **22**

1.1 Fossil Fuel Domination 22

1.2 Renewables 24

1.3 Hydrogen 26

1.3.1 Fuel Cells 26

1.3.2 Hydrogen and Transport 28

1.3.2.1 Compressed Hydrogen 29

1.3.2.2 Liquid Hydrogen 31

1.3.2.3 Hydrogen Physisorption 32

1.3.2.4 Chemical Storage 33

1.3.3 Hydrogen Storage Comparison 35

1.4 Research Aims and Objectives 37

1.5 Thesis Overview 38

2 Literature Review **40**

2.1 Introduction 40

2.2 Lithium Borohydride 41

2.3 Thermodynamic Tuning 43

2.3.1 Metal Addition 44

2.3.1.1 Aluminium 44

2.3.1.2 Transition Metals 46

2.3.2 Intermetallic Addition 47

2.3.2.1 Calcium Nickel Alloy 47

2.3.2.2 Magnesium Nickel Hydride 48

2.3.3 Metal Chloride Addition 49

2.3.4 Metal Oxide Addition 51

2.3.4.1 Silicon Oxide 51

2.3.4.2 Titanium Dioxide 53

2.3.4.3 Other Oxides 54

2.3.5 Binary Hydrides 55

2.3.5.1 Magnesium Hydride 55

2.3.5.2 Calcium Hydride 56

2.3.5.3 Other Systems 58

2.3.6 Complex Hydride Addition 60

2.3.6.1 Alanate Addition 60

2.3.6.2 Amide Addition 64

2.4 Kinetic Improvements 66

2.4.1 Ball-Milling 66

2.4.2 Catalysis 67

2.4.2.1 Platinum Group Metals 68

2.4.2.2 Nickel 70

2.4.2.3 Niobium 72

2.5 Confinement of Lithium Borohydride 74

2.6 Summary 77

3 Methodology **80**

3.1 Introduction 80

3.2 Sample Preperation 81

3.3 Sample Characterisation 83

3.3.1 Thermal Analysis 83

3.3.1.1 Differential Scanning Calorimetry(DSC) 83

3.3.1.2 Thermogravimetric Analysis (TGA) 85

3.3.2 Structural Analysis 87

3.3.2.1 X-Ray Diffraction 87

3.3.2.2 Neutron Diffraction 89

3.3.2.3 Fourier Transfer Infra-Red Spectroscopy 91

3.3.3 Hydrogen Uptake Analysis 93

3.3.4 Scanning Electron Microscopy Analysis 96

4 Results **98**

4.1 Lithium Borohydride As-received 98

4.2 Lithium borohydride and nickel systems 101

4.2.1 Introduction 101

4.2.2 Use of Calcium Nickel Alloy 102

4.2.3 Use of Nickel 105

4.2.3.1 As-received Materials 105

4.2.3.2 Varying Nickel Content 105

4.2.3.3 Focus on 2Ni system 113

4.3 Lithium Borohydride and Silicon Systems 127

4.3.1 Introduction 127

4.3.2 As-received materials 127

4.3.3 Reaction Between Silicon and Boron 127

4.3.3.1 One Hour Ball-Milling 127

4.3.3.2 Four Hours Ball-Milling 130

4.3.3.3 Five Hours Ball-Milling 134

4.3.4 Effect of Titanium Catalyst on $LiBH_4$:xSi System 137

4.4 Lithium Borohydride and Iron/Cobalt Systems 142

4.4.1 Introduction 142

4.4.2 As-received Materials 142

4.4.3 Use of Iron 142

4.4.4 Use of Cobalt 147

5 Discussion **151**

5.1 Lithium Borohydride and Nickel Systems 151

5.1.1 Introduction 151

5.1.2 Varying Nickel Content 153

5.1.3 Focus on the $LiBH_4$:2Ni System 157

5.1.4 Reversibility 164

5.1.5 Thermodynamic Assessment 167

5.1.6 Summary 168

5.2 Lithium Borohydride and Silicon 171

5.2.1 Introduction 171

5.2.2 Reaction Between Silicon and Boron 174

5.2.3 Affect of Titanium Catalyst on reaction between $LiBH_4$ and Silicon 181

5.2.4 Summary 184

5.3 Lithium Borohydride and Iron/Cobalt 185

5.3.1 Introduction 185

5.3.2 Decompostion Using Iron and Cobalt 187

5.3.3 Summary 196

5.4 Overall Summary 197

6 Conclusions **199**

6.1 Nickel Addition 199

6.2 Silicon Addition 200

6.3 Iron and Cobalt Addition 201

6.4 Final Conclusions 202

7 Future Work **203**

Bibliography **206**

List of Figures

1.1 Schematic showing the energy mix of the world compared to the UK in 2015. [1] 22

1.2 Schematic showing the uptake of PV panels following the introduction of the FiT schemes [7]. 25

1.3 Different types of fuel cells and their operating conditions [10]. 27

1.4 Break down of the costs for each component in a compressed hydrogen storage cannister with 80% of the cost for the 700 bar system coming from the carbon fibre composite. [19]. 30

2.1 Enthalpy diagram demonstrating the lowering of a hydrides decomposition enthalpy upon reaction with a secondary component. [45] . . 43

2.2 *In-situ* PND data showing the full decomposition of $LiBD_4$ using the $CaNi_5$ at 192 °C. This is followed by the partial regeneration of $LiBD_4$ under 80 bar of D_2 [55] 48

2.3 TGA decomposition curves for three different $LiBH_4$-SiO_2-TiF_3 systems. [65] 52

2.4 Hydrogen uptake curves of the $6LiBH_4$-CaH_2 (5 wt% NbF_5) system at different temperatures showing the fastest uptake at 450 °C. [79] . 58

2.5 Formation of an AlB_2 shell prevents the formation of LiAl and allows for easier regeneration of $LiBH_4$ [48] 62

3.1 Scheme showing the heat flux type DSC used. [136] 84

3.2 Scheme showing the isolated balance away from the sample in the furnace in the TGA. [137]. 86

3.3 Schematic showing the scattering of X-rays by atoms in a crystal structure. Amended from [138]. 88

3.4 Schematic showing layout of the D1B instrument used for neutron diffraction experiments [140]. 90

3.5 Schematic showing the collection of IR radiation produced during DRIFTS. Amended from [143]. 92

3.6 Schematic showing the basic set up of a Sieverts apparatus. [144] . . . 94

3.7 Schematic showing a stylised PCI plot where A is the plateau pressure of the hydrogen storage material. [45] 94

3.8 Schematic showing the formation of a van't Hoff plot. [146] 95

4.1 FTIR data for as-received $LiBH_4$. 99

4.2 XRD data for as-received $LiBH_4$. 99

4.3 TGA and DSC data for as-received $LiBH_4$ heated to 585°C at 10 °C min^{-1}. 100

4.4 TGA and DSC data for the $2LiBH_4$:$CaNi_5$ system heated to 585°C at 10 °C min^{-1}. Dotted box indicates all decomposition occurring below 300°C. 102

4.5 TGA and DSC data for the as-received $LiBH_4$ and $2LiBH_4$:$CaNi_5$ systems heated to 585°C at 10 °C min^{-1}. TGA data has been converted from mass loss to percentage of hydrogen liberated from system to more easily compare two systems. 104

4.6 PND data for the $2LiBD_4$:$CaNi_5$ system. 104

4.7 XRD data for as-received micro-scale nickel and nano-scale nickel. . . 105

4.8 XRD data for the four different nickel containing systems post-milling. 106

4.9 DSC data for the four different nickel containing systems heated to 585°C at 10 °C min^{-1}. 107

4.10 TGA data for the four different nickel containing systems heated to 585°C at 10 °C min^{-1}. Dotted box indicates all decomposition occurring below 300°C. 108

4.11 *Ex-situ* XRD data for the Ni system showing different stages of the system's decomposition. 109

4.12 *Ex-situ* XRD data for the 2Ni system showing different stages of the system's decomposition. 110

4.13 *Ex-situ* XRD data for the 2.5Ni system showing different stages of the system's decomposition. 111

4.14 *Ex-situ* XRD data for the 3Ni system showing different stages of the system's decomposition. 112

4.15 FTIR data for the four systems post decomposition up to 585 °C. Dotted lines show any phase shifting of species. 113

4.16 DSC and TGA data for the $LiBH_4$:2Ni system heated to 585°C at 10 °C min^{-1} under flowing argon and flowing hydrogen gases. 114

4.17 SEM data for the $LiBH_4$:2Ni system using (A) micro-scale and (B) nano-scale nickel precursors. 114

4.18 DSC data for the $LiBH_4$:2Ni system using micro-scale and nano-scale nickel precursors heated to 585°C at 10 °C min^{-1}. 115

4.19 SEM data for the as-milled $LiBH_4$:2Ni system. EDX analysis was also performed for site 1 (A) and site 2 (B). 116

4.20 SEM data for the decomposed up to 585 °C $LiBH_4$:2Ni system. EDX analysis was also performed for site 1 (A) and site 2 (B). 117

4.21 *In-situ* PND data for the $LiBD_4$:2Ni system system upon heating to 300°C. 118

4.22 *In-situ* PND data for the $LiBD_4$:2Ni system upon heating to 300°C. . 119

4.23 Integrated peak areas for species for the $LiBD_4$:2Ni system observed during PND experiments upon heating to 300°C. 120

4.24 Selected PND plots for the $LiBD_4$:2Ni system demonstrating (A) the melting of the $LiBD_4$ at 260 °C and (B) the crystallisation of nickel borides from an amorphous region at the same temperature. 121

4.25 Isothermal decomposition data for the $LiBH_4$:2Ni system carried out on the TGA with an initial 30 $°C^{-1}$ ramp rate followed by the isothermal decomposition at the desired temperature. 122

4.26 FTIR spectra for the $LiBH_4$:2Ni system after isothermal experiments at different temperatures. Dotted lines show any phase shifting of species. 123

4.27 XRD data for the $LiBH_4$:2Ni system after isothermal experiments at different temperatures. 124

4.28 Hydrogenation isotherms for the $LiBH_4$:2Ni system at 200, 225 and 250 °C. 124

4.29 Post-hydrogenation TGA data for the $LiBH_4$:2Ni system at 200, 225 and 250 °C compared against the as-milled system. Samples were heated to 585 °C at 10 °C min^{-1}. Black dotted box shows decomposition up to 300°C and red dotted box shows decomposition up to 320°C. 125

4.30 Post-hydrogenation FTIR data for the $LiBH_4$:2Ni system at 200, 225 and 250 °C compared against the as-milled system. Dotted lines show any phase shifting of species. 126

4.31 XRD data of as-received silicon powder. 128

4.32 XRD data of as-received titanium fluoride powder. 128

4.33 XRD data for the 1 hour ball-milled 6$LiBH_4$:Si. 129

4.34 DSC and TGA data for the 1 hour ball-milled 6$LiBH_4$:Si system heated to 585°C at 10 °C min^{-1}. Dotted box indicates decomposition occurring within the solid-state. 129

4.35 XRD data for the four hour ball-milled 6$LiBH_4$:Si, 3$LiBH_4$:Si and $LiBH_4$:Si systems. 131

4.36 DSC and TGA data for the four hour ball-milled 6$LiBH_4$:Si system heated to 585°C at 10 °C min^{-1}. Dotted box indicates decomposition occurring within the solid-state. 131

4.37 DSC and TGA data for the four hour ball-milled $3LiBH_4$:Si system heated to 585°C at 10 °C min^{-1}. Dotted box indicates decomposition occurring within the solid-state. 132

4.38 DSC and TGA data for the four hour ball-milled $LiBH_4$:Si system heated to 585°C at 10 °C min^{-1}. Dotted box indicates decomposition occurring within the solid-state. 133

4.39 XRD data for the five hour total ball-milled $6LiBH_4$:Si and $3LiBH_4$:Si systems. 134

4.40 DSC and TGA data for the five hour total ball-milled $6LiBH_4$:Si system heated to 585°C at 10 °C min^{-1}. Dotted box indicates decomposition occurring within the solid-state. 135

4.41 DSC and TGA data for the five hour ball-milled $3LiBH_4$:Si system heated to 585°C at 10 °C min^{-1}. Dotted box indicates decomposition occurring within the solid-state. 136

4.42 XRD data for the five hour ball-milled $4.4LiBH_4$:Si system with 10, 20 and 30% by mass added TiF_3. 137

4.43 DSC and TGA data for the five hour ball-milled $4.4LiBH_4$:Si system with 10% TiF_3 by mass heated to 585°C at 10 °C min^{-1}. Dotted box indicates decomposition occurring within the solid-state. 138

4.44 DSC and TGA data for the five hour ball-milled 4.4$LiBH_4$:Si system with 20% TiF_3 by mass heated to 585°C at 10 °C min^{-1}. Dotted box indicates decomposition occurring within the solid-state. 139

4.45 DSC and TGA data for the five hour ball-milled 4.4$LiBH_4$:Si system with 30% TiF_3 by mass heated to 585°C at 10 °C min^{-1}. Dotted box indicates decomposition occurring within the solid-state. 140

4.46 XRD data for the five hour ball-milled 4.4$LiBH_4$:Si system with 20 and 30% by mass added TiF_3 after heating to 585 °C. 141

4.47 XRD data for as-received cobalt and iron. 143

4.48 XRD data for as-milled $LiBH_4$:2Fe and $LiBH_4$:Fe systems milled for 3 hours. 143

4.49 DSC and TGA data for the $LiBH_4$:Fe system heated to 585°C at 10 °C min^{-1}. Dotted box indicates all decomposition occurring below 300°C. 144

4.50 DSC and TGA data for the $LiBH_4$:2Fe system heated to 585°C at 10 °C min^{-1}. Dotted box indicates all decomposition occurring below 300°C. 145

4.51 XRD data for the $LiBH_4$:2Fe and $LiBH_4$:Fe systems decomposed up to 585 °C. 146

4.52 XRD data for as-milled $LiBH_4$:2Co and $LiBH_4$:Co systems milled for 3 hours. 147

4.53 DSC and TGA data for the $LiBH_4$:Co system heated to 585°C at 10 °C min^{-1}. Dotted box indicates all decomposition occurring below 300°C. 148

4.54 DSC and TGA data for the $LiBH_4$:2Co system heated to 585°C at 10 °C min^{-1}. Dotted box indicates all decomposition occurring below 300°C. 149

4.55 XRD data for the decomposed, up to 585 °C, $LiBH_4$:2Co and $LiBH_4$:Co systems. 150

5.1 Phase diagram for the boron-nickel system. [149]. 152

5.2 DSC and TGA data for the four nickel systems studied. 155

5.3 XRD data for the four nickel systems studied. A - $LiBH_4$:Ni B - $LiBH_4$:2Ni C - $LiBH_4$:2.5Ni C - $LiBH_4$:3Ni 156

5.4 PND data for the $LiBD_4$:2Ni system. A - Waterfall Plot B - Superplot C - Integrated peaks plot D - Amorphous Region Analysis 161

5.5 Low temperature data for the $LiBD_4$:2Ni system. A - Isothermal decomposition profiles B - FTIR data C - XRD data. 163

5.6 Reversibility data for the $LiBD_4$:2Ni system. A - PCI plots B - TGA data C - FTIR data. 166

5.7 Enthalpy and entropy diagram for the $LiBH_4$:2Ni system using data from Price *et al.* and Teppa *et al.* [72, 151]. 167

5.8 Phase diagram for the boron-silicon system. [154]. 171

5.9 Phase diagram for the Li-Si system [155]. 173

5.10 Data for the four hour ball-milled $LiBH_4$:xSi systems. A - XRD B - $LiBH_4$:6Si TGA/DSC C - $LiBH_4$:3Si TGA/DSC- D - $LiBH_4$:Si TGA/DSC. 175

5.11 Data for the five hour ball-milled $LiBH_4$:xSi systems. A - XRD B - $LiBH_4$:6Si TGA/DSC C - $LiBH_4$:3Si TGA/DSC. 177

5.12 Enthalpy and entropy diagram for the 6$LiBH_4$:Si system using data from Price *et al.* and Domalski *et al.* [164, 167]. 180

5.13 Data for the 4.4$LiBH_4$:Si:x wt% TiF_3 catalyst systems. A - 4.4$LiBH_4$:Si:10 wt% TiF_3 DSC/TGA B - 4.4$LiBH_4$:Si:20 wt% TiF_3 DSC/TGA C - 4.4$LiBH_4$:Si:30 wt% TiF_3 DSC/TGA D - XRD data for the 20 and 30 wt% TiF_3 systems. 183

5.14 Phase diagram for the boron-iron system. [168] 186

5.15 Phase diagram for the boron-cobalt system. [169] 187

5.16 TGA/DSC data for the $LiBH_4$:Fe and $LiBH_4$:2Fe systems. A - $LiBH_4$:Fe B - $LiBH_4$:2Fe. 189

5.17 TGA/DSC data for the $LiBH_4$:Co and $LiBH_4$:2Co systems. A - $LiBH_4$:Co B - $LiBH_4$:2Co 191

5.18 XRD data for the iron and cobalt systems. A - $LiBH_4$:Fe & $LiBH_4$:2Fe B - $LiBH_4$:Co & $LiBH_4$:2Co. 193

Abstract

Lithium borohydride ($LiBH_4$) has been shown great interest as a hydrogen storage material owing to its large hydrogen storage capacity of 18.5 wt%, but unfortunately to release the vast majority of the stored hydrogen requires temperatures in excess of 600 °C. To improve the temperature at which $LiBH_4$ decomposes, and to improve its poor reversibility, a process known as thermodynamic tuning can be used. Thermodynamic tuning involves creating new, more favourable reaction pathways and in this work the addition of nickel, silicon, iron and cobalt were investigated.

The addition of nickel in the $LiBH_4$:2Ni system was shown to be the most effective in reducing the decomposition temperature to occur below 300 °C while also improving reversibility to occur in the solid state at temperatures of 250 °C or lower.

The addition of silicon was found to not be effective in reducing the decomposition temperature of $LiBH_4$ even though it was thermodynamically predicted to do so. Attempts to improve the kinetics of the system with a titanium catalyst only showed an improvement when large quantities of the catalyst were used implying that the reaction with the catalyst was the driving force.

Addition of both cobalt and iron were also affective in reducing the temperature of $LiBH_4$ decomposition, in a similar reaction to the nickel systems by forming borides. The mass loss in the solid state (<300 °C) was, however, inferior to the addition of nickel.

Acknowledgements

I would like to thank my supervisors Prof. Gavin Walker and Prof. David Grant for their support in allowing me to carry out the research presented in this work.

I would also like to thank all of the technicians that assisted in my research especially Tom Buss for general support and Dr Nigel Neate for all his assistance with using all aspects of the XRD.

I would especially like to thank my friends and colleagues Dr Andrew Patman, Dr Priyen Mistry, Dr Christopher Bennett, Dr Alastair Stuart, Dr Kandavel Manickam, Gulucan Serdaroglu and Alexander Lamond for their friendship and assistance throughout my PhD studies.

Lastly I would like to show deepest thanks to my wife Megan and our new son Alexander. Megan showed me constant support and love throughout my studies and the arrival of Alexander is what inspired me to finally finish my thesis.

Chapter 1

Introduction

1.1 Fossil Fuel Domination

A growing concern for world energy production is that dwindling oil reserves will eventually run out. This, coupled with climate change concerns from CO_2 emis-

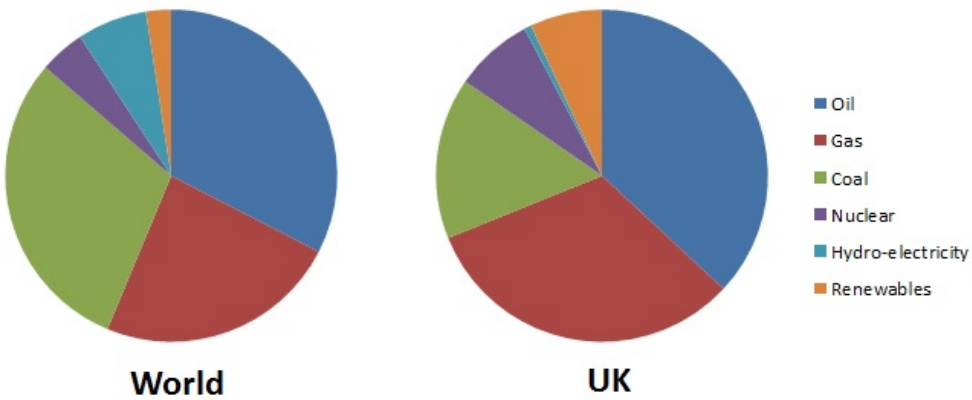

Figure 1.1: Schematic showing the energy mix of the world compared to the UK in 2015. [1]

Table 1.1: Climate Change Act Targets [2].

Budget Period	% Reduction on Emissions
1st Budget (2008-2012)	23%
2nd Budget (2013-2017)	29%
3rd Budget (2018-2022)	35% by 2020
4th Budget (2023-2027)	50% by 2025

sions, has encouraged many governments to seek out alternative and environmentally friendly methods of producing and storing energy. Currently over 86% of the world's energy supply comes from fossil fuels which means significant changes need to be made to phase out these technologies and replace them. The UK is slightly below the global average at 84.5% fossil fuel usage [1], figure 1.1, but the government has set targets to reduce greenhouse gas emissions by 80% by 2050.

The main driver for the UK's reduction is carbon emissions comes from the Climate Change Act, introduced in 2008, which established a framework for a credible carbon emissions reduction path [2]. This pathway is laid out with four carbon budget periods in which a reduction is measured versus 1990 levels and is summarised in Table 1.1. To meet these targets, new technologies must be exploited and these include renewables, CCS, nuclear and bioenergy. Renewables are seen as the preferred option for many people owing to their perception as a clean energy source.

1.2 Renewables

In 2011 the UK government pledged to deliver at least 15% of the UK's energy mix as renewables by 2020, with the Scottish government providing more ambition by targeting 100% renewable electricity in the same period [3]. The government is running the risk of not meeting these renewable targets by reducing incentives to build renewables such as cutting the feed-in tariffs. The UK did fall short of targets in 2010 by only providing 7.4% of electricity using renewables compared to its target of 9% and this shortfall in renewables targets is attributed to poor wind conditions in 2010 [4]. By 2012, however, the UK had become the world leader in deploying offshore wind power generation [5] which is explained by a change in government policy that encouraged its deployment. The Crown Estate also granted additional planning permission for the development of offshore wind to generate revenue for the government [6].

Another recognisable renewable technology is photovoltaics (PV). Unlike wind power, PV installations tend be decentralised and fitted to domestic properties. This method became extremely popular with the public owing to the feed-in-tariff scheme developed by the government, in which a household is paid for the electricity they generate using renewables installed on their property surplus to their own usage. Feed-in-tariffs (FiT) financially benefit an owner in three ways: a) a generation tariff in which the owner is paid for the generation of the electricity b) an export tariff in which the owner is paid for exporting electricity back into the grid and c) savings

on their electricity bill when they are using the electricity from their renewables rather than from the grid [8]. Before FiT schemes were introduced in 2010 the UK only produced 32 MW of electricity from photovoltaics but within a year 28,550 installations of new PV-panels had been installed which corresponded to 77.7 MW of electricity generation. By the end of 2011 the total installations had increased further still to 102,022 and was estimated to be generating 366 MW of power, a ten fold increase before the FiT scheme was introduced [7]. This is shown in figure 1.2.

While uptake of renewables is on the rise their primary drawback is their intermittent nature in that wind is not always blowing and PV panels only work during the day. The period in which these technologies are operating at their peak efficiency does not always correspond with peak demand for electricity, which is why wind turbine operators are being more frequently paid to keep them switched off. One way of

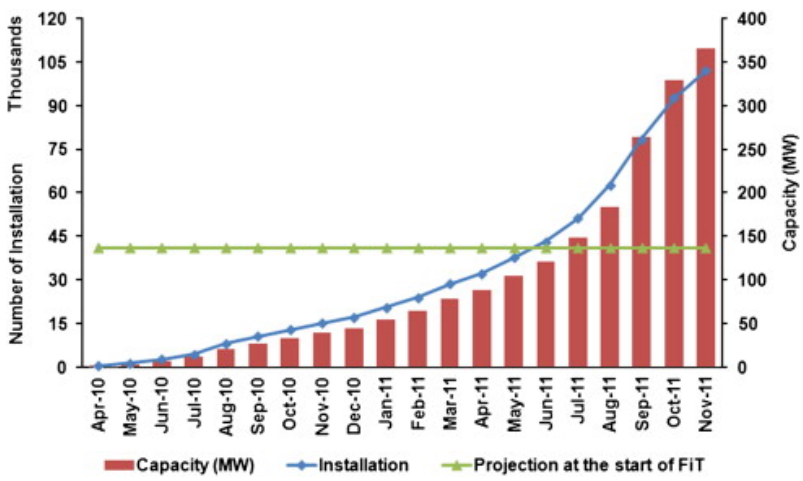

Figure 1.2: Schematic showing the uptake of PV panels following the introduction of the FiT schemes [7].

preventing this waste of electricity would be to store it and one technology that could accommodate this large scale storage would be the generation of hydrogen.

1.3 Hydrogen

Hydrogen is seen as one of the technologies which could one day make fossil fuels obsolete. Hydrogen is one of the most energy dense fuels and, unlike fossil fuels, it does not produce any CO_2 while generating energy. However, using a method such as steam-reforming to generate the hydrogen does result in the formation of CO_2. There are several methods for generating electricity from hydrogen but the most promising is the use of fuel cells.

1.3.1 Fuel Cells

A fuel cell is a device which can convert the chemical energy of a fuel into electricity by reacting hydrogen with an oxidising agent, most commonly oxygen. Unlike internal combustion engines, fuel cells are extremely efficient with typical efficiencies reaching 60% or even over 70% if the waste heat is utilised in systems such as combined heat and power units [9]. There are currently several types of fuel cell in development including: solid-oxide fuel cell (SOFC), molten-carbonate fuel cell (MCFC), phosphoric-acid fuel cell (PAFC), polymer-electrolyte membrane fuel cell (PEMFC) and alkaline fuel cell (AFC). The operating conditions for each of these

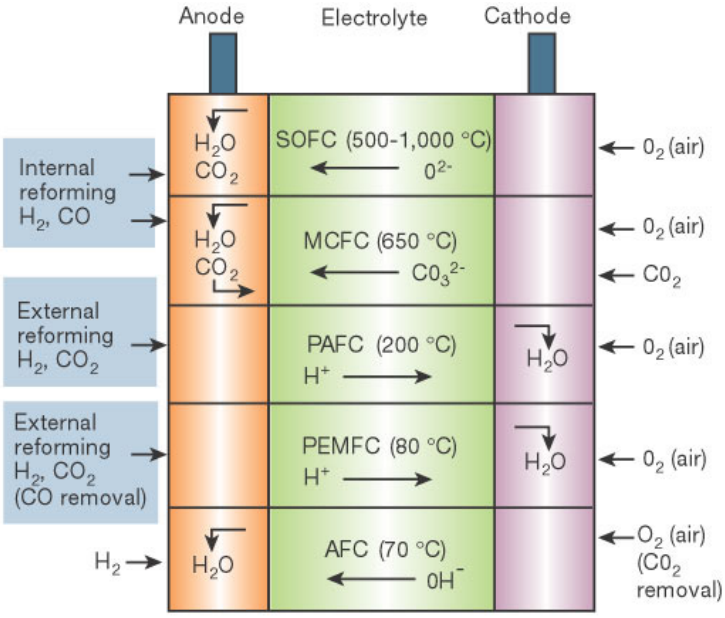

Figure 1.3: Different types of fuel cells and their operating conditions [10].

is presented in figure 1.3.

The solid oxide fuel cell has a characteristic ceramic electrolyte which is a metallic oxide. At the cathode O_2 molecules are reduced to O^{2-} ions which then move through the electrolyte to react with H_2 and CO at the cathode to form H_2O and CO_2. These fuel cells are typically operated at 800-1000°C, to overcome the electrical resistivity of the electrolyte, but there is currently research into reducing this to save money and use a wider variety of fuels [11].

Another high temperature fuel cell used is the molten carbonate fuel cell. This fuel cell operates at around 650°C and transports carbonate ions through an electrolyte that is composed of both lithium and sodium carbonate salts which liquefy at high

temperatures. The use of a liquid electrolyte provides a lower resistivity and better conductivity than that of the solid SOFC electrolytes [12].

Alkaline fuel cells were the first type ever developed and the only low temperature fuel cell to conduct ions rather than protons and operate at around 70°C. This fuel cell uses a potassium hydroxide solution to transport hydroxide ions (OH^-) which are formed at the cathode. Low CO_2 oxygen feedstock is required for this fuel cell otherwise carbonates form in the electrolyte, precipitate out and reduce the number of available hydroxyl ions and thus the conductivity [13, 14].

Phosphoric acid fuel cells, unlike previous fuel cells, conduct protons across the electrolyte rather than as an ion and must be operated at 150-200°C [15].

The final type of fuel cell, and the most well known is the polymer electrolyte membrane fuel cell which operates between 80-100°C to maximise fuel cell efficiency while preventing membrane dehydration. Typically this type of fuel cell uses a sulphated polymer that contains negatively charged sulphate ions that facilitate the conduction of positively charged protons [16].

1.3.2 Hydrogen and Transport

Fuel cell technology is rapidly becoming mature with the first cars using the technology coming to market in 2017 such as the Honda Clarity and Toyota Mira. However, one of the major issues for long term implementation of fuel cells within vehicles is

Table 1.2: DOE targets for mobile storage of hydrogen [18].

System Parameter	2020 Target	2025 Target	Ultimate Target
Gravimetric Capacity (wt%)	4.5	5.5	6.5
Volumetric Capacity ($g_{(H_2)}L^{-1}$)	30	40	50
Operational Cycles	1500	1500	1500
Max Operating Temperature (°C)	85	85	85

the difficulty of storing H_2 in quantities that give fuel cell vehicles comparable range to that of a traditional hydrocarbon/internal combustion engine vehicle. The main driver for hydrogen storage research are the targets set by the United States Department of Energy (DOE), in 2009 and updated in 2017, which include step-wise goals for 2020, 2025 and an ultimate goal [17]. These targets are summarised in table 1.2. There are currently several different technologies competing to be the state-of-the-art hydrogen storage technology including compressed, liquefied, physisorption and chemically bound hydrogen.

1.3.2.1 Compressed Hydrogen

Compressed storage is the most mature of all the hydrogen storage technologies and is the most widely used in both stationary and mobile applications. With compressed storage the hydrogen is pressurised between 350 and 700 bar and stored

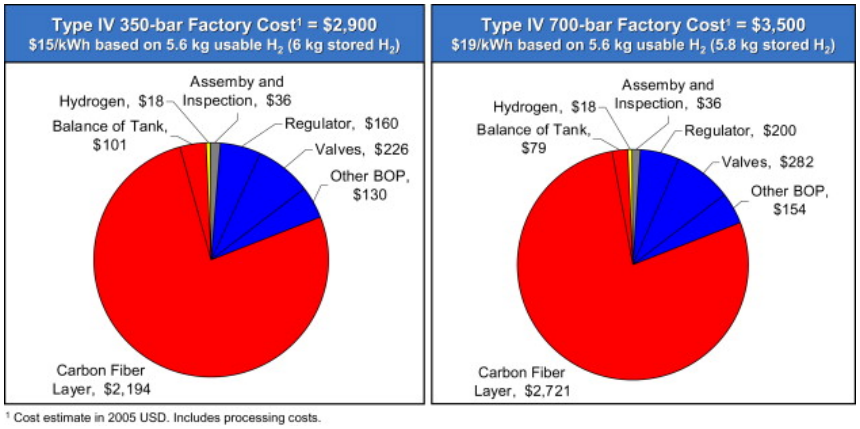

Figure 1.4: Break down of the costs for each component in a compressed hydrogen storage cannister with 80% of the cost for the 700 bar system coming from the carbon fibre composite. [19].

in canisters. The canisters used consist of a high density polyethylene liner wrapped in carbon fibre composites which give excellent mechanical properties, on a par with metals, while being lighter. This reduction means that a typical tank can now store 5.6kg of usable hydrogen which, for a 350 bar system, translates to a weight capacity of 5.5wt% (5.2wt% for a 700 bar system) and a volumetric capacity of 17.6 $g_{(H_2)}L^{-1}$ (26.3 $g_{(H_2)}L^{-1}$ for a 700 bar system). This means that compressed storage can meet the 2017 gravimetric storage capacity target but fail to meet the volumetric capacity targets. While considerably lighter than steel used in previous generations, the carbon fibre cannisters now employed are much more expensive with the carbon fibre taking up to 80% of the system cost, see figure 1.4. This means that compressed hydrogen storage is also one of the most expensive of all hydrogen storage technologies with costs of up to \$27 kWh^{-1} [19].

Another concern with compressed hydrogen storage is the safety of the technology. The perceived risk of compressed hydrogen storage is the high risk of explosion and fire, mostly owing to the historic Hindenburg disaster, but in reality the technology is safer than petrol or diesel [20]. The reason that hydrogen is considered safer is that, unlike diesel or petrol, when a leak occurs in the store the hydrogen is dispersed into its surroundings almost immediately. However, with petrol and diesel cars the fuel lingers and produces a greater radiant heat causing damage to both the car and passengers [21].

1.3.2.2 Liquid Hydrogen

Although historically used for fuelling rockets, liquid hydrogen has more recently been considered for on-board hydrogen storage in vehicles as well. This technology relies upon cooling hydrogen to lower than 21.2 K so that it condenses out of the gas phase and forms a liquid. The main benefit of liquid storage over compressed storage is that it has almost double the volumetric density of compressed storage at 700 bar, 70.8 $_{(H_2)}L^{-1}$, and can operate at ambient pressures [22]. Liquid hydrogen is also considerably cheaper than compressed storage with a price of \$8 kWh^{-1} [23].

The downside to liquid hydrogen storage, however, are its large energy penalties. The first energy loss is from the cooling of the hydrogen to cryogenic temperatures in which 30% of the stored hydrogen energy is lost. The biggest energy loss, however, comes from the boil-off of the hydrogen. This boil-off arises from outside heat which

causes the hydrogen to evaporate and escapes from the storage tank. This boil-off effect contributes up to another 40% energy loss. Due to the 70% energy penalty research into liquid hydrogen storage has all but ended [24].

1.3.2.3 Hydrogen Physisorption

Another method for storing hydrogen is to physically bind it to a surface. To ensure that the weak van der Waal's forces binding the diatomic hydrogen to the surface are not overcome, low temperatures are needed (typically 77 K) although not as low as liquid hydrogen storage (below 33 K). Metal-organic frameworks (MOFs) have increasingly become the most popular medium for this type of storage alongside porous carbon which is the cheaper of the two technologies. MOFs are a class of material which are a crystalline solid, consisting of linking units, that can be modified by organic synthesis and have a large porosity resulting in a high surface area [25]. The synthesis of MOFs results in them being pure and is performed using a one-pot, solvothermal method under mild conditions. The resultant surface area for MOFs has been found to be greater than 1000 m^2g^{-1}, larger than that of zeolites, with values of 3000 m^2g^{-1} causing the greatest excitement [26].

To make MOFs as effective as possible and overcome the weak binding energies, certain properties need to be manipulated. Ideally a MOF would operate at 298 K and to do so it would need an absorption enthalpy of 13.6 kJ mol^{-1}. Pore size of the materials is also important, with 7 Å the optimal size for room temperature opera-

tion. Finally, the MOF's ability to be stable in the presence of H_2 gas impurities or when exposed to atmosphere, would be ideal given that some of the best performing MOFs demonstrate decomposition in air [27].

1.3.2.4 Chemical Storage

The final method of storing hydrogen is chemically in the solid state. These materials are known as hydrides and come in two varieties: complex and metal hydride. Metal hydrides are those that store hydrogen in the interstitial sites between the metal atoms or by ionic bonding between the hydrogen and the metal. Complex hydrides are salts that store hydrogen in the anion, bound to a metallic or semi-metallic element covalently, which in turn is ionically bound to a metal cation. Both types of hydrides have drawbacks with metal hydrides suffering from poor weight capacities and complex hydrides either possessing high decomposition temperatures or poor reversibility.

One example of a metal hydride is lanthanum nickel hydride ($LaNi_5H_6$). $LaNi_5H_6$ is extremely interesting as a hydrogen storage medium because it is able to liberate all of its hydrogen at not much greater than room temperature, 298K. Downsides to $LaNi_5H_6$ are that its gravimetric hydrogen storage capacity is only around 1.0 wt% and lanthanum is both rare and expensive [28,29]. Another example of a metal hydride is magnesium hydride (MgH_2). Due to using a much lighter metal the gravimetric hydrogen storage capacity of MgH_2 is 7.6 wt%, however this still does not

meet the DOE targets which involve a whole system not just the material. However, unlike $LaNi_5H_6$ where the bonding involved is metallic in nature, the bonding in MgH_2 is a mix of ionic and covalent. Typically ionic and covalent bonding energies are significantly higher than metallic bonding which means that the decomposition temperature of MgH_2 is far higher at around 300°C. This temperature is not ideal for use within mobile applications using proton exchange membrane fuel cells where they typically operate around 80°C to prevent the polymer membrane from drying out. For this reason a metal hydride storage system will need to decompose at or near 80°C and there are many ways to decrease this decomposition temperature including ball milling, catalysis and using a second component in the system to tune the thermodynamics [30, 31].

While metal hydrides are interesting, complex metal hydrides such as $LiBH_4$ and $LiAlH_4$ are seen as the materials more likely to meet DOE targets for hydrogen storage owing to their use of light elements, resulting in much higher weight capacities. Another advantage is that the elements used are potentially cheaper and more common than those used in metal hydrides as well. The disadvantages of complex metal hydrides, however, come from the covalent nature of the bonding between the hydrogen and the host element. This usually means that decomposition temperatures of these materials are extremely high or regenerating the original material requires a high energy process, high hydrogen pressures or temperatures [32–34].

1.3.3 Hydrogen Storage Comparison

When comparing hydrogen storage mediums five key areas for comparison are the most important: cost, volumetric capacity, gravimetric capacity, operational temperature and size of store. For the four mediums presented here compressed storage operates as the most expensive owing to the cost of the carbon fibre reinforced steel needed. Liquid storage for example comes in at over three times cheaper than compressed hydrogen while physisorption and chemical storage can be cheaper still if low cost elements can be used to form the hydrogen storage materials.

Volumetric storage capacities are superior for compressed and liquid storage while physisorption and chemical storage have the potential to have the greatest gravimetric storage densities of the four mediums while also maintaining an acceptable volumetric capacity.

A big variation is seen with the operational temperature of the different mediums with compressed storage the only system which can operate at room temperature. Both liquid and physisorption both require cryogenic temperatures to operate but while liquid hydrogen is completely dependant on these temperatures to prevent excessive boil off hydrogen physisorption has the potential to operate at close to room temperature if a suitable material with a high binding energy can be found. Chemical storage of hydrogen in metal or complex hydrides can vary massively from room temperature up to 600 °C. While the hydrides that can release and uptake hydrogen at low temperatures have very low gravimetric storage capacities, owing to the heavy

elements used, complex metal hydrides, that have much higher capacities, can have their high temperature of operation reduced by modifying the thermodynamics and kinetics but at the cost of reducing their overall storage capacity.

Liquid, physisorption and chemical storage are of great scientific interest because they can store hydrogen in a much smaller area compared to compressed hydrogen which, for a typical hatchback, has a tank that is the length of the vehicle. The other three mediums, however, have the potential to reduce this size down to what is currently the size of a petrol car's tank. While compressed storage has significant drawbacks, such as cost and gravimetric density, and the least potential to improve, except potentially liquid hydrogen, currently no material that is used for either physisorption or chemical storage can meet as many of the hydrogen storage targets that compressed can such as fill time, number of cycles and operating temperature.

1.4 Research Aims and Objectives

The main driver for this research is the targets set United States Department of Energy for the mobile storage of hydrogen as few materials are showing the potential to reach the 2017 parameters. Lithium borohydride has shown promise as a candidate to meet these targets but its high decomposition temperature and poor reversibility have so far made it ineligible. Therefore, the primary aim of this research is to reduce the decomposition temperature of lithium borohydride and improve its reversibility through a process known as thermodynamic tuning using multi-component systems. The secondary components used in this work will be nickel, silicon, iron and cobalt and the ability to form either borides or silicides in a reaction with $LiBH_4$ will be investigated.

The main objectives for this research will include:

- Investigate the use of elemental nickel in the destabilisation and reversibility of $LiBH_4$ compared to a $CaNi_5$ alloy which has previously been shown to be effective in improving both of these properties.
- Investigate the possibility of using elemental silicon to form either borides or silicides in a reaction with $LiBH_4$. The use of a TiF_3 catalyst will also be studied to aid in formation of these species.
- Determine if the use of the lighter transition metals iron and cobalt can provide a similar destabilising effect of that of nickel.

Table 1.3: System targets for thermodynamic turning of $LiBH_4$.

System Parameter	Target
Gravimetric Capacity (wt%)	6.5
Gravimetric Capacity (wt%) in Solid State (< 300 °C)	6.5
Reversible storage capacity (wt%)	6.5
Decomposition Temperature (°C)	85

While conducting these experiments the systems presented here will try and meet targets closely related to those set down by the DOE, listed in table 1.3, as closely as possible. During the discussion chapter these values will be compared against the experimental data collected to determine the success of the investigated systems.

1.5 Thesis Overview

Chapter 2 is a literature review of published articles on the improvements into the storage properties of $LiBH_4$. The main focus of the review will be an assessment of previous multi-component systems and their impact on the decomposition temperature and potential reversibility with additions to $LiBH_4$ including metals, alloys, compounds and other hydrides. The impact of other methods to improve the hydrogen storage properties of $LiBH_4$ will also be discussed including nano-confinement,

catalysis and ball-milling.

Chapter 3 will outline the materials and methods used for this research. The materials used, their handling and sample preparation is discussed along with the theory and experimental parameters used for the characterisation techniques.

Chapters 4 and 5 will encompass the experimental results and discussion for the different systems studied with each chapter broken down into three distinct sections:

- The use of nickel to improve the hydrogen storage properties of $LiBH_4$.
- Two approaches for the use of silicon in providing a destabilising effect.
- Investigations into the use of iron and cobalt and how they compare against nickel.

Chapter 6 will conclude the research presented and chapter 7 will discuss future work needed to further characterise each of the systems presented in this work.

Chapter 2

Literature Review

2.1 Introduction

In Chapter 1 it was discussed that to make hydrogen a viable replacement for fossil fuels within the transport sector it needs to have a storage capacity with a sufficient energy density that will compete with the range of fossil-fuel powered cars. This chapter outlines the research that has been conducted on the solid state storage of hydrogen using lithium borohydride ($LiBH_4$). The focus of this review will be on the thermodynamic tuning of $LiBH_4$ using material groups such as metals, intermetallics, chlorides, oxides and other hydrides. Also there will be a discussion on improving the reaction kinetics for $LiBH_4$, through varying preparation methods such as ball milling and catalysis, along with the confinement of $LiBH_4$ to improve

its overall hydrogen storage properties.

2.2 Lithium Borohydride

Lithium borohydride ($LiBH_4$) is a salt-like, crystalline material. It was first synthesised in the 1940s by Schlesinger and Brown by reacting together ethyl lithium and diborane (B_2H_6) [35] but has more recently been more directly synthesised by the reaction between lithium hydride (LiH) and B_2H_6 [36]. During thermal decomposition $LiBH_4$ is found to have three distinct endothermic events [37, 38]:

- A reversible polymorphic transformation of the $LiBH_4$ at 108-112 °C.
- The fusion of the $LiBH_4$ at 268-286 °C, at which up to 2% of the hydrogen is lost.
- The main evolution of gas which begins at 380 °C and liberates 80% of the stored hydrogen forming LiH.

The decomposition pathway for $LiBH_4$ was thus proposed in equation 2.1:

$$LiBH_4 \rightarrow LiH + B + \frac{3}{2}H_2 \tag{2.1}$$

When $LiBH_4$ is heated at slow rates, 0.5 and 1 K min^{-1}, other intermediates are observed during the decomposition and the most stable of these intermediates is $Li_2B_{12}H_{12}$ [39]. This compound was observed firstly by Raman spectroscopy [40]

and later by NMR spectroscopy [41]. The formation of this intermediate was postulated and is shown in equation 2.2:

$$LiBH_4 \leftrightarrow \frac{1}{12}Li_2B_{12}H_{12} + \frac{5}{6}LiH + \frac{13}{12}H_2 \leftrightarrow LiH + B + \frac{3}{2}H_2 \tag{2.2}$$

Later another investigation also proposed that $Li_2B_{12}H_{12}$ is not a true intermediate for the decomposition reaction but is instead a product of a side reaction between diborane evolved during the decomposition reaction that is able to react with remaining $LiBH_4$ [42]. The proposed reaction for this can be seen in equation 2.3:

$$2LiBH_4 + 5B_2H_6 \rightarrow Li_2B_{12}H_{12} + 13H_2 \tag{2.3}$$

Pressure composition isotherms (PCI) have been able to show that the enthalpy (ΔH) and entropy (ΔS) for the decomposition of $LiBH_4$ is 74 kJ mol^{-1} H_2 and 115 J K^{-1} mol^{-1} H_2 respectively [43]. This means that the decomposition of $LiBH_4$ is reversible and this has been demonstrated. The experimental conditions required for this are a temperature of 600 °C and 350 bar of pressure [44]. However, with these conditions the reaction takes longer than twelve hours to finish and does not guarantee a complete reaction. To improve the de/hydrogenation properties a method known as thermodynamic tuning can be used. Section 2.3 will detail several systems which exemplify a thermodynamic tuning reaction.

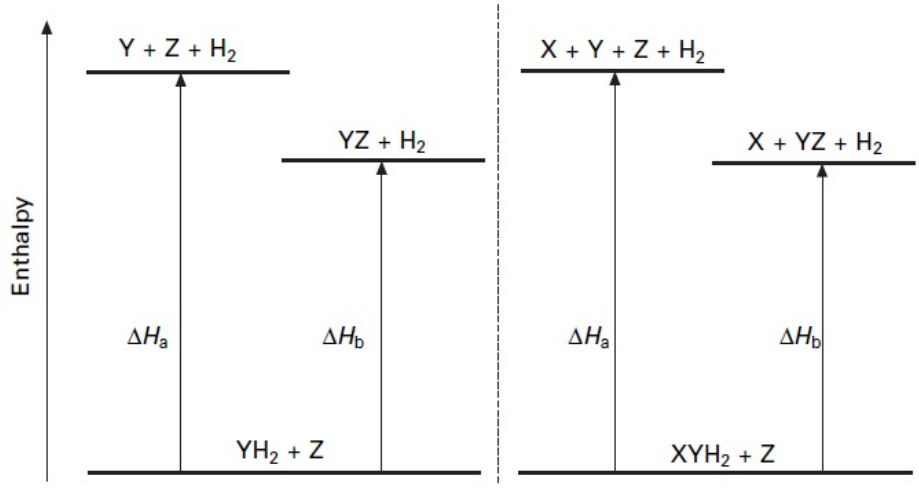

Figure 2.1: Enthalpy diagram demonstrating the lowering of a hydrides decomposition enthalpy upon reaction with a secondary component. [45]

2.3 Thermodynamic Tuning

The principal of thermodynamic tuning is to make hydrides more thermodynamically unstable which lowers the reaction enthalpy and thus lowering the decomposition temperature. In the case of multi-component hydrogen storage systems a reaction occurs between the hydride and a second material which has been added. The mechanism of thermodynamic tuning can be explained by an enthalpy diagram, figure 2.1, which shows the thermodynamic tuning of binary and complex hydrides. In the case of complex hydrides (right of the digram), of which $LiBH_4$ is one, when there is no reaction between the hydride (XYH_2) and second material (Z) then the enthalpy of decomposition is ΔH_a. When a reaction between one of the elements in the hydride (Y) and Z occurs, and has a lower enthalpy of reaction ΔH_b than the pure hydride decomposition, then the temperature at which the hydride decomposes

is reduced [45]. The following sections will detail thermodynamically tuned $LiBH_4$ systems and discuss their success and failures in improving the thermodynamics of the hydride.

2.3.1 Metal Addition

This section will discuss the addition of metals, such as aluminium and transition elements, which can form metal borides by reacting with the $LiBH_4$.

2.3.1.1 Aluminium

The addition of aluminium to destabilise $LiBH_4$ was first reported by Kang *et al.* in which they milled together $LiBH_4$ and Al in a 2:1 ratio [46]. They found that the system was able to release 7.2 wt% in 3 hours at 450 °C (90% of stored hydrogen). Reversibility was also studied and found to occur at 400 °C and 100 bar of pressure but suffered from poor cycling performance. The proposed reaction, equation 2.4, was as follows:

$$LiBH_4 + \frac{1}{2}Al \rightarrow LiH + \frac{1}{2}AlB_2 + \frac{3}{2}H_2 \tag{2.4}$$

Friedrichs *et al.* conducted further research into this system by investigating the reversibility of LiH and Al, combined ex-situ and not from decomposed $LiAlH_4$ [47]. They found that hydrogen absorption occurred at 300 °C and that it took 20 hours

to complete while under 150 bar of H_2 pressure. The total amount of absorbed hydrogen they saw from the first cycle was 7.6 wt% (92% of theoretical maximum). Poor cyclability occurred after three cycles and the capacity dropped to 2.4 wt%. They postulated that the reason for the poor cycling performance was that the Al-B reaction was incomplete upon subsequent decomposition steps owing to boron having to perform long range diffusion to react with aluminium and that AlB_2 has a low stability.

Meggough *et al.* found another possible reason for the poor cycling performance for this system by discovering the reason for the incomplete reaction between the Al and B [48]. They discovered that during decomposition AlB_2 forms a passivating layer over the aluminium which can prevent further reaction between Al and B and that using $LiAlH_4$ to form Al *in situ* provides a much more dispersed source of Al and therefore allowed a more complete reaction every time. They discovered that reversibility occurred at 350 °C and 85 bar of H_2 pressure. The thermodynamics of the system were calculated with the reaction enthalpy reduced to 38.2 kJ mol^{-1} and a T(1bar) of 240-300 °C.

Higher ratios of $LiBH_4$ to Al were studied by Ravnsbæk *et al.* and Hansen *et al.* to investigate the further reaction of Al with the LiH formed from the $LiBH_4$ decomposition [49, 50]. It was found that this increase in Al did lead to a further reaction, equation 2.5, but reduced the overall storage capacity to 6.4 wt%. Poor cycling was still observed with a reduction to 1 wt% after 10 cycles (15% of original

capacity). A TiB_2 catalyst was added which helped to improve the kinetics of the system by increasing the rate at which LiAl was formed. Hansen *et al.* found that this catalyst also increased the formation of $Li_2B_{12}H_{12}$ which contributed to the further reduction in cycling performance.

$$LiH + Al \rightarrow LiAl + H_2 \tag{2.5}$$

2.3.1.2 Transition Metals

Xia *et al.* conducted a study using nickel to improve the decomposition temperature and reversibility of $LiBH_4$ [43]. In this research, 2:1, 4:1 and 6:1 $LiBH_4$ to nickel ratios were used and it was found that up to 17 wt% H_2 could be released below 600 °C. Formation of trace amounts of nickel borides were observed and a dehydrogenation enthalpy of -61 kJ mol^{-1} was calculated. Reversibility of the systems were investigated and found that up to 3.3 wt% could be recovered at 600 °C with 100 bar of pressure.

Yang *et al.* looked into a wide range of metals to be used in the destabilisation of $LiBH_4$ including Titanium, Vanadium, Chromium and Scandium [51]. They found that none of these transition metals could destabilise $LiBH_4$ when milled in a 2:1 ratio ($LiBH_4$ to metal) but instead formed hydrides (Titanium, Scandium and Vanadium) as the $LiBH_4$ decomposed or had no effect (Chromium).

2.3.2 Intermetallic Addition

Intermetallics have long been considered as hydrogen storage materials with $LaNi_5$ being the alloy most investigated owing for its ability to de/hydrogenate 1.4 wt% of H_2 at room temperature and pressure [52]. However, there have been few reports, up until recently, with work being performed using intermetallics in multi-component systems to destabilise complex metal hydrides. This section will focus on two intermetallics, one in its alloy form and the other in its hydride form, used to destabilise $LiBH_4$.

2.3.2.1 Calcium Nickel Alloy

Calcium nickel alloy ($CaNi_5$) is an interesting material for hydrogen storage itself as it has a higher storage capacity than $LaNi_5$ (1.8 vs 1.5 wt%) and a lower plateau pressure [52, 53]. More recently its use as a reactant in $LiBH_4$ destabilisation has been investigated.

Ibikunle *et al.* investigated the use of the hydrided form of the alloy, $CaNi_5H_4$, as an alternative source of CaH_2 and milled it with $LiBH_4$ in a ratio of 6:1 [54]. It was hoped that the nickel would act as a dopant and aid in the decomposition reaction but it was found that it had no effect on the reaction and only added to the weight of the system, thus reducing its storage capacity.

Meggouh *et al.* found that by using the unhydrided form of the alloy in a 2:1

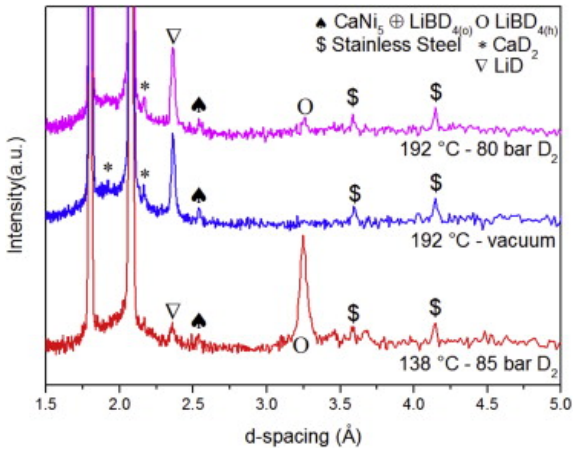

Figure 2.2: *In-situ* PND data showing the full decomposition of $LiBD_4$ using the $CaNi_5$ at 192 °C. This is followed by the partial regeneration of $LiBD_4$ under 80 bar of D_2 [55]

ratio that a significant reduction in the decomposition temperature of the $LiBH_4$ occurred [55]. With this system 1.1 wt% of hydrogen was released by 220 °C and no evidence of the $LiBH_4$ melting was observed, implying the reaction was completely carried out in the solid state. Partial reversibility was also observed during neutron diffraction experiments at 192 °C and 80 bar of D_2 pressure, shown in figure 2.2. A reaction, equation 2.6, was postulated:

$$2LiBH_4 + CaNi_5 \rightarrow 2LiH + CaH_2 + Ni_3B + Ni_2B + 3H_2 \tag{2.6}$$

2.3.2.2 Magnesium Nickel Hydride

Vajo *et al.* found that magnesium nickel hydride (Mg_2NiH_4) could induce a destabilisation reaction in $LiBH_4$ [56]. They found that the reaction begins at 250 °C and follows a stepwise reaction in which initially the $LiBH_4$ reacts with the Mg_2NiH_4,

equation 2.7, liberating 2.6 wt% by 340 °C, followed by the decomposition of the MgH_2 which liberates a further 2.1 wt% by 370 °C. The reversibility of the system was investigated in another paper [57] in which the rehydrogenation occurred below 300 °C, required 160 bar of H_2 pressure and recovered up to 1 wt% after 3 cycles.

$$4LiBH_4 + 5Mg_2NiH_4 \rightarrow 2MgNi_{2.5}B_2 + 4LiH + 8MgH_2 + 8H_2 \tag{2.7}$$

A more recent study into the system by Zhao *et al.* [58] investigated the addition of a catalyst into the system, 10 wt% $CeH_{2.29}$, and an additional processing step by heating the sample in a dynamic vacuum at 300 °C after the system was ball milled. It was found that the onset temperature for rapid dehydrogenation was reduced to 179 °C for the uncatalysed system and 102 °C for the catalysed system. Step one of the decomposition (boride formation seen in equation 2.7 and a 2.6 wt% loss) was completed by 197 °C and 167 °C for the uncatalysed and catalysed systems respectively.

2.3.3 Metal Chloride Addition

Au *et al.* first investigated the use of several different species in the destabilisation of $LiBH_4$ with two different chloride species showing promise [59, 60]. $TiCl_3$ was used on its own in two different ratios, $LiBH_4$ + 10 or 25% $TiCl_3$, and it was

shown that the 25% system started to rapidly dehydride at 100 °C with a final release of 8.2 wt% by 600 °C. The 10% system started to rapidly dehydride at 250 °C with a final mass loss of 9.2 wt% at 600°C. The group also investigated the use of $MgCl_3$ in conjunction with $TiCl_3$. The $LiBH_4$:0.2$MgCl_3$:0.1$TiCl_3$ system started to rapidly dehydride at 60 °C and lost 4 wt% by 400 °C. Reversibility was investigated and found to occur at 600 °C and 70 bar of H_2 pressure and recovered up to 9 wt% H_2. The main decomposition product formed during these reactions were LiCl. A more recent study by Au *et al.* discovered the mechanism for the decomposition of $LiBH_4$ by $TiCl_3$ [61]. They found that at higher molar levels of $TiCl_3$, $LiBH_4$:0.5$TiCl_3$, that a cation exchange reaction occurs in the borohydride, similar to previous experiments conducted [62], where the Ti replaces the Li in the borohydride, equation 2.8. This unstable borohydride led to the formation of large amounts of diborane during the decomposition indicated by a 37% mass loss by 100 °C. Reversibility was investigated for this system but was found not to be possible at 500 °C and 70 bar owing to boron loss from diborane formation. However, compared to other systems, a pressure of 70 bar was not likely to reform $LiBH_4$.

$$3LiBH_4 + TiCl_3 \rightarrow 3LiCl + Ti(BH_4) \tag{2.8}$$

Another study with low amounts of $TiCl_3$, by Mosegaard *et al.*, found that there is a solid state reaction between the two materials at room temperature [63]. When 2% $TiCl_3$ was used, and milled together by hand, a reaction was observed to occur,

indicated by a change in colour, unless the system was stored at -35 °C. It was also observed that LiCl, formed during this solid state reaction, dissolved into the solid structure of the $LiBH_4$ as it was no longer observed in the XRD data between 100 and 245 °C.

One study by Zhang *et al.* investigated the use of other transition metal chlorides in the destabilisation of $LiBH_4$ [64]. It was found that when $LiBH_4$ was mixed in a 2:1 ratio with $NiCl_2$, $FeCl_2$ or $CoCl_2$ then the dehydrogenation temperature is reduced to between 230 and 300 °C. It was found that almost 100% of the stored hydrogen could be released in the case of the $NiCl_2$ and $FeCl_2$ systems but a capacity loss of a third was observed for the $CoCl_2$ system owing to diborane formation. The postulated destabilisation reaction was a cation exchange reaction to form unstable borohydrides which results in the formation of metal borides and LiCl upon full decomposition. At addition levels of 5 and 10% it was found that only $NiCl_2$, compared to $FeCl_2$ and $CoCl_2$, was able to improve system kinetics with a reduction in reaction temperature by 50-60 °C.

2.3.4 Metal Oxide Addition

2.3.4.1 Silicon Oxide

Silicon oxide (SiO_2) was one of the first materials considered for the destabilisation of $LiBH_4$. Züttel *et al.* investigated its use in a $LiBH_4$-SiO_2 system with a 25:75

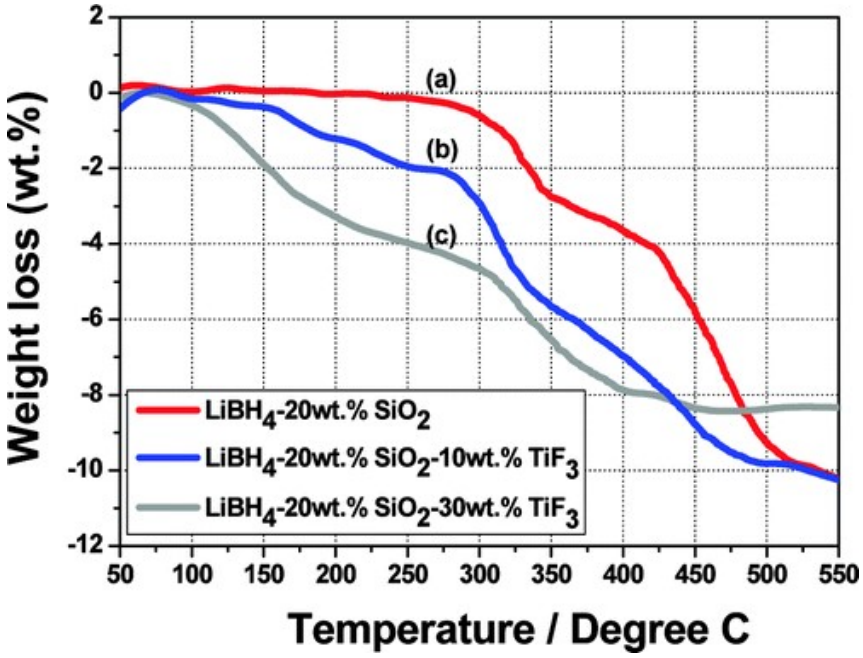

Figure 2.3: TGA decomposition curves for three different $LiBH_4$-SiO_2-TiF_3 systems. [65]

mass ratio [37, 38]. It was found that this system could release a total of $\frac{3}{4}$ of the stored H_2, starting at 200 °C, of which it could release half of the stored H_2 by 400 °C. This paper, however, did not discuss whether this was a catalytic reaction or a stoichiometric, destabilisation reaction. Zhang *et al.* investigated a $LiBH_4$-SiO_2-TiF_3 composite where the SiO_2 was 20 wt% of the system and the TiF_3 being either 10 or 30 wt% of the system [65]. It was found that this system could release 4 wt% by 300 °C and 10 wt% by 550 °C. For the 30% TiF_3 system, the onset dehydrogenation was reduced to 70 °C. The TGA decomposition curves for these reactions are shown in figure 2.3. A reaction was postulated, equation 2.9, that Li_4SiO_4 was formed, along with elemental silicon and boron, owing to no crystalline boron species observed after the reaction. Reversibility was found to occur for the

30% TiF_3 system at 500 °C and 45 bar of H_2 pressure where it was able to uptake 4 wt% in 14,000 s but no evidence of $LiBH_4$ was observed post-hydrogenation. Moosegard *et al.* investigated the use of SiO_2 in various molar amounts [63]. They found that Li_2SiO_3 was formed when high molar levels of SiO_2 were used (25.5 mol%). When lower amounts of SiO_2 were used (5 and 9.9 mol%) then both the formation of Li_2SiO_3 and Li_4SiO_4 were observed. Decomposition was seen to occur at temperatures greater than 200 °C and was found that the reaction was also irreversible in contrast to the Zhang *et al.* paper.

$$4LiBH_4 + SiO_2 \rightarrow Li_4SiO_4 + 4B + Si + 8H_2 \tag{2.9}$$

2.3.4.2 Titanium Dioxide

Titanium dioxide (TiO_2) has also been investigated in high and low stoichiometric amounts on its ability to destabilise $LiBH_4$. Yu *et al.* investigated the addition of TiO_2 in a high stoichiometric ratio with $LiBH_4$ and the 1:4 by weight (1:1.1 by moles) $LiBH_4$ to TiO_2 was found to be the most successful system for levels of decomposed hydrogen [66]. It was discovered that 3.65 wt% was the total mass loss and formed $LiTiO_2$ upon decomposition, equation 2.10. No crystalline boron containing species were observed during XRD indicating that it was in an amorphous state. Reversibility of this system was not investigated. A low stoichiometric amount of TiO_2 was used in the research conducted by Au *et al.* [67]. They used TiO_2 as

25% of the system mass or in a molar ratio $LiBH_4$:0.09TiO_2. With this system it was found that the TiO_2 decreased the decomposition temperature so that 4 wt% was released by 400 °C with the primary phases formed during decomposition being (LiOH)(H_2O), TiB_2 and LiOH, observed by XRD, and no $LiTiO_2$ was observed compared to the high stoichiometric amounts. Reversibility was investigated in this paper and it was found that 8 wt% could be absorbed, at 600 °C and 100 bar H_2 and forms $LiBH_4$. However, cycling performance was poor as Li_3BO_3 is also formed upon rehydrogenation and removes Li and B from the system for subsequent cycles.

$$LiBH_4 + TiO_2 \rightarrow LiTiO_2 + B + H_2 \tag{2.10}$$

2.3.4.3 Other Oxides

Other oxides have been considered for the destabilization of $LiBH_4$ and in the same study by Au *et al.* [67] ZrO_2, V_2O_3 and SnO_2 were investigated. All of these oxides were combined with $LiBH_4$ as 25% by mass of the system and showed similar decomposition profiles to that of TiO_2 with 9 wt% given off by 600 °C and showing a dehydrogenation onset at 175 °C. Yu *et al.* also investigated several different oxides and found that a hierarchy for the destabilisation of $LiBH_4$ could be formed where Fe_2O_3>V_2O_5>Nb_2O_5>TiO_2>SiO_2 [68]. It was found that Fe_2O_3 could release 6 wt% by 200 °C in a 1:2 mass ratio with $LiBH_4$ ($LiBH_4$ to Fe_2O_3) and an

overall reaction equation for the metal oxide destabilisation of $LiBH_4$ was postulated, equation 2.11:

$$LiBH_4 + MO_x \rightarrow LiMO_x + B + H_2 \tag{2.11}$$

2.3.5 Binary Hydrides

2.3.5.1 Magnesium Hydride

It was first proposed by Vajo *et al.* that MgH_2 could be used to destabilise $LiBH_4$ [69]. It was found that MgH_2 could reversibly store 8-10 wt% H_2 when combined with $LiBH_4$, reduce the dehydrogenation enthalpy of $LiBH_4$ by 25 kJ mol^{-1} (to 40.5 kJ mol^{-1}) and provide a T(1 bar) of 225 °C. The destabilisation reaction, equation 2.12, was found to form MgB_2 but only under hydrogen back pressure and not under dynamic vacuum. In this paper reversibility was only possible with MgB_2 present and absorbed a maximum of 10 wt% at 450 °C and under 24 bar of H_2. It was later found by Bösenberg *et al.* that the reaction proceeds in a two stage process, equation 2.13, where the MgH_2 decomposes first to Mg, after which this reacts with the $LiBH_4$ [70]. Reversibility was also investigated and found to occur at 250-300 °C, under 50 bar H_2, in which both products were found to form simultaneously.

$$LiBH_4 + \frac{1}{2}MgH_2 \leftrightarrow LiH + \frac{1}{2}MgB_2 + 2H_2 \tag{2.12}$$

$$2LiBH_4 + MgH_2 \rightarrow Mg + H_2 + 2LiBH_4 \rightarrow 2LiH + \frac{1}{2}MgB_2 + 3H_2 \tag{2.13}$$

A different route for the destabilisation reaction was proposed by Walker *et al.* in several papers in which it was discovered that under vacuum the reaction forms an MgLi alloy instead of MgB_2 [71–74]. They proposed that the originally investigated 2:1 ratio for the $LiBH_4$ MgH_2 system was inferior to a 0.3:1 system where, upon complete decomposition, it forms two different magnesium-lithium alloys, equation 2.14. This new system was able to decompose 9.8 wt% H_2 and demonstrated 95% reversibility at 400 °C and 100 bar H_2. Kinetics for the two systems were also studied and it was found that the 0.3:1 system could decompose 90% of its stored hydrogen, at 40 °C, within 10 minutes while the reverse reaction saw it uptake 90% of its capacity within 15 minutes. The 2:1 system, however, performed poorly with only 60% decomposed after 4 hours at 400 °C and rehydrogenation was equally as slow with only 50% taken up after 4 hours.

$$0.3LiBH_4 + MgH_2 \leftrightarrow 0.37Li_{0.184}Mg_{0.816} + 0.15MgB_2 + 0.78Li_{0.30}Mg_{0.70} + 1.6H_2 \tag{2.14}$$

2.3.5.2 Calcium Hydride

The use of calcium hydride (CaH_2) to destabilise $LiBH_4$ was first investigated by Yang *et al.* while testing multiple systems that had previously been identified

through thermodynamic assessments [51, 75]. It was found that the system could not fully release all of its stored hydrogen, 5.1 out of 11.7 wt%, when held at 400 °C for 100 h and was not reversible at 350 °C and 150 bar of H_2 pressure. CaB_6 was formed during the decomposition and a reaction was proposed, equation 2.15.

$$6LiBH_4 + CaH_2 \rightarrow CaB_6 + 6LiH + 10H_2 \tag{2.15}$$

A series of papers [76–78] all investigated the decomposition and reversibility of the system. Pinkerton *et al.* were the first to investigate the system and discovered that adding 0.25 moles of $TiCl_3$ to the system helped reduce the onset dehydrogenation temperature to 150 °C with the majority of the H_2 released by 350 °C and complete by 400 °C. CaB_6 and LiH were formed, as expected, during the decomposition and reversibility of 9.1 wt% was achieved at 400 °C and 83 bar of H_2. Jin *et al.* used a similar system but used less $TiCl_3$ (0.2 moles) and observed that the onset temperature had increased slightly to 230 °C. System reversibility of 6 wt% was also confirmed in this paper with it rehydriding at similar conditions of 400 °C and 100 bar H_2 after 20 h. Lim *et al.* used a different catalyst, NbF_5, which was found to be an improvement over the $TiCl_3$ systems where 9.1 wt% could be released by 400 °C and begins at 200 °C. The thermodynamics of the system were also investigated with a dehydrogenation reaction enthalpy of 56.5 kJ mol^{-1} and T(1bar) of 309 °C presented. Lim *et al.* also investigated the cycling performance of the system in a later paper [79]. The best reversibility for the system occurred

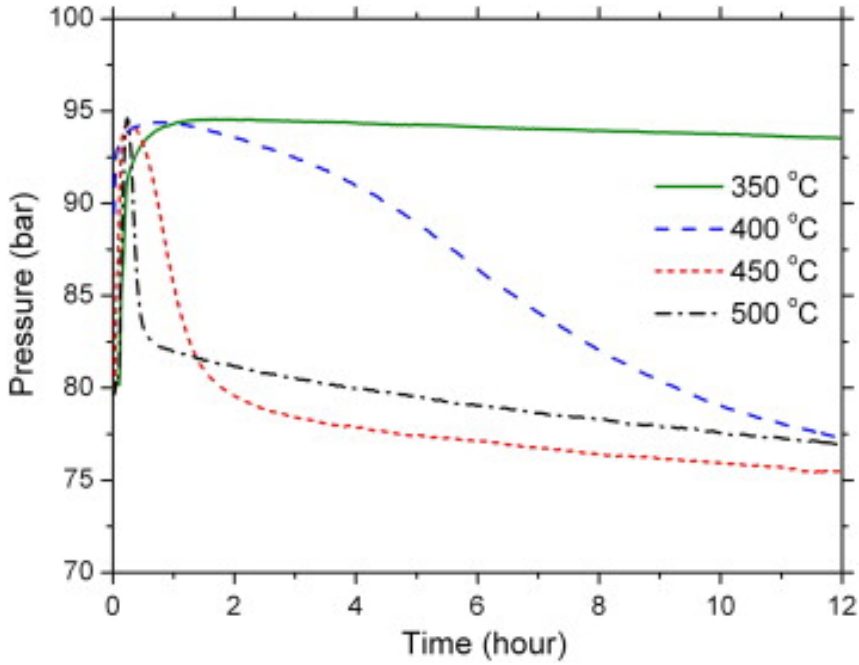

Figure 2.4: Hydrogen uptake curves of the $6LiBH_4$-CaH_2 (5 wt% NbF_5) system at different temperatures showing the fastest uptake at 450 °C. [79]

at 450 °C after which 9 wt% H_2 was uptaken compared to 8.4 wt% at 500 °C. The speed of hydrogen uptake is shown in figure 2.4. The system was shown to suffer from cycling degradation where capacity is reduced from 9 wt% to 6 wt% after 5 cycles owing to the growth of the CaB_6 crystals. However, NbF_5 was found to help improve the cycling performance by reducing the microstructural coarsening that occurred after repeated cycles.

2.3.5.3 Other Systems

Jin *et al.* discovered that cerium hydride (CeH_2) could also be used to destabilise $LiBH_4$, equation 2.16, similarly to CaH_2 [80]. The system was calculated to have

a theoretical capacity of 7.39 wt% and experimentally released 6.1 wt% by 430 °C with dehydrogenation onset occurring at 180 °C. Hydrogenation of this system was found to proceed at 350 °C and 100 bar of H_2 and took 20 h to complete. Mauron *et al.* performed a thermodynamic study of this system [81] and calculated that the reaction enthalpy for dehydrogenation was reduced to 58 ± 3 kJ mol^{-1}, entropy reduced to 113 ± 4 J $K^{-1}mol^{-1}$ and a T(1 bar) bar of 240 ± 32 °C (74, 115 and 370 for pure $LiBH_4$ respectively).

$$6LiBH_4 + CeH_2 \rightarrow 6LiH + CeB_6 + 10H_2 \tag{2.16}$$

Yttrium hydride is also able to destabilise $LiBH_4$ as found by Shim *et al.* [82]. For this system to have the destabilisation reaction occur, equation 2.17, a hydrogen back pressure is required. When decomposing the system under dynamic vacuum at 350 °C only 2 wt% could be desorbed after 24 hours, but with 3 bar of H_2 back pressure 7.2 wt% is given off at the same temperature and within the same time frame owing to the microstructural evolution of the dehydrogenation products formed by a solidliquid reaction. For this system the formation of YB_4 was more stable than YB_6, as previously seen with CeH_2 and CaH_2, with rehydrogenation achieved at 350 °C, 90 bar of H_2 pressure and 24 h to react in which 5.2 wt% was uptaken.

$$4LiBH_4 + YH_3 \rightarrow 4LiH + YB_4 + 7.5H_2 \tag{2.17}$$

2.3.6 Complex Hydride Addition

This section will detail the addition of other complex metal hydrides to destabilise $LiBH_4$ with several different metal alanates ($^{-}AlH_4$) and amides ($^{-}NH_2$) discussed.

2.3.6.1 Alanate Addition

The use of an alanate to decompose $LiBH_4$ was first discussed by Jin *et al.* in which they found that $LiBH_4$ milled together with lithium alanate ($LiAlH_4$) in a 2:1 ratio, with 3 mol% TiF_3, resulted in a destabilised system [80]. Decomposition was observed to begin at 177 °C and released a total of 7.2 wt% by 387 °C with the formation of AlB_2 observed when left for 4 h at 400°C. During the milling process was found that the $LiAlH_4$ decomposed leaving behind aluminium to react with the $LiBH_4$. Reversibility was found to be possible at 400 °C, 70 bar of H_2 and, after 6 h, 5.2 wt% could be uptaken. Mao *et al.* investigated this system further by performing catalytic and thermodynamic studies [83]. The addition of 5 mol% TiF_3 reduced the onset decomposition temperatures of the first and second steps by 54 and 150 °C respectively. The reaction enthalpy for $LiBH_4$ was calculated to be 60.4 kJ mol^{-1}, down from 74 kJ mol^{-1} for pure $LiBH_4$. Reversibility was also investigated with 4.78 wt% uptaken after 4 h at 600 °C and 40 bar of H_2.

Alternative catalysts for the $LiBH_4$-$LiAlH_4$ system were proposed with $TiCl_3$ showing promising results [48, 84]. Blanchard *et al.* found that milling $LiBH_4$ with

$LiAlH_4$ in a 1:3 ratio with 4 mol% $TiCl_3$ could desorb 7 wt% H_2 by 390 °C. Reversibility was investigated with a 2.5 wt% uptake at 350 °C and 85 bar but cycling losses were attributed to the formation of B_2H_6. Meggouh *et al.* also used $TiCl_3$ as a catalyst but utilised the previously investigated 2:1 ratio between $LiBH_4$ and $LiAlH_4$ [48]. To this system 3 mol% $TiCl_3$ was added and longer milling times were used, 4 h, compared to other papers. Onset dehydrogenation occurred at 290 °C and the dehydrogenation enthalpy was calculated to be 38.2 kJ mol^{-1} with a corresponding T(1 bar) of 240-300 °C. Reversibility was superior to previous papers using $TiCl_3$ where 77% of the system storage could be reversed when left for 2 h at 350 °C and 85 bar of H_2. This improved reversibility was attributed to the lack of LiAl formation and is shown in figure 2.5 A reaction for this system, equation 2.18, would be as follows:

$$\begin{aligned} 2LiBH_4 + LiAlH_4 &\rightarrow 2LiBH_4 + LiH + Al + \frac{3}{2}H_2 \\ 2LiBH_4 + Al &\rightarrow 2LiH + AlB_2 + \frac{3}{2}H_2 \end{aligned} \tag{2.18}$$

Other alanates studied for the destabilisation of $LiBH_4$ include sodium alanate, magnesium alanate and calcium alanate. The use of sodium alanate $NaAlH_4$ to destabilise $LiBH_4$ was investigated by Shi *et al.* in which they milled it together in 1:1, 2:3 and 1:3 ratios ($LiBH_4$ to $NaAlH_4$) with a 4 mol% TiF_3 catalyst [85]. The 1:3 doped system showed the best properties in which it was able to decompose 3.9 wt% by 210 °C by following a cation exchange between the two hydrides, equation

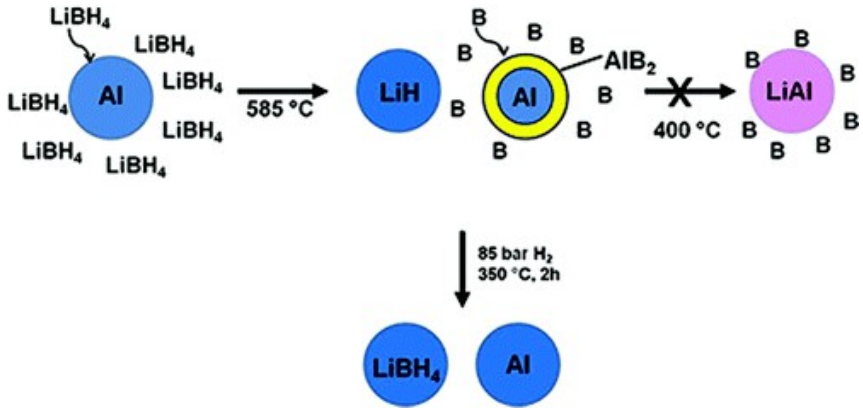

Figure 2.5: Formation of an AlB_2 shell prevents the formation of LiAl and allows for easier regeneration of $LiBH_4$ [48]

2.19, after which the formed $LiAlH_4$ decomposes along its traditional decomposition route. Uptake of 0.6 wt% occurs when reversed at 80 bar and 180 °C but does so by forming a new product $LiNa_2AlH_6$, equation 2.20, when an excess of $NaAlH_4$ is used, equation 2.21, and decomposes to form NaH.

$$LiBH_4 + NaAlH_4 \rightarrow LiAlH_4 + NaBH_4 \tag{2.19}$$

$$LiH + 2NaH + Al + \frac{3}{2}H_2 \leftrightarrow LiNa_2AlH_6 \tag{2.20}$$

$$\begin{aligned} 3NaAlH_4 &\rightarrow Na_3AlH_6 + Al + H_2 \\ Na_3AlH_6 &\rightarrow 3NaH + Al + \frac{3}{2}H_2 \end{aligned} \tag{2.21}$$

Liu *et al.* investigated the use of magnesium alanate ($Mg(AlH_4)_2$) to destabilise

$LiBH_4$ [86]. The two materials were milled in a 6:1 ratio ($LiBH_4$ to $Mg(AlH_4)_2$) and released 11.8 wt% of H_2 after 200 min at 400 °C using a three step reaction pathway, equation 2.22. Reversibility was also found to be possible for this system with a 6.4 wt% uptake after 300 min at 400 °C and 30 bar. Products formed from this included $LiBH_4$, MgH_2 and Al.

$$\begin{gathered} Mg(AlH_4)_2 \rightarrow MgH_2 + 2Al + 3H_2 \\ MgH_2 + \frac{3}{2}Al \rightarrow \frac{1}{2}Mg_2Al_3 + H_2 \\ 6LiBH_4 + \frac{1}{2}Mg_2Al_3 + \frac{1}{2}Al \rightarrow 6LiH + MgAlB_4 + AlB_2 + 9H_2 \end{gathered} \tag{2.22}$$

Liu *et al.* investigated the use of calcium alanate ($Ca(AlH_4)_2$) to destabilise $LiBH_4$ [87]. They milled together $LiBH_4$ and $Ca(AlH_4)_2$ in three different molar ratios (10:1, 6:1 and 2:1) and found that the $6LiBH_4$:$Ca(AlH_4)_2$ system showed the most promising results with it releasing 8.2 wt% H_2 after 35 min at 450 °C. The system followed a three stage decomposition process in which the $Ca(AlH_4)_2$ decomposed first, equation 2.23, after which the $LiBH_4$ reacted with the *in situ* formed components, equation 2.24, and finally a reaction between excess CaH_2 and Al, equation 2.25. Reversibility was found to be possible for this system with the 6:1 system uptaking 4.5 wt % H_2 after 600 min at 450 °C and 40 bar of H_2. Species formed from this reaction include $LiBH_4$ and $Ca(BH_4)_2$.

$$Ca(AlH_4)_2 \rightarrow CaH_2 + 2Al + 6H_2 \tag{2.23}$$

$$8LiBH_4 + CaH_2 + Al \rightarrow 8LiH + CaB_6 + AlB_2 + 13H_2 \tag{2.24}$$

$$CaH_2 + 4Al \rightarrow CaAl_4 + H_2 \tag{2.25}$$

2.3.6.2 Amide Addition

This section will deal with the addition of lithium amide ($LiNH_2$) to destabilise $LiBH_4$. Aoki *et al.* were the first to propose this system in which they conducted first principles calculations and experiments [88]. The enthalpy of decomposition was calculated to be 23 kJ mol^{-1} (a reduction of 52 kJ mol^{-1} from as-received $LiBH_4$) and experimentally 7.8 wt% H_2 could be desorbed at 249 °C and formed Li_3BN_2, equation 2.26. Additionally it was observed that upon milling a Li_3N-BN compound was formed.

$$LiBH_4 + LiNH_2 \rightarrow Li_3BN_2 + 4H_2 \tag{2.26}$$

Pinkerton *et al.* later found this intermediate compound to be $Li_3BN_2H_8$ and that is was formed upon milling or heating of the two starting materials to 95 °C [89]. This quaternary hydride was discovered to have an 11.9 wt% theoretical capacity, melt at

190 °C and decompose above 250 °C. It was also observed that ammonia was also released during the decomposition (2-3 mol%) and reversibility was not possible under 80 bar of H_2 pressure. Later the same group found that the quaternary hydride had the structure $Li_4BN_3H_{10}$ [90]. They also investigated several different stoichiometric ratios between the two starting materials and found that the original 1:2 ratio was optimal for both hydrogen release and the suppression of ammonia formation [91].

The addition of different transition metal catalysts were studied to improve reaction kinetics and suppress the formation of ammonia. Pinkerton *et al.* investigated the use of both palladium (Pd) and platinum (Pt) as catalytic additives [92]. The best additive level to use was 5 wt% Pd which was able to reduce the onset decomposition to 150 °C and showed no ammonia formation if the decomposition temperature was kept below 210 °C. Reversibility was investigated for this system but was shown to be poor as only 15% of the system's capacity could be recovered and the formation of the quaternary hydride or starting materials was not confirmed. Pinkerton *et al.* later investigated the use of $NiCl_2$ as a catalyst for the system [93]. The onset dehydrogenation temperature using this catalyst was 122 °C and ammonia formation only occurred at temperatures above 240 °C. Zhang *et al.* investigated the use of $CoCl_2$-LiH catalyst and found that the system could release 9.6 wt% H_2 at 160-250 °C [94]. With this catalyst, ammonia formation was extremely low with only 80 ppm observed in the decomposition gasses.

2.4 Kinetic Improvements

2.4.1 Ball-Milling

Ball-milling is a highly energetic process used to produce nano-structured materials to improve their reaction properties. This technique is inexpensive, simple, widely applicable and scalable way of forming nano-scale particles (<100 nm) by plastic deformation or brittle fracture of coarser grains [95]. The reason that ball-milling is particularly important for hydrogen storage materials is that when they are at the nano-scale they have significantly more atoms close to grain boundaries as well as better interfacial mixing of multicomponent systems and catalysts. This allows the increased diffusion of hydrogen atoms in both hydrogenation and dehydrogenation reactions while also breaking down any oxide layers formed on the hydride's surface [96]. Ball-milling has shown to be effective in increasing reactivity in multi-component systems. It ensures that good mixing of the two components is occurring, increasing the available reactable surface area of the two components, and causes surface defects that aid in reaction and ensuring that any catalyst is well dispersed throughout the sample [30, 97].

For MgH_2 it has been shown that ball-milling can significantly improve its decomposition properties. Huot *et al.* investigated the milling of MgH_2 and found that when the material was milled for 2 h the MgH_2 changed phase to orthorhombic, did not have its storage capacity reduced but did experience an increase in the specific

surface area of the material [98]. It was found that the decomposition temperature was reduced by 64 °C and that the milled material fully desorbed faster at 400 °C (700s) than the un-milled material could at 425 °C (900s). Hydrogenation was improved with milling where 7.2 wt% could be reversibly uptaken at 300 °C compared to 6.8 wt% at 400 °C for un-milled MgH_2. Reuele *et al.* investigated the use of additives milled with MgH_2 and found that upon milling the MgH_2 formed a layer covering the additive with kinetic improvements attributed to the large interface created between the MgH_2 and the additive [99].

2.4.2 Catalysis

The early use of catalysts in the improvement of the kinetics of $LiBH_4$ was reported by Vajo *et al.* when they used $TiCl_3$ to improve the kinetics of the $2LiBH_4$:MgH_2 destabilised system [69]. Since then many different $LiBH_4$ catalysed systems have been reported with both pure and destabilised systems investigated. One proposed mechanism for the catalytic activity is related to reported spillover effect. This mechanism involves the transport of an active species (hydrogen) formed from one surface (hydride) onto another surface (catalyst) which does not react with the active species [100, 101].

2.4.2.1 Platinum Group Metals

Platinum group metals, such as platinum (Pt), palladium (Pd) and ruthenium (Ru), have been considered for use as catalysts in both as-received and destabilised systems. Usually these catalysts are dispersed as nanoparticles in carbon supports and are loaded from anywhere between 5 and 50 % of the system weight.

Xu *et al.* investigated the use of both Pt and Pd nanoparticles to enhance the storage properties of $LiBH_4$ [102–104]. With Pt supported in a carbon catalyst it was found that with a 10 wt% loading the onset decomposition temperature was reduced from 420 °C to 280 °C with two major decomposition events occurring before the first one observed at 485 °C for the as-received material. When loadings were increased up to 50 wt% of the system almost the entire 18.5 wt% H_2 stored in the $LiBH_4$ could be released and this was attributed to the high surface area between the two materials. Reversibility was investigated with 6.1 wt% reversibly maintained after 30 cycles at 600 °C and 30 bar of H_2 over 24 h. LiC was observed to form during decomposition, in a reaction with the carbon support, while $B_{16}H_{20}$ and Li_5PtH_3 were both formed during the hydrogenation which helps to explain the lack of capacity by not forming $LiBH_4$. When graphene was used to support the Pt nanoparticles the properties were improved further still with only two major decomposition events observed, instead of three. With the onset decomposition still occurring at 280 °C for the 10 wt% catalyst system. System capacity was observed to be 12.1 wt% (10.7 wt% for as-received $LiBH_4$ at same conditions) with B_2H_6 formation found to be suppressed.

Reversibility was improved with 8.1 wt% maintained after 30 cycles at 400 °C, 30 bar of H_2 and 10 h reaction time. The presence of $LiBH_4$ was confirmed after hydrogenation but also $Li_2B_{10}H_{10}$. The same group used palladium in the same conditions as the platinum and discovered that onset decomposition was the same at 280 °C for the 10 wt% loaded system and that smaller nanoparticles were the most effective. Reversibility was worse for the palladium system where only 4.3 wt% was reversible after 4 cycles, at 600 °C, 30 bar of H_2 and 24 h, and formed $B_{16}H_{20}$ instead of $LiBH_4$.

The $LiBH_4$ and MgH_2 multicomponent system catalysed by the platinum group has also been investigated. Weng *et al.* used carbon supported Pd nanoparticles and found that onset decomposition was reduced from 360 °C to 260 °C with a total mass loss of 8 wt% possible below 400 °C [105]. Reversibility investigations found that 7.8 wt% could be reversed at 400 °C and 35 bar after 6 h. With the catalyst the reaction proceeds in two steps in which initially the MgH_2 reacts with the Pd to liberate elemental magnesium, after which the Mg reacts with the $LiBH_4$ to form magnesium boride. Mao *et al.* investigated the use of ruthenium to destabilise the same system [106]. The $2LiBH_4$:MgH_2 system was doped with 10 wt% Ru in a carbon support and reduced the first and second decomposition steps from 360/380 °C to 310/360 °C respectively. A kinetics study of the system demonstrated that at 380 °C, 8.39 wt% could be desorbed after 2 h whereas the uncatalysed system could only desorb 6.37 wt% in the same period. Reversibility was also improved with a

7.5 wt% uptake after 8 h (at 500 °C and 40 bar of H_2) versus only a 5.3 wt% uptake for the uncatalysed system. Cycling capacity experiments for the catalysed system showed that 7.6 wt% could be maintained over the first three cycles.

2.4.2.2 Nickel

Negene *et al.* demonstrated that the combination of nano-confinement and the addition of 3.75 wt% nickel (Ni) was effective in improving the ability to regenerate $LiBH_4$ [107, 108]. When the samples were regenerated under 40 bar H_2 at 320 °C for 2 h an uptake of 2.3 wt% was achieved with the addition of the nickel catalyst compared to just the nano-confinement of the $LiBH_4$. It was discovered that the elemental nickel did not act as a catalyst during this reaction, however, but the formation of nickel borides (Ni_xB), formed by a reaction between the nickel and $LiBH_4$, provided the catalytic effect shown by the system. Evidence for the formation of nickel borides during the decomposition was further supported with the observation of Ni_4B_3 formed when higher levels of nickel were present in the system. Li *et al.* reported that with 25 wt% Ni used the decomposition temperature of the system is reduced from 470 °C to 423 °C with Ni_4B_3 a by-product of the reaction [109]. Regeneration of the $LiBH_4$, performed at 550 °C under 350 bar H_2 for 24 h, demonstrated that the nickel addition allowed 10.8 wt% to be taken up compared to 4.3 wt% for as-received $LiBH_4$ under the same conditions. Further, the Ni_4B_3 transformed to Ni_2B during the regeneration process but continued to

provide the same catalytic effect as its precursor. When Xu *et al.* used graphene to support the nickel nanoparticles they discovered that decomposition began at 180 °C with the main dehydrogenation peaks occurring at 275 and 465 °C with the formation of Ni_4B_3 shown to occur [110]. Reversibility was performed for 10 h at 400 °C and 30 bar of H_2 and was shown to maintain a storage capacity of 9.8 wt% after 30 cycles. Similar to their studies with Pt and Pd, $Li_2B_{10}H_{10}$ formed along with $LiBH_4$ while the Ni_4B_3 present did not transform into Ni_2B when the nickel was not supported.

Nickel additives have also been investigated to aid in the decomposition of the $2LiBH_4$:MgH_2 destabilised system. Mao *et al.* investigated the use of two varying amount of nickel: 0.5 and 0.05 moles stoichiometrically. It was discovered that nickel was useful in promoting the decomposition of MgH_2, in particular, but higher quantities of nickel were only found to enhance $LiBH_4$ decomposition [111]. The onset of decomposition for MgH_2 in the 0.05 Ni system was observed to occur at 310 °C (40 °C lower than the pure system) with a maximum release rate occurring at 331 °C (34 °C lower) but no change in the $LiBH_4$ decomposition temperature was observed. For the 0.5 Ni system the decomposition of the two hydrides was found to occur at 313 and 410 °C (52 and 25 °C lower respectively) but this led to a drop in the hydrogen storage capacity. Upon decomposition it was observed that a tertiary Mg-Ni-B alloy was formed, prominently in the 0.5 Ni system, which indicates that at low levels the Mg can act as a catalyst but at higher levels it starts to act as a reactant.

Reversibility was improved for the system where the Mg-Ni-B alloy was present with a 5.3 wt% uptake observed after 10 h at 400 °C and 55 bar of H_2 pressure compared to only 4.4 wt% for the pure system. Shao *et al.* took a different approach and used pre-made Ni-B catalysts rather than forming them *in-situ* via a reaction between the Ni and $LiBH_4$ [112]. They investigated using the decomposed species (LiH and MgH_2) to improve the re/dehydrogenation properties of the system with 10 wt% of the system as Ni-B. When hydrogenated at 350 °C under 100 bar H_2 it was observed that 90% of the expected uptake occurred within 2 h compared to almost 4 h for the undoped system. The formation of $LiBH_4$ and MgH_2 were confirmed by both XRD and FTIR after hydrogenation. Upon decomposition, at 400 °C and 4 bar H_2 back pressure, the samples would decompose fully within 2 h compared to over 3 h for the system with no nickel addition. The formation of $MgNi_3B_2$ during the decomposition process was found to encourage further formation of MgH_2 during hydrogenation and cycling of the system was observed to reverse up to 9 wt% which was maintained after 3 cycles.

2.4.2.3 Niobium

It was found that NbO_5 could improve the hydrogen storage properties of MgH_2 [113, 114] which led to Fan *et al.* investigating its use in the $2LiBH_4$:MgH_2 system [115]. They discovered that a Nb_2O_5 dopant in the system allowed 6-8 wt% H_2 to be released below 400 °C and an uptake of 5-6 wt% at the same temperature under 19

bar H_2 after 4 h. During decomposition NbH_2 was formed but the expected MgB_2 was observed below 400 °C. Cycling was studied with 5.16 wt% maintained after 3 cycles. Xiao *et al.* conducted studies using a 5 mol% NbF_5 catalyst [116, 117]. It was observed that 8.1 wt% H_2 could be released below 450 °C with an almost complete reaction of the system taking place. Only LiH and MgB_2 were observed in post decomposition XRD. Reversibility was later investigated and found to be promising with 8.5 wt% taken up within 15 minutes at 400 °C under 65 bar of H_2 pressure. Cycling was similarly good with an average capacity of 8.97 wt% H_2 over 15 cycles. The improvement in properties between NbO_5 and NbF_5 was confirmed by Sabitu *et al.* when they demonstrated that the use of the NbF_5 catalyst could encourage an 80 % decomposition of the system after 6 min compared to 20 min using the NbO_5 catalyst and 30 min for the pure system [118]. Mao *et al.* noted that the formation of $Li_2B_{12}H_{12}$ during decomposition was suppressed when using the NbF_5 catalyst [119].

2.5 Confinement of Lithium Borohydride

A more recent method of improving the hydrogen storage properties of $LiBH_4$ is to use a process called confinement in which the kinetics and/or thermodynamics of the system can be improved. It was first proposed by Vajo *et al.* that the confinement of $LiBH_4$ at the nano scale could improve the reaction kinetics for the destabilisation of complex metal hydrides which are poor owing to their directional ionic/covalent bonding [120]. These poor kinetics are further hampered in thermodynamically tuned systems by the low temperatures utilised as well as the interaction between different species. For their experiments they limited particle size, to reduce diffusion distance, by confining the $LiBH_4$ in a carbon aerogel and found that the decomposition temperature could be reduced by 100 °C. Zhang *et al.* similarly found that mesoporous carbon could be used to nano-confine $LiBH_4$ in which both the thermodynamics and the kinetics were improved [121]. For this system the reaction enthalpy was reduced to 40 kJ mol^{-1} and 3 wt% could be desorbed by 350 °C. Another benefit of using confinement was that little melting of the $LiBH_4$ was observed with some Li_2C_2 formed during the decomposition.

It was noted by Vajo *et al.* that pore size was an important factor in improving the hydrogen storage properties of the confined $LiBH_4$ and later research investigated the use of pores as smal as 2 nm [122–125]. Gross *et al.* continued the aerogel research conducted by Vajo *et al.* and observed a difference between the 13 and 25 nm pore sizes [122]. It was discovered that reducing the pore size and, thus the

particle size of the $LiBH_4$, is able to improve the storage properties. The system with the 13 nm pore size system showed a lower activation energy than the one with 25 nm (103 vs 111 kJ mol^{-1}) and a faster decomposition rate (12.5 vs 7.8 wt% h^{-1}). Fang *et al.* used $LiBH_4$ chemically injected into activated carbon, with a pore size between 1.7 and 3.2 nm, and found that the onset decomposition temperature was reduced to 220 °C [123]. For this system the decomposition rate was increased to 9 wt% h^{-1} and reversibility partially possible with a 6.6 wt% uptake at 300 °C and 50 bar of H_2 pressure. Cahen *et al.* used mesoporous carbon, pore size of 4 nm, and chemically injected the $LiBH_4$ [124]. For this system 3.4 wt% was released within 90 minutes at 300 °C with no intermediate compounds formed during the decomposition. Liu *et al.* used the smallest pore sizes, 2 nm columnar pores, formed from hard carbon during an evaporation self assembly mechanism [125]. This system showed no phase change, usually associated with $LiBH_4$ at 100 °C, and the onset decomposition temperature was reduced to 220 °C. Other benefits of this system were that diborane formation was suppressed from 10^{9} Torr to zero, as was the melting of the $LiBH_4$.

As well as using inert carbon to confine $LiBH_4$, activated confinement materials have also been considered to offer a catalytic effect while reducing particle size. The use of titanium dioxide (TiO_2) has been of particular interest with it used in a mesoporous form, tubular and impregnated into a carbon environment [126–128]. Guo *et al.* first reported the use of TiO_2 as the confinement medium where they investi-

gated it as a mesoporous material [126] . When $LiBH_4$ was chemically injected into the mesoporous TiO_2 the onset decomposition temperature was reduced to 220 °C and peak decomposition was found to occur at 330 °C. Up to 11 wt% was desorbed after 3 h but there was some interaction between the TiO_2 and $LiBH_4$ forming lithium titanates which have been shown to be irreversible. Liu *et al.* used TiO_2 micro-tubes as the confinement medium and investigated different weight loadings between $LiBH_4$ and TiO_2 [129]. For the $LiBH_4$:2TiO_2 system the onset decomposition temperature is reduced further still to 180 °C and the activation energy for the decomposition was reduced to 122 kJ mol^{-1} down from 146 kJ mol^{-1} for bulk $LiBH_4$. The $LiBH_4$:3TiO_2 system caused an onset decomposition temperature of less than 100 °C but similar to the mesoporous TiO_2 lithium titanates were formed. Zhao *et al.* used TiO_2 but impregnated it into a carbon aerogel along with nickel [128]. They found that the two materials in combination helped to release 6.75 wt% H_2 in 120 min at 350 °C and could reduce the activation energy to 118.8 kJ mol^{-1}. However this again showed a reaction between the $LiBH_4$ and TiO_2 to form lithium titanates.

Destabilised systems have also been investigated for confinement with the 2$LiBH_4$:MgH_2 system being the most reported. Nielsen *et al.* first reported the use of the nano-confined 2$LiBH_4$:MgH_2 system where they confined the system in an aerogel with 21 nm pores [130]. They discovered that 4.3 wt% H_2 could be desorbed at 260-470 °C, close to the maximum capacity of the system. Kinetically the system released

3.9 wt% H_2 after 20 h at 390 °C and at 320 °C 74% of the system hydrogen was liberated compared to 26% for the bulk material. Reversibility was investigated with 92% of the system capacity maintained after 3 cycles. Gosalawit-Utke *et al.* investigated the system confined in aerogels but with larger pores of 31 nm [131,132]. They found that 90% of the stored hydrogen could be liberated at 425 °C vs 34% for the bulk material and that the decomposition occurred in a single step. Decomposition started at 250 °C and finished by 400 °C. Reversibility was found to be similar to the Nielsen paper with 3.6 wt% preserved after 4 cycles at 425 °C and 130 bar H_2. Wang *et al.* later reported that when using mesoporous carbon, with pore sizes of 3.5-6 mm, the reversibility of the system was significantly worse [133]. After 3 cycles the relative storage capacity (only taking into account the hydride capacity not system total) had dropped from 10 wt% to 7 wt%. The author attributed this to the two components decomposing separately from each other and not in one step.

2.6 Summary

This literature review has focused on the solid-state storage of hydrogen using the complex metal hydride lithium borohydride. To assess whether a lithium borohydride storage system can meet the DOE's targets properties, such as decomposition temperature, weight capacity and regeneration conditions, were reported and ways to improve these were discussed. While lithium borohydride has an intrinsically high storage capacity its other aspects make it a poor hydrogen storage material such as a

high decomposition temperature and poor reversibility. Currently no modified system has achieved all of the DOE targets, table 1.2, where usually the improvements in reversibility and decomposition come at the expense of the storage capacity of the system and these previously studied systems have been summarised in table 2.1. The aim of this research will be to explores methods for the improvement of the dehydrogenation and hydrogenation of $LiBH_4$ in the solid state while also improving the storage capacity by exploring nickel based additions to form nickel borides, silicon to form either borides or silicides and alternative transition elements to nickel as stated in the aims and objectives on page 32, section 1.4.

Table 2.1: Reaction Conditions for selected thermodynamically tuned $LiBH_4$ systems.

System	Capacity (wt%)	T Dehydrog. (°C)	T(1 bar) (°C)	Cycling Conditions	Reference
$2LiBH_4 + Al \rightarrow LiH + AlB_2 + 3H_2$	7.2	450	-	400 °C/100 bar	[46]
$2LiH + AlB_2 + 3H_2 \rightarrow 2LiBH_4 + Al$	7.6	-	-	300 °C/150 bar H_2/20 hours	[47]
$2LiBH_4 + LiAlH_4 \rightarrow 3LiH + AlB_2 + \frac{9}{2}H_2$	11	149/344	240-300	350°C/85 bar H_2	[48]
$2LiBH_4 + Ni$	17 wt%	> 300 °C	-	600 °C/100 bar H_2	[134]
$2LiBH_4 + CaNi_5 \rightarrow 2LiH + CaH_2 + Ni_3B + Ni_2B + 3H_2$	1.1	220 °C	-	192 °C/85 bar H_2	[55]
$LiBH_4 + 5Mg_2NiH_4 \rightarrow 2MgNi_{2.5}B_2 + 4LiH + 8MgH_2 + 8H_2$	2.6	340	-	< 300 °C/160 bar H_2	[56, 57]
$LiBH_4$ + 10% TiF_3	9.2	250-600	-	-	[59, 60]
$4LiBH_4 + 2SiO_2$ (+ TiF_3 catalyst) $\rightarrow Li_4SiO_4 + 4B + Si + 8H_2$	10	70 - 550	-	500 °C/45 bar H_2	[65]
$LiBH_4 + 0.09TiO_2 \rightarrow 0.18LiOH + 0.82LiH + 0.82B + 0.09TiB_2 + 1.5H_2$	9	100-600	-	600 °C/100 bar H_2	[67]
$2LiBH_4 + MgH_2 \rightarrow 2LiH + MgB_2 + 2H_2$	10	270-340	225	450°C/24 bar	[69]
$LiBH_4 + CaH_2$ (+ 0.25 mol $TiCl_3$ catalyst) $\rightarrow CaB_6 + 6LiH + 10H_2$	9.1	150-400	-	400 °C/83 bar H_2	[77]
$LiBH_4 + CaH_2$ (+ NbF_5 catalyst) $\rightarrow CaB_6 + 6LiH + 10H_2$	9.1	200-400	309	450 °C/80 bar H_2	[78, 79]
$LiBH_4 + 3NaAlH_4$	3.9	210	-	80 bar/180 °C (does not form $LiBH_4$)	[85]
$LiBH_4 + LiNH_2 \rightarrow Li_3BN_2 + 4H_2$	7.8	249	-	-	[88]

Chapter 3

Methodology

3.1 Introduction

This chapter will deal with the experimental techniques used in both sample preparation and material characterisation. Section 3.2 will detail the starting materials and how they were prepared for characterisation. Section 3.3 will cover the materials characterisation broken down into the thermal analysis of samples, structural analysis, hydrogen uptake and scanning electron microscopy.

Table 3.1: As-recieved materials used.

Material	Purity	Supplier
$LiBH_4$	>95 %	Sigma Aldrich
Calcium	99 %	Sigma Aldrich
Nickel	99.9 %	Sigma Aldrich
Nano-nickel	99 %	Sigma Aldrich
Silicon	99.999 %	Alpha Aeser
Titanium Flouride	N/A	Sigma Aldrich
Iron	99 %	Sigma Aldrich
Cobalt	99.9 %	Sigma Aldrich

3.2 Sample Preperation

All samples, listed in table 3.1, were handled and stored inside an MBRAUN Unilab argon filled glove box, to owing to their sensitivity to oxygen and water. The oxygen and moisture levels in the glove box were maintained at less than 0.1 ppm and samples were weighed on a Sartorius CP225D-OCE micro-balance (accuracy 0.01 mg).

Synthesis of $CaNi_5$ alloy started with nickel powder (99.9%, 150m, Sigma Aldrich) and calcium granules (99%, Sigma Aldrich) being measured in a 5:1 molar ratio, for a total mass of 18g, and mixed by agitation. The mixture was loaded into a 22 mm

die and pressed using a Moore hydraulic press at 240 MPa. The resulting pellet was melted using the cold crucible section of an Induction Cold Crucible PSI Hermiga Gas Powder Atomiser, at 450V, for 30 seconds.

For ball milling, samples of 1-2 g were loaded into stainless steel mill pots (volume of 80cm^3) with the lid sealed by a PTFE ring. Electrical tape was used to secure the lid to the pot and to also prevent the ingress of air into the pot. Milling conditions for the different systems are detailed in table 3.2.

Table 3.2: Milling conditions for different systems.

System	Ball-to-Powder Ratio	RPM	Milling Time
$2LiBH_4$:$CaNi_5$	80:1	400	3 hours
$LiBH_4$:xNi	80:1	400	3 hours
$xLiBH_4$:ySi:zTiF_3	60:1	400	1,4,5 hours (5 hours includes 1 hour of soft milling)
$LiBH_4$:xCo	80:1	400	3 hours
$LiBH_4$:xFe	80:1	400	3 hours

Milling conditions for the nickel, iron and cobalt systems were chosen owing to previous studies using $CaNi_5$ showed that 3 hours of ball-milling to be effective in providing sufficient mixing of the two components to encourage the reaction between

the two components. Milling for the silicon systems was increased from 1 an initial one hour milling to four hours to enhance the systems kinetics to increase the possibility of a reaction occurring. An extra hour soft milling to total five hours was also used owing to studies by Abbas *et al.* demonstrating that it was effective in enhancing the reaction between LiH and germanium.

3.3 Sample Characterisation

3.3.1 Thermal Analysis

3.3.1.1 Differential Scanning Calorimetry(DSC)

Different scanning calorimetry (DSC) is the thermoanaytical technique in which changes in a sample's state are determined by the difference in the amount of heat required to raise its temperature compared to an inert reference material. For example when a material starts to melt it requires more energy to be put in as the phase change, from solid to liquid, is endothermic . This change is seen on the DSC curve as a peak in the endothermic direction. The type of DSC used in these experiments is a heat flux DSC with a disc-type measuring system. This set-up uses two measuring discs symmetrical to the centre of the furnace with sensors integrated into the discs which cover the area under the sample holder. When the furnace is heated heat flows to the sample and reference material the initial differential temperature

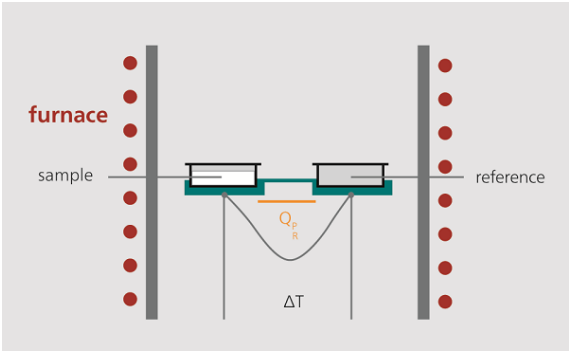

Figure 3.1: Scheme showing the heat flux type DSC used. [136]

signal is zero. Once the heat causes a change to the steady-state equilibrium in the sample then a differential signal is generated proportional to the difference between the heat flow rates of the sample and reference material [135]. A schematic showing demonstrating the configuration of a heat flux DSC is shown in figure 3.1 [136].

For this work DSC analysis was used to identify decomposition events occurring as the multi-component systems were heated using a set ramp rate. Events expected to occur as $LiBH_4$ is heated include the endotherms for the phase change from orthorhombic to hexagonal, the melting of the $LiBH_4$ and finally its decomposition. For the multi-component systems any changes to the temperature at which peaks occur, loss of these peaks or new peaks appearing could all indicate a reaction between the $LiBH_4$ and a secondary component. DSC is also used closely alongside Thermogravimetric analysis (TGA) to correlate mass loss to peaks occurring on the DSC data.

DSC Analysis was performed on a Netzsch 204 HP Phoenix. Samples were prepared in an argon filled glove box where the materials were weighed into alumina crucibles

and sealed within an aluminium pan and lid. The sample was then transferred to the DSC and the aluminium lid was pierced immediately before placing it inside the DSC chamber. Once the chamber was sealed it was flushed 3 times with argon gas (BOC, purity N6.0) after which an argon flow was applied at 100 ml^{-1} under 1 bar of absolute pressure. Samples were decomposed under a heating profile, unless stated otherwise, of a temperature ramp of 30-585°C at 10°C min^{-1}. After decomposition, samples were either removed back to the glove box for further analysis or disposed off. Data analysis of samples was performed on Netzsch Proteus Thermal Analysis software version 4.8.5 (17.06.2009).

3.3.1.2 Thermogravimetric Analysis (TGA)

Thermogravimetric analysis (TGA) is another thermoanaytical technique which is able to see changes in a sample by measuring the weight loss or gain of the sample as it is heated. TGA is a useful technique for the analysis of complex metal hydride storage materials because the primary weight loss usually corresponds to the release of hydrogen from the sample. This technique, in combination with DSC and end product analysis (from XRD or FTIR), can elucidate the reaction pathway as well as the storage capacity of the system. Keeping the decomposition in the solid-state is a key property for using these materials for on-board hydrogen storage so maximising decomposition at temperatures lower than 300°C was prioritised. The TGA analysis here uses a single-sided, isolated balance system, shown in figure 3.2, which means

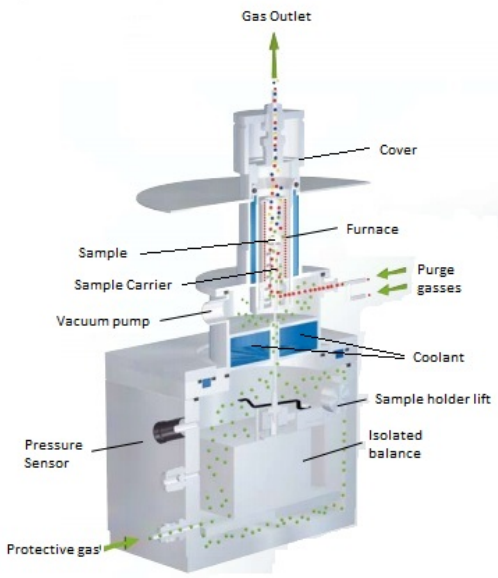

Figure 3.2: Scheme showing the isolated balance away from the sample in the furnace in the TGA. [137].

that a buoyancy test is needed owing to the two different environments the sample and balance are in [137].

TGA analysis was performed on a Netzsch 209 F1 Iris apparatus. Before testing a buoyancy run was performed on the machine using an empty alumina crucible with aluminium pan and lid to provide a correction factor for the separate environments. The apparatus is able to perform an automatic evacuation cycle in which the sample chamber is flushed with argon and vacuumed down prior to any testing performed. A typical TGA measurement begins with a 30 minute isothermal step to allow the balance to stabilise followed by the same heating profile as the DSC measurements to allow direct comparison between the two. Samples were either disposed of or returned to the glove box and data analysis was performed on the Proteus Thermal

Analysis software. For simplicity any mass losses are assumed to be from the release of hydrogen with any other possible species liberated to be investigated in future experiments.

3.3.2 Structural Analysis

3.3.2.1 X-Ray Diffraction

Powder X-Ray diffraction (XRD) is a structural analysis technique that uses X-rays to probe the crystal structure of a material. XRD operates by scattering X-rays off of the electrons in the ordered, crystal structure of a material and measuring the intensity of the resultant x-rays. The regular array of atoms in the crystal structure produces spherical waves and while the majority of these waves are cancelled out from destructive interference while at particular angles constructive interference occurs and is determined by Bragg's law seen in equation 3.1 [138].

$$2\mathrm{d}\sin\theta = \mathrm{n}\lambda \tag{3.1}$$

Here d is the spacing between diffraction planes, θ is the angle of the diffracted X-ray, λ is the wavelength of the wave and n is any positive integer.

For this research XRD has been used to identify the phases present in as-received, post-milling and post-decomposition samples. For as-received samples the main observations are to determine the locations of expected peaks later on such as $LiBH_4$

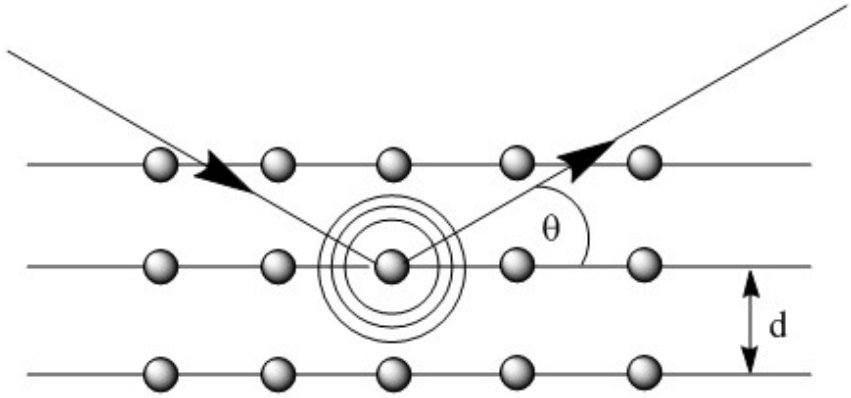

Figure 3.3: Schematic showing the scattering of X-rays by atoms in a crystal structure. Amended from [138].

and the metallic additions to the system. Post-milling samples are observed to determine that the peaks seen during the as-received samples are still present and to determine if any new species have formed during the milling. Finally post-decomposition data is collected to determine if an expected species has formed which would confirm a thermodynamic reaction such as a metal boride. Expected species to form, from the metallic species being added, include nickel borides, silicon borides, lithium silicides, iron borides and cobalt borides.

Powder XRD was performed using a Bruker D8 Advanced XRD. Samples were loaded onto a silicon wafer and covered with an amorphous polymer tape to protect against exposure to the atmosphere. This polymer tape, however, results in an amorphous hump to be present on all samples in the 2θ region of 10-30 °. Data was collected in the 2θ range of 10-80 ° in intervals of 0.05 ° with a dwell time of 4 s. A CuKα source (λ = 1.5418 Å) was used at 40 kV and 40 mA with a 0.6 mm exit slit. Samples were rotated during the experiment to improve measurement

statistics. Data analysis was performed using the EVA software by Bruker and indexed using diffraction data from the ICSD database. XRD was performed on all samples including raw materials, as-milled materials, post-DSC samples and other post-experiment samples.

3.3.2.2 Neutron Diffraction

Powder neutron diffraction (PND) is a technique that is similar to X-ray diffraction where use of neutrons are used instead of X-rays. Neutrons have an advantage over X-rays owing to their null magnetic charge which means they do not interact with the electrons in atoms. This means that lighter elements, such as boron and lithium, can be more easily detected as the neutrons are not scattered from the electron clouds and instead scattered from the nuclei. Unfortunately for neutron diffraction studies isotropically enriched, deuterium based versions of materials are required owing to the large incoherent cross-section of 80.3 barns for hydrogen compared to that of deuterium of 5.6 barns [139].

For this work PND has been used to gain information on the decomposition of $LiBH_4$ systems that XRD cannot. Owing to the ability of PND to more easily detect light elements the tracking of the different states of $LiBH_4$, and other elements present, during *in-situ* testing. PND has been used to observe the phase change of $LiBH_4$, melting of $LiBH_4$ and when it reacts with its secondary component.

Neutron differaction experiments were carried out on the D1B instrument at the

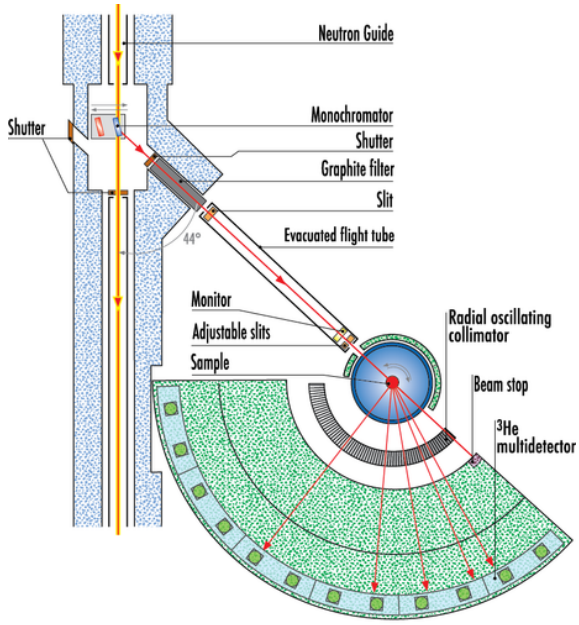

Figure 3.4: Schematic showing layout of the D1B instrument used for neutron diffraction experiments [140].

ILL neutron facility in Grenoble, France. The D1B instrument, shown in figure 3.4, is a two-axis powder diffractometer that is able to produce a high neutron flux of 6.5 x10^6 n cm^{-2} s^{-1} using a pyrolytic graphite monochromator to produce a wavelength of 2.52 Å. The samples of $2^7Li^{11}BD_4$: $CaNi_5$ and $2^7Li^{11}BD_4$:2Ni (2 grams) were loaded into a 316 L stainless steel vessel inside of a glove box. A large sample size is needed to provide sufficient signal to the detectors such that a pattern can be achieved in 5 min with a reasonable signal to noise ratio. The sample was exposed to different conditions including ramp rates of 1°C min^{-1} and isothermal steps, where the sample was either exposed to vacuum or deuterium up to 85 bar of pressure and data was collected in 5 minute time intervals. Pressure above the sample was monitored to determine if deuterium was released during

decomposition and an increase in pressure above the sample was assumed to be solely from released deuterium for these experiments. Data analysis was performed on the Large Array Manipulation Program (LAMP) which was designed by the ILL facility to read and display the large amount of data generated during the neutron diffraction experiments.

3.3.2.3 Fourier Transfer Infra-Red Spectroscopy

Fourier transform infra-red spectroscopy (FTIR) is a technique that probes a materials structure by measuring the amount of absorbed of transmitted IR radiation from a sample over a wide range of wavelengths very quickly. FTIR is able to perform its scanning rapidly by firstly combining many different frequencies of light, using an interferometer, to create an interferogram which is shone at the sample. The incident interferogram is then collected and processed using a mathematical formula, called a Fourier transform, which is able to convert it from an intensity-vs.-time spectrum into an intensity-vs.-frequency spectrum [141].

The specific FTIR technique used in this work is diffuse reflectance infra-red Fourier transform spectroscopy (DRIFTS) in which IR light is reflected off of a powdered sample, with an uneven surface, and collected by using ellipsoid or parabolic mirrors to focus the incident beams, see figure 3.5. When using DRIFTS, samples are often diluted using a non-absorbent material, such as potassium bromide (KBr), if they are too absorbent. Commonly DRIFTS spectra are plotted as Kubelka-Munk

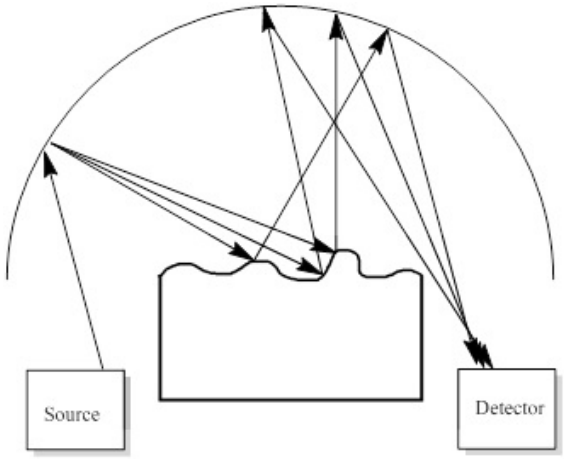

Figure 3.5: Schematic showing the collection of IR radiation produced during DRIFTS. Amended from [143].

vs wavenumber, where Kubelka-Munk is a conversion factor used because DRIFTS bands are stronger than traditional reflectance bands. Kubleka-Munk (K/M) function is derived from the absorption (K) and scattering (S) coefficients of a material and allows the calculation of the diffuse reflectance (R_∞), equation 3.2, or is more simply displayed as the K/M transform, equation 3.3 [142, 143].

$$R_\infty = 1 + \frac{K}{S} - \sqrt{\frac{K}{S}\left(2 + \frac{K}{S}\right)} \tag{3.2}$$

$$\frac{K}{S} = \frac{(1 - R_\infty)^2}{2R_\infty} \tag{3.3}$$

Owing to the covalent nature of the boron-hydrogen bonding in the anion FTIR can be used to determine the presence, or lack-of, $LiBH_4$ in a sample. FTIR was used to determine if decomposition of $LiBH_4$ has occurred for the multi-component systems

while also providing the best proof of its reformation after reversibility studies owing to XRD being poor in observing it when mixed with large amount of heavy elements such as nickel, iron or cobalt.

Diffuse reflectance infra-red fourier transform spectroscopy (DRIFTS) was carried out on a Bruker Tensor 27 using a sealed Pike environment cell (HC-900) with a DiffusIR accessory. Samples were mixed in a 1:5 ratio with potassium bromide, using a mortar and pestle, to dilute the sample. The sample was then loaded into a crucible and sealed inside of the environment cell. Spectra were recorded by scanning for 10 minutes after a KBr background scan had been recorded for the same time.

3.3.3 Hydrogen Uptake Analysis

Hydrogen uptake was measured using a Sieverts apparatus which is a piece of equipment that allows the study of the hydrogen uptake capacity of hydrogen storage materials using volumetric methods. A Sieverts apparatus is usually a bespoke set-up, that varies from lab-to-lab, in which the uptake or release of hydrogen from a sample is measured by the change of pressure when the vessel is exposed to a volume calibrated manifold. The change in the hydrogen pressure during (de)hydrogenation allows the construction of a pressure composition isotherm (PCI) plots which plots the resultant pressure against the calculated weight capacity of the system [144]. A diagram of a typical Sieverts apparatus is presented in figure 3.6.

All PCI experiments are carried out at a set temperature and begin with the V_{ref}

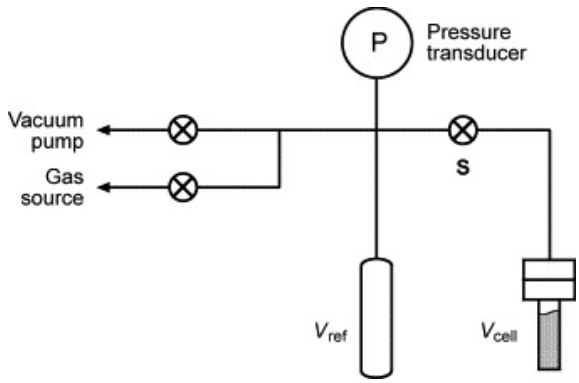

Figure 3.6: Schematic showing the basic set up of a Sieverts apparatus. [144]

cell being filled with a known quantity of hydrogen while being sealed from the V_{cell} using valve **S**. Once the valve is opened the sample in V_{cell} will either release or absorb hydrogen until an equilibrium pressure is reached with the V_{ref}. This is repeated in a step wise fashion over a series of measurements to construct the PCI plot.

A PCI plot is made up of several phases and a stylised PCI plot is shown in figure 3.7. At the beginning of the experiment the material is the alpha phase and very

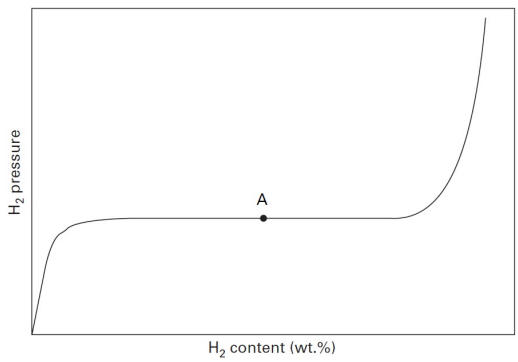

Figure 3.7: Schematic showing a stylised PCI plot where A is the plateau pressure of the hydrogen storage material. [45]

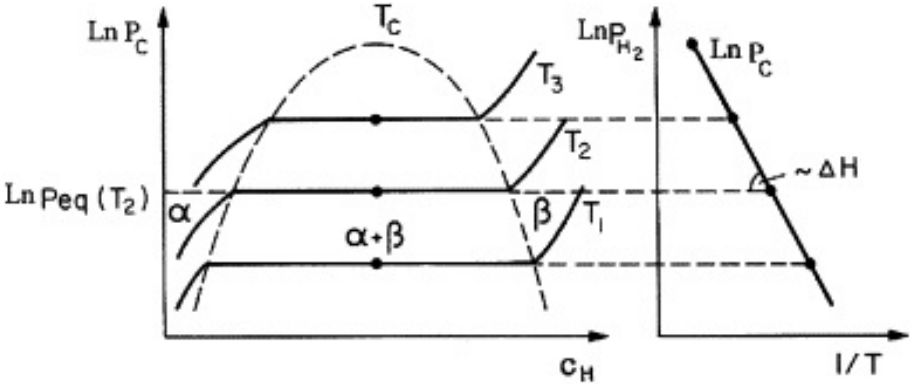

Figure 3.8: Schematic showing the formation of a van't Hoff plot. [146]

little hydrogen is being absorbed by the sample so the equilibrium pressure rises sharply. When the material is saturated with hydrogen a secondary beta phase begins to form which results in a null-rise in pressure, or a plateau, with point A on the graph representing the material's plateau pressure. Once the material has fully converted to the beta phase the weight capacity for the material has been reached and the equilibrium pressure again rises sharply [45, 145].

By performing these PCI measurements at different temperatures a van't Hoff plot can be constructed by plotting the natural logarithm of the pressures ($\ln(p_{\mathrm{eq}})$) against 1/T, shown in figure 3.8. Using the van't Hoff equation, equation 3.4, which is derived from two equations for Gibbs free energy, equations 3.5 and 3.6 , the change in entropy (ΔS) and enthalpy (ΔH) for the system can be calculated [145].

$$\ln(\mathrm{p_{eq}}/\mathrm{p_{eq}}^{0}) = \frac{\Delta \mathrm{H}}{\mathrm{RT}} - \frac{\Delta \mathrm{S}}{\mathrm{R}} \tag{3.4}$$

$$\Delta G = \Delta H - T\Delta S \tag{3.5}$$

$$\Delta G = -RTln p_{eq} \tag{3.6}$$

3.3.4 Scanning Electron Microscopy Analysis

Scanning electron microscopy (SEM) is a versatile experimental technique used in the analysis of the microstructure of solid objects. The reason that SEM is so widely used is that it's resolution is high with top-end research instruments able to achieve 1nm (10 Å) resolution. When an electron beam strikes a sample it produces two types of signals used to produce an image: secondary electrons (SE) and back scattered electrons (BSE). These produced electrons are collected by a detector, off to one-side of the sample, with the sample often tilted towards it. These two types of produced electrons arise owing to different interactions the sample. When elastic scattering occurs when the electron trajectory is changed, but no kinetic energy is lost, this produces BSE. Inelastic scattering results in a change of energy between the two species and thus the secondary electrons are generated. During the interaction of electrons with the material's surface X-rays are also produced which allow for a technique known as energy-dispersive X-ray spectroscopy (EDX) to be carried out. EDX is able to determine the elements present in the sample by analysing the produced X-rays from the electron bombardment and matching them

to their known spectrum [147].

SEM and EDX was used in this work to identify mechanistic properties of the multi-component systems. SEM images were used to identify particles that appeared to contain a mix of two components after which EDX was used to determine the elemental composition of selected areas. Samples were compared between as-milled and those which had been decomposed to determine when mixing and a reaction between the two components has occurred.

SEM experiments were conducted on a Philips XL30 instrument. Samples were prepared inside the glove box where a sticky carbon tab was fixed to an aluminium stub. The sample powder was then either lightly pressed onto the tab or scattered over to achieve either a dense or dispersed distribution. Samples were not coated, to achieve maximum signal in the SEM, and were sealed inside glass vials during transfer to the SEM. When ready to be analysed samples were removed and immediately placed inside the SEM chamber to pump down and prevent excessive oxidation. Scans were taken at 20 kV and using a spot size of 4.

Chapter 4

Results

4.1 Lithium Borohydride As-received

The characterisation of as-received lithium borohydride ($LiBH_4$) is necessary to compare it against the multi-component systems. Figure 4.1 shows the FTIR data for as-received $LiBH_4$. The three peaks observed between 1000 and 1300 cm^{-1} correspond the bending of the B-H bonds in the $[BH_4]^-$ anion and the three peaks between 2200 and 2400 cm^{-1} correspond to B-H stretching [148]. The single peak at 1630 cm^{-1} corresponds to water contamination in the air. Figure 4.2 shows the XRD data for as-received $LiBH_4$. The four most intense peaks observed for $LiBH_4$ are observed at 17.8, 23.8, 24.7 and 26.9 °.

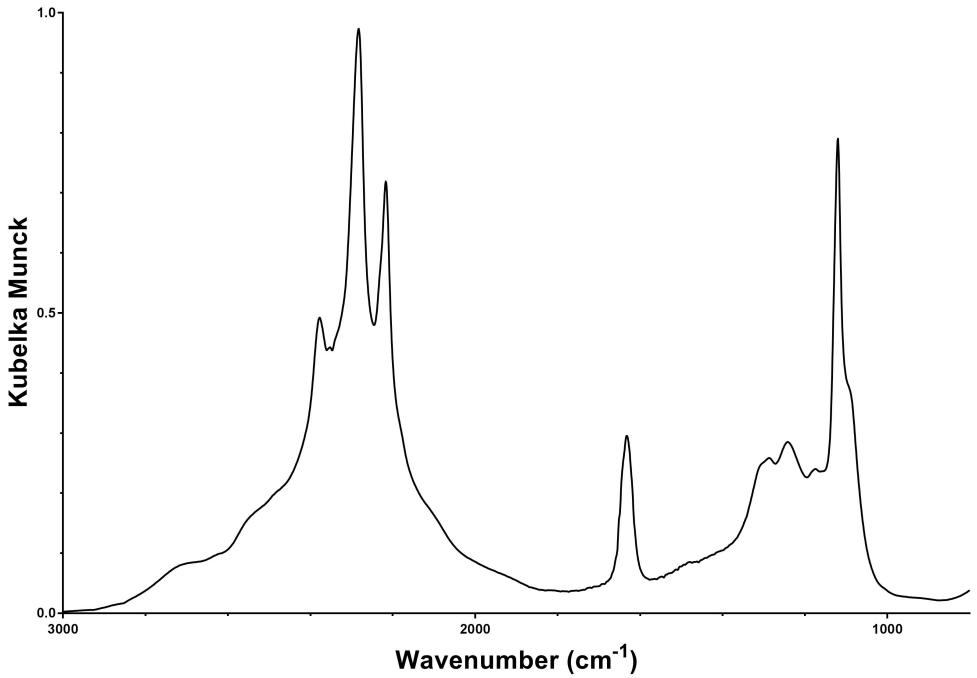

Figure 4.1: FTIR data for as-received $LiBH_4$.

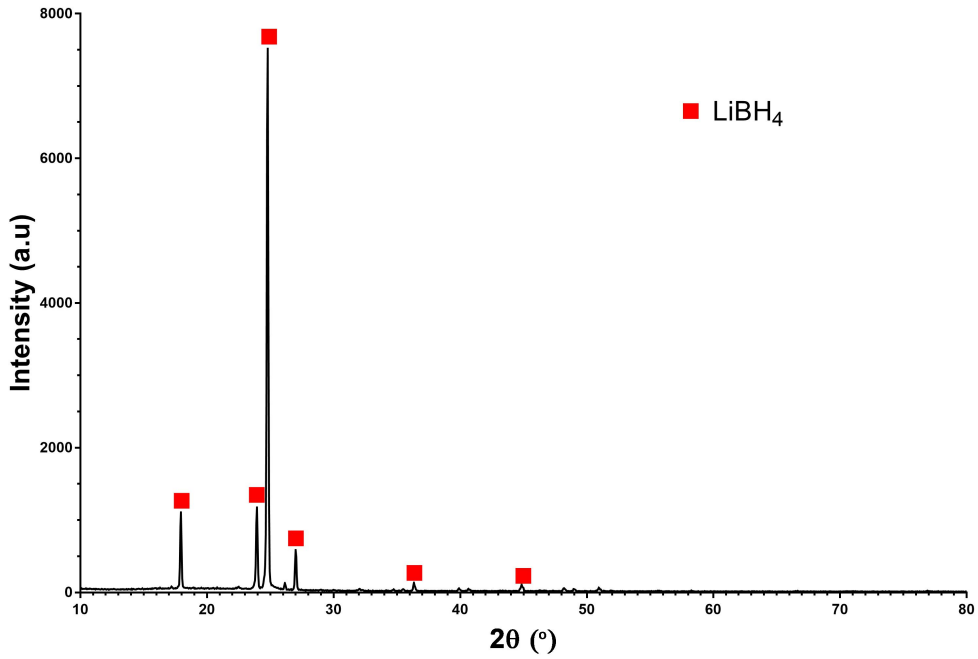

Figure 4.2: XRD data for as-received $LiBH_4$.

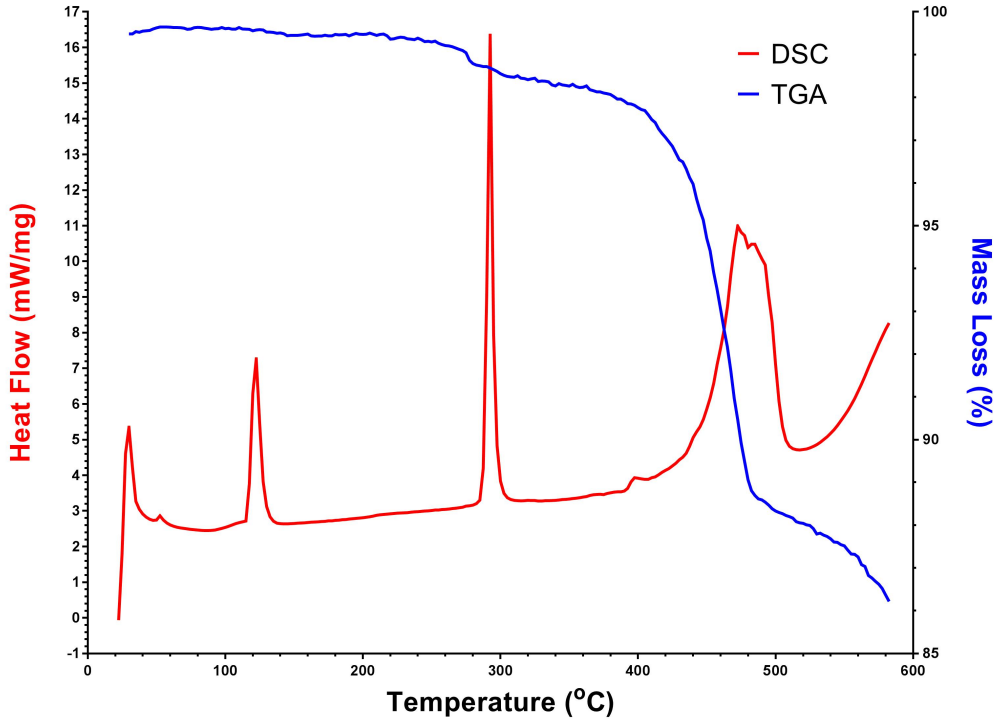

Figure 4.3: TGA and DSC data for as-received $LiBH_4$ heated to 585°C at 10 °C min^{-1}.

Figure 4.3 shows the TGA and DSC data for as-received $LiBH_4$. On the DSC curve a peak is first observed at 120 °C corresponding to the phase change between orthorhombic and hexagonal phase structure. The peak at 300 °C corresponds to the melting of the $LiBH_4$ and occurs at the same time as a 1 % mass loss on the TGA curve. A large, broad peak is next seen between 400 and 520 °C and corresponds to the main decomposition of the $LiBH_4$ and matches the primary mass loss occurring on the TGA curve at the same time. Total mass loss observed by 585 °C is 14%.

4.2 Lithium borohydride and nickel systems

4.2.1 Introduction

In this work the use of elemental nickel was milled with $LiBH_4$ in similar ratios to compare against the use of a $CaNi_5$ alloy. A ratio of 1:3 $LiBH_4$ to nickel was used to investigate a more nickel rich system, a 1:2 ratio for a more nickel lean system, a 1:2.5 system to match that of the use of $CaNi_5$ and a 1:1 system to see whether stoichiometries between that of $CaNi_5$ and previous elemental nickel research were viable. The systems and their theoretical capacities are summarised in table 4.1.

Table 4.1: $LiBH_4$:xNi systems used.

System	Theoretical Storage Capacity (LiH Formation)
$2LiBH_4$:$CaNi_5$	1.6
$LiBH_4$:3Ni	1.53
$LiBH_4$:2.5Ni	1.79
$LiBH_4$:2Ni	2.175
$LiBH_4$:Ni	3.75

4.2.2 Use of Calcium Nickel Alloy

The use of a calcium nickel alloy ($CaNi_5$) is effective in reducing the decomposition temperature of lithium borohydride ($LiBH_4$). Figure 4.4 shows the DSC and TGA data for the $2LiBH_4$:$CaNi_5$ system. From the TGA data it can be seen that onset decomposition for this system is observed at 100°C with the majority of the decomposition finished by 200°C. After 200 °C some decomposition still occurs, but at a much slower rate, with a total mass loss of 1.4 wt% by 585°C. On the DSC curve the decomposition event seen on the TGA corresponds to a small, broad exotherm at 200-220°C. Another two events occur at 500°C and 580°C, with the endotherm at 580°C attributed to the small mass loss at the end of the decomposition.

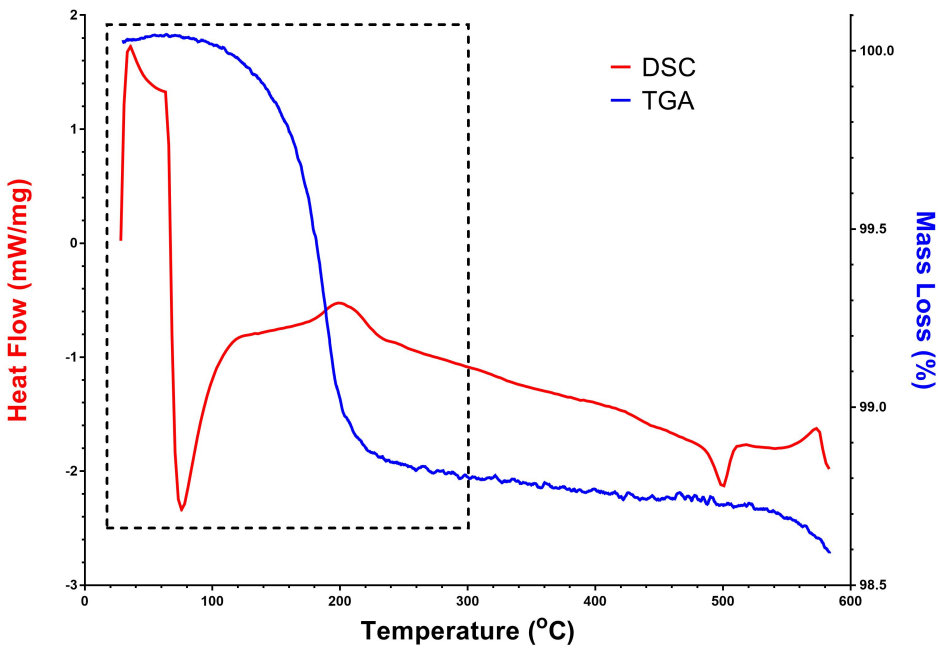

Figure 4.4: TGA and DSC data for the $2LiBH_4$:$CaNi_5$ system heated to 585°C at 10 °C min^{-1}. Dotted box indicates all decomposition occurring below 300°C.

Figure 4.5 shows the TGA and DSC for the $2LiBH_4$:$CaNi_5$ system compared to that of as-received $LiBH_4$. The TGA data has been converted to show the percentage of stored hydrogen released during decomposition owing to the large difference in the mass losses between the two systems (1.4% vs 14%), making it difficult to compare them. From the TGA data it can be seen that the majority of the released hydrogen (60%) for the $2LiBH_4$:$CaNi_5$ system is shown to release by 200°C compared to that of 500°C for the as-received system. The DSC data for $2LiBH_4$:$CaNi_5$ also lacks two distinguishing features of the as-received system: the phase change at 120°C and the melting of $LiBH_4$ at 300°C. The lack of evidence for melting of the $LiBH_4$ is encouraging as it implies that the reaction has been completely carried out in the solid state.

Figure 4.6 shows the powder neutron diffraction (PND) data for the $2LiBD_4$:$CaNi_5$ system. PND was used to confirm the decomposition pathway for the system where the phase change was observed to occur at 162°C, the $LiBD_4$ was found to have fully decomposed by 192°C and nickel borides were found to have formed by 202°C. Evidence for the reversibility of the system was observed, when deuteriding the system at 192°C and 80 bar of D_2, where a small $LiBD_4$ peak started to form. The proposed reaction for this system is presented in equation 4.1 below:

$$2LiBH_4 + CaNi_5 \rightarrow Ni_3B + Ni_2B + CaH_2 + 2LiH + 3H_2 \tag{4.1}$$

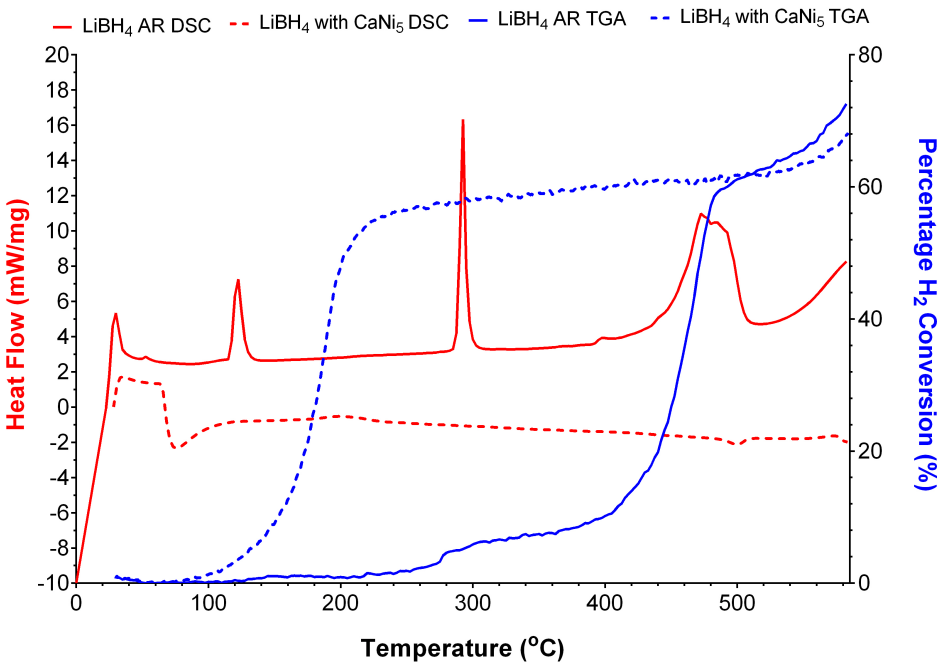

Figure 4.5: TGA and DSC data for the as-received $LiBH_4$ and $2LiBH_4$:$CaNi_5$ systems heated to 585°C at 10 °C min^{-1}. TGA data has been converted from mass loss to percentage of hydrogen liberated from system to more easily compare two systems.

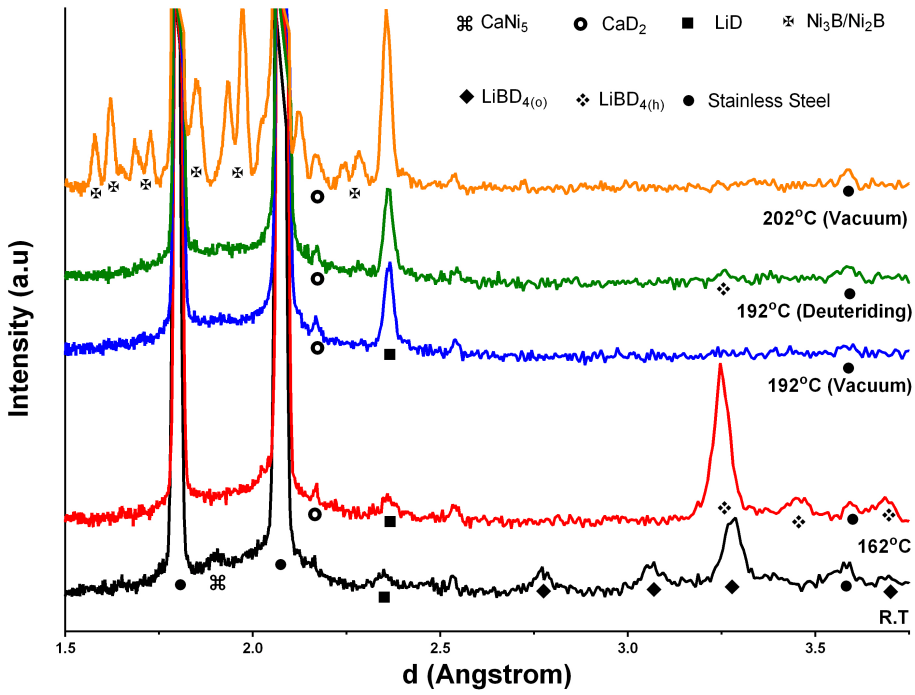

Figure 4.6: PND data for the $2LiBD_4$:$CaNi_5$ system.

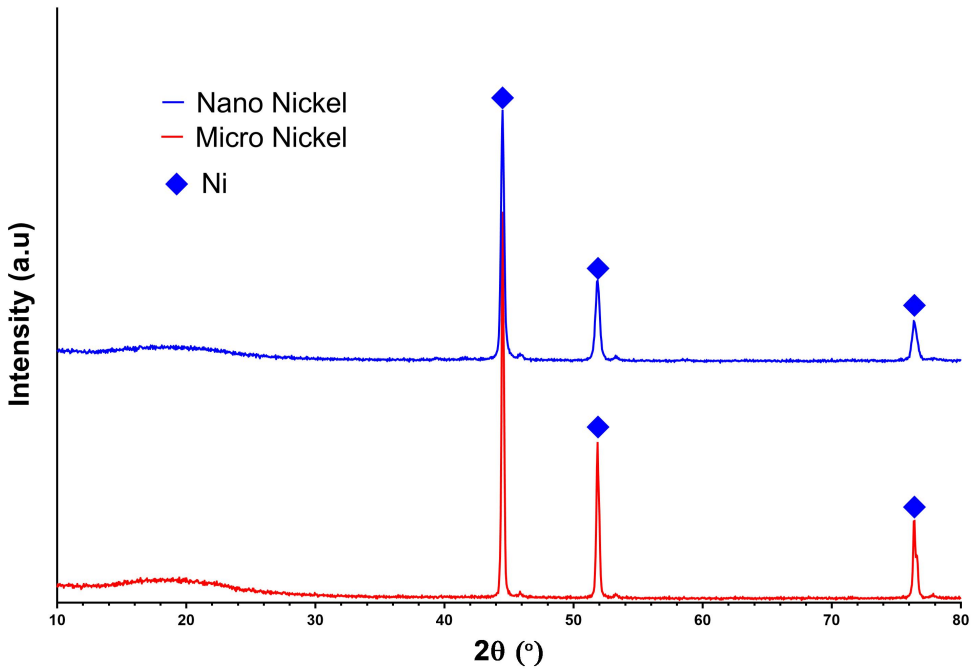

Figure 4.7: XRD data for as-received micro-scale nickel and nano-scale nickel.

4.2.3 Use of Nickel

4.2.3.1 As-received Materials

Figure 4.15 shows the XRD data for as-received nickel at both the micro-scale and nano-scale. On the XRD data three peaks can be seen at 45, 52 and 76 °.

4.2.3.2 Varying Nickel Content

Figure 4.8 shows the X-ray diffraction (XRD) data for the four different nickel systems post-milling. It can be seen that for the Ni system that the nickel peaks are strong and sharp whereas for the the 2, 2.5 and 3 Ni systems they become

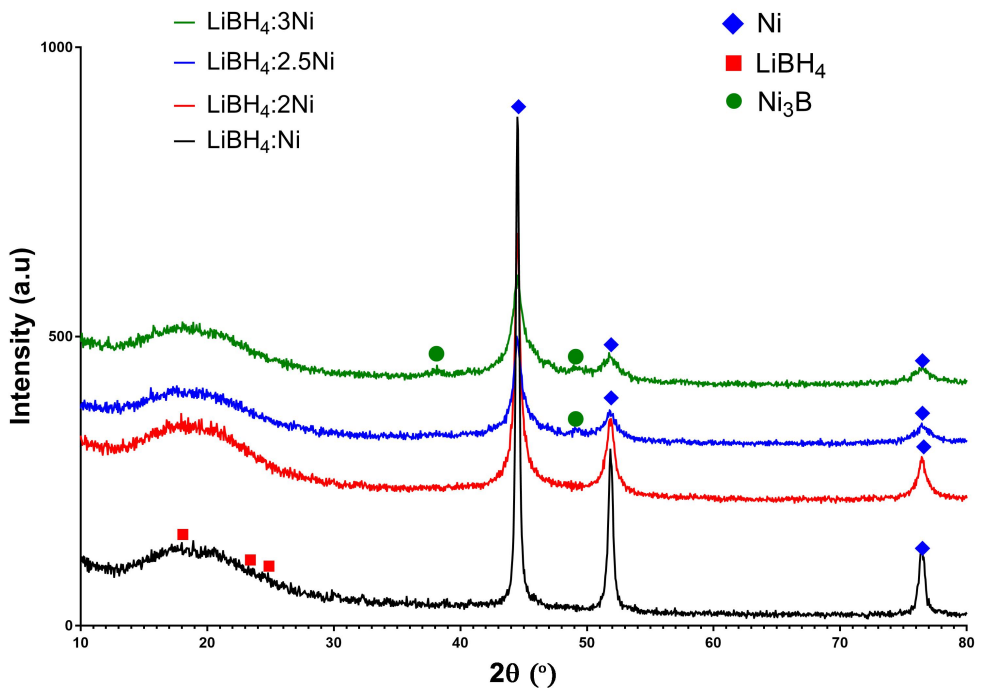

Figure 4.8: XRD data for the four different nickel containing systems post-milling.

less intense and more broad with increasing nickel content. For the 2, 2.5 and 3 Ni systems a small broad peak is observed at 49° corresponding to Ni_3B. This indicates that some decomposition has occurred during the milling process that becomes more apparent with increased nickel content. On the 3 Ni system a second Ni_3B peak is also observed at 39°. $LiBH_4$ is difficult to observe on all of the data owing to its poor X-ray scattering cross-section but some evidence is seen on the 1:1 system with increasing nickel content obscures the peaks further.

Figure 4.9 shows the DSC data for the four different nickel systems. Each system shows the $LiBH_4$ phase change from orthorhombic to hexagonal at 120°C. The three systems with the highest nickel content, 3, 2.5 and 2 Ni, each show a broad decompo-

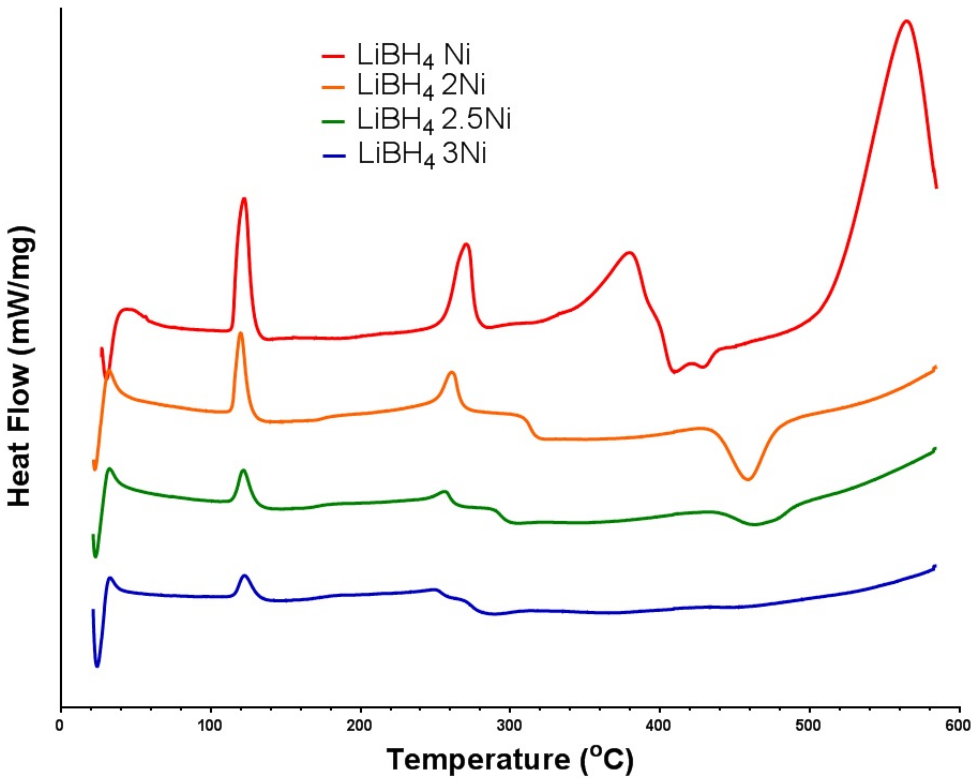

Figure 4.9: DSC data for the four different nickel containing systems heated to 585°C at 10 °C min^{-1}.

sition endotherm starting at 160°C and finishing at 280, 300 and 320°C respectively. For each of these systems the melting of the $LiBH_4$ is still observed but with a less intense peak than that of as-received $LiBH_4$ and usually downshifted compared to the temperature it should occur at, 295°C. The 2.5 and 2 Ni systems also show an exotherm at 460°C which is attributed to a stoichiometric rearrangement and formation of Ni_2B species seen on XRDs, figures 4.12 & 4.13. The Ni system is unique in which, although similar endotherms corresponding to decomposition and a melting are still observed below 300°C, it shows large, broad decomposition endotherms at 380°C and 570°C corresponding to further decomposition.

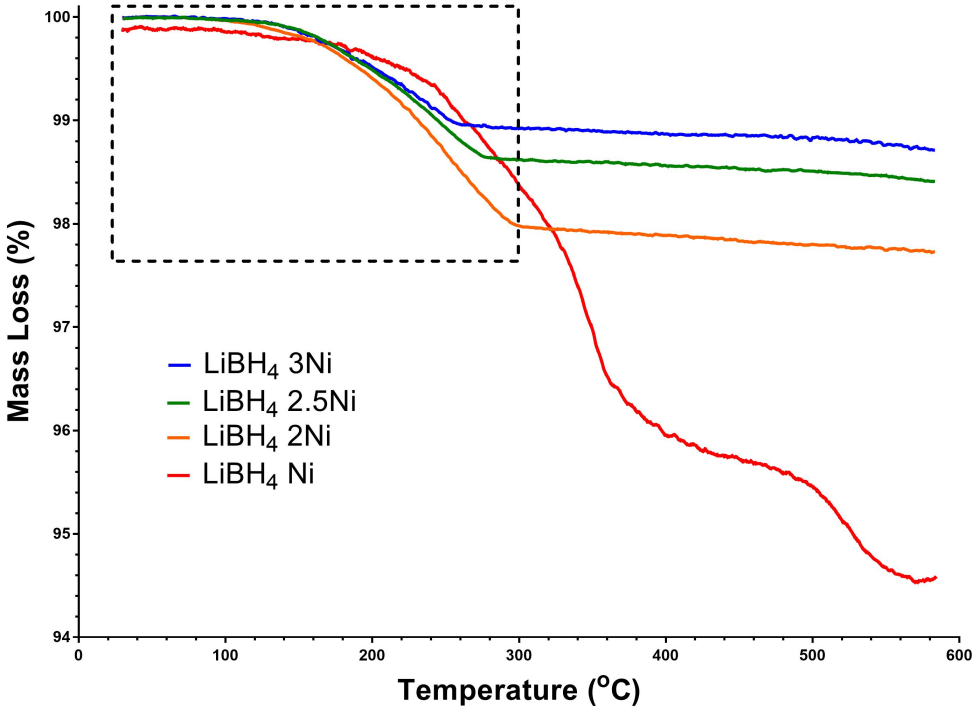

Figure 4.10: TGA data for the four different nickel containing systems heated to 585°C at 10 °C min^{-1}. Dotted box indicates all decomposition occurring below 300°C.

Figure 4.10 shows the TGA data for the four nickel systems. For the Ni system onset decomposition is observed at 200°C with an increase in the rate of decomposition occurring at 260°C. Decomposition for this system slows by 400°C but increases again at 500°C until the end of the reaction. For the other three systems onset decomposition is observed at 140°C and then proceeds rapidly for each system until 260, 280 and 300°C for the 3, 2.5 and 2 Ni systems respectively. After this primary decomposition the systems continue to decompose slowly until the end of the reaction at 585 °C. For the 1, 2, 2.5 and 3 Ni systems the total mass loss by 585°C were 4.5, 2.3, 1.6 and 1.3 wt% respectively and by 300°C, the solid-state temperature of

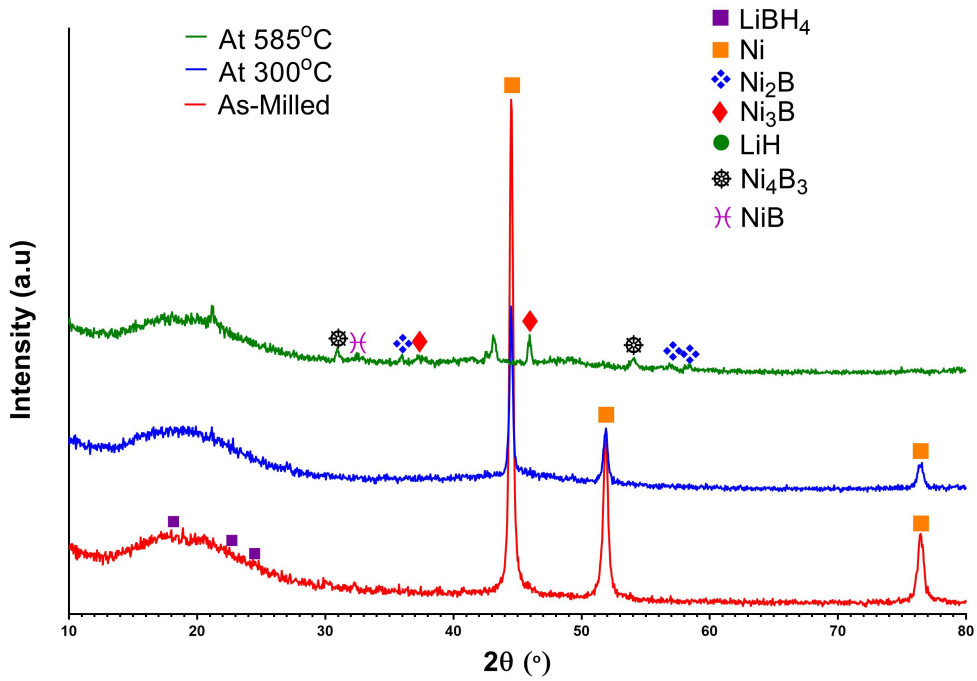

Figure 4.11: *Ex-situ* XRD data for the Ni system showing different stages of the system's decomposition.

$LiBH_4$, 1.6, 2.1, 1.4 and 1.1 wt% respectively.

Figure 4.11 shows the *ex-situ* XRD data for the Ni system. Post-milling the primary species observed is nickel with weak $LiBH_4$ peaks also seen. Upon heating to 300 °C nickel is still the primary species observed but the peaks are weaker. Other peaks are observed but not distinct enough to identify. By 585 °C the nickel species is no longer observed but is instead replaced by several nickel boride species. The stoichiometrically expected species NiB is observed but also Ni_2B, Ni_3B, Ni_4B_3.

Figure 4.12 shows the *ex-situ* XRD data for the 2Ni system. Post-milling the primary species observed is nickel with a trace amount of Ni_3B formed during milling.

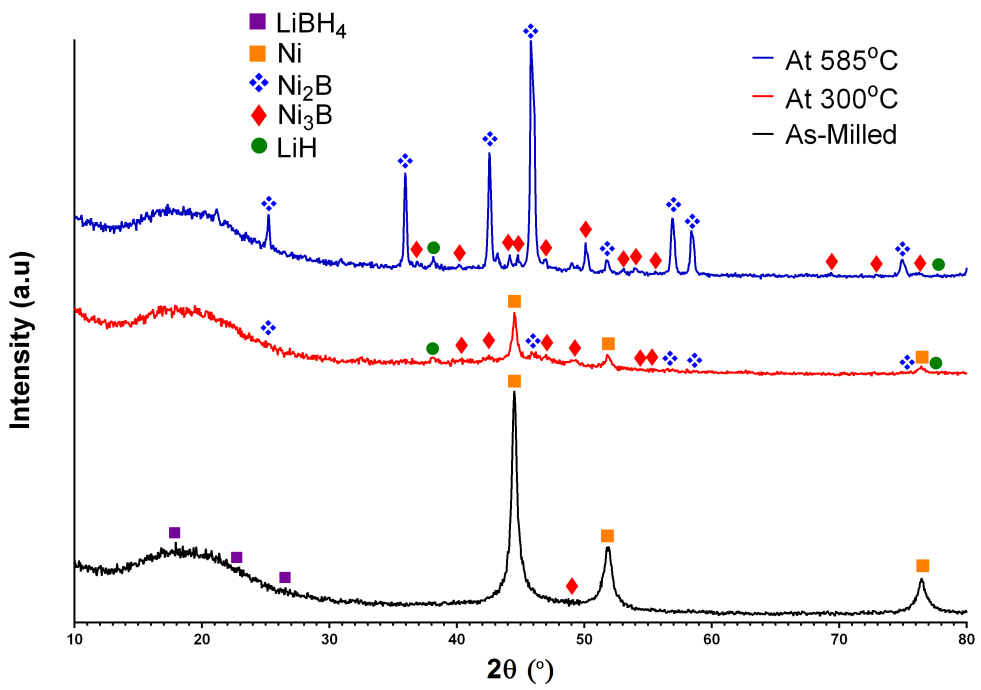

Figure 4.12: *Ex-situ* XRD data for the 2Ni system showing different stages of the system's decomposition.

By 300°C the primary species is still nickel but after decomposition Ni_3B has become the second most intense species. Some Ni_2B is observed but these peaks are either weak or overlapping with Ni_3B peaks. LiH is visible but has weak peaks similarly to $LiBH_4$. By 585°C the primary species now observed is Ni_2B. This is attributed to a stoichiometric rearrangement occurring at 470°C, observed on the DSC data, where the Ni_3B species react with the remaining nickel to form the more stoichiometrically favourable species. Ni_3B and LiH species are still observed but are very weak compared to the primary species and no nickel is observed indicating a complete reaction.

Figure 4.13 shows the *ex-situ* XRD data for the 2.5Ni system. Post-milling the

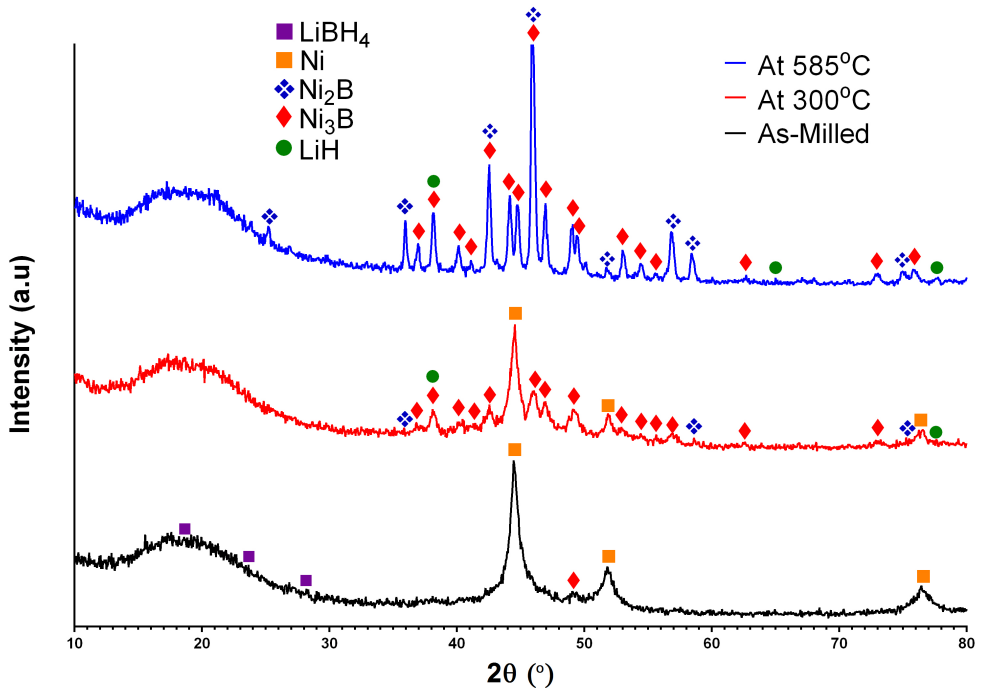

Figure 4.13: *Ex-situ* XRD data for the 2.5Ni system showing different stages of the system's decomposition.

primary species is nickel with trace amounts of Ni_3B formed during the milling process. Once heated to 300°C the primary species observed is still nickel but now Ni_3B is present, shown by multiple peaks. By 585°C the nickel peaks are no longer observed and the primary species is now a mix of Ni_3B and Ni_2B species. This mix arises owing to the stoichiometry of the system and the much smaller stoichiometric rearrangement event observed on the DSC, figure 4.9, is explained by only some of the Ni_3B reacting to form Ni_2B. Some LiH is observed at both 300°C and 585°C but is difficult to observe through XRD owing to its poor scattering ability.

Figure 4.14 shows the *ex-situ* XRD data for the 3Ni system. The primary phase for

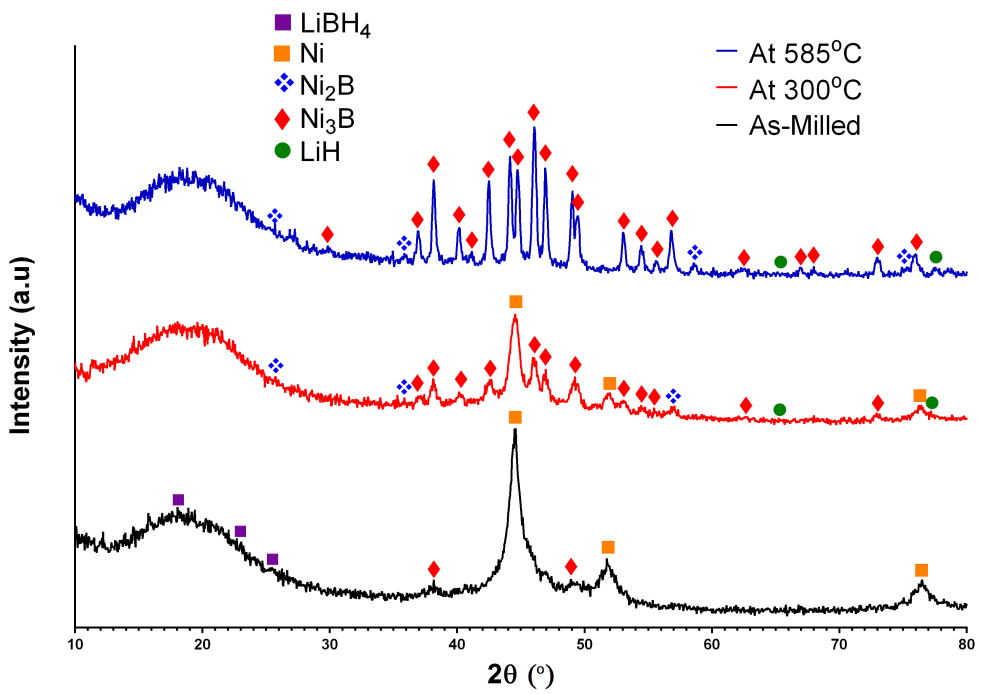

Figure 4.14: *Ex-situ* XRD data for the 3Ni system showing different stages of the system's decomposition.

the post-milling sample is nickel but unlike previous systems a second Ni_3B peak is observed at 38° indicating an increased reaction between the two species during ball-milling. By 300°C nickel is still the primary species but shows a significant decrease in intensity compared to the Ni_3B peaks present in previous systems. By 585°C Ni_3B is the primary species observed with very little Ni_2B observed.

Figure 4.15 shows the FTIR data for the four systems post-decomposition and $LiBH_4$ as-received for comparison. The $LiBH_4$:Ni system does show some weak peaks in the regions in which the $LiBH_4$ peaks occur, with no significant shifting of peaks, but for the other three systems no peaks are observed in the 1000-1400 cm^{-1} region and one small peak in the 2000-2600 cm^{-1} region.

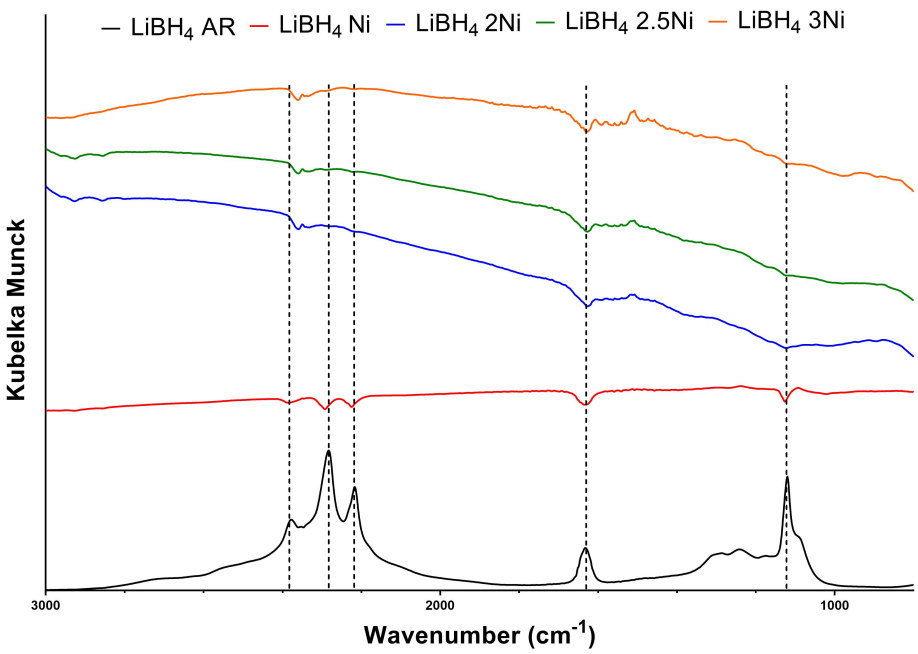

Figure 4.15: FTIR data for the four systems post decomposition up to 585 °C. Dotted lines show any phase shifting of species.

4.2.3.3 Focus on 2Ni system

Owing to the 2Ni system showing the best balance between decomposition temperature and storage capacity it was decided to focus the research on this system. Figure 4.16 shows the DSC and TGA data for the $LiBH_4$:2Ni system decomposed under argon and hydrogen. Heating the sample under hydrogen showed no change in the any of the expected events on either the TGA or DSC data.

Figure 4.17 shows SEM images comparing $LiBH_4$:2Ni system when using micro-scale or nano-scale nickel precursors. After ball-milling, particle size was shown to be similar for both systems and when decomposed, figure 4.18, no significant change in the temperature for any of the events on the DSC data were observed.

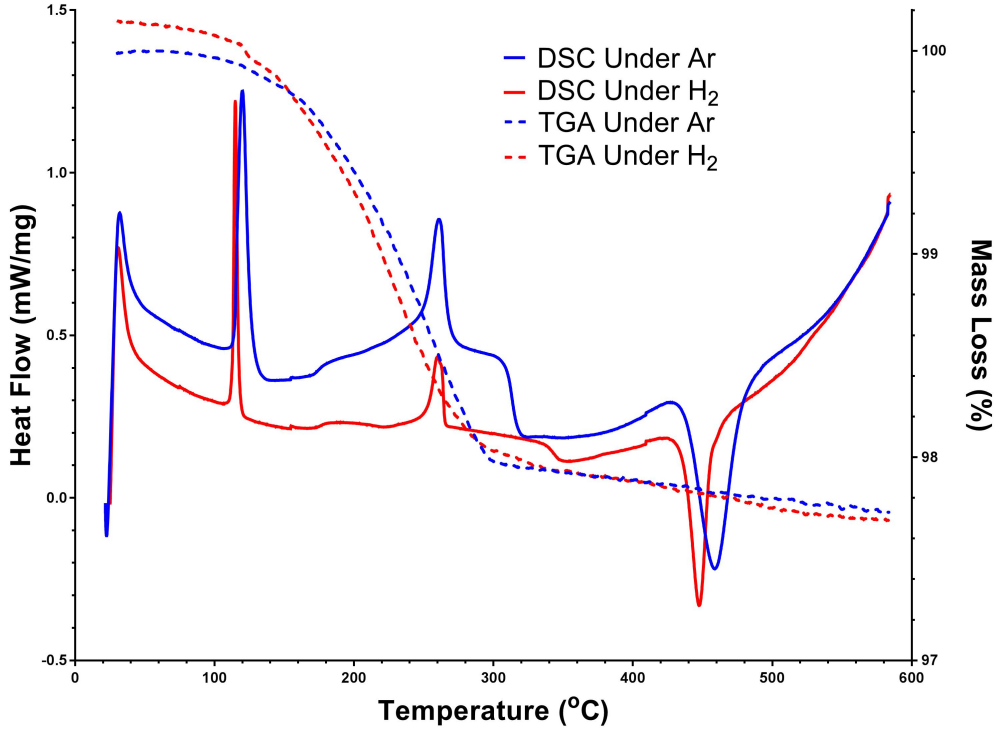

Figure 4.16: DSC and TGA data for the $LiBH_4$:2Ni system heated to 585°C at 10 °C min^{-1} under flowing argon and flowing hydrogen gases.

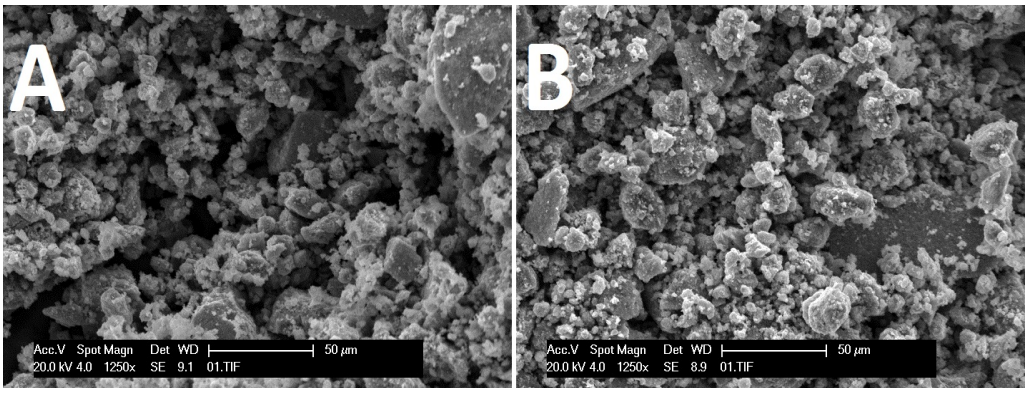

Figure 4.17: SEM data for the $LiBH_4$:2Ni system using (A) micro-scale and (B) nano-scale nickel precursors.

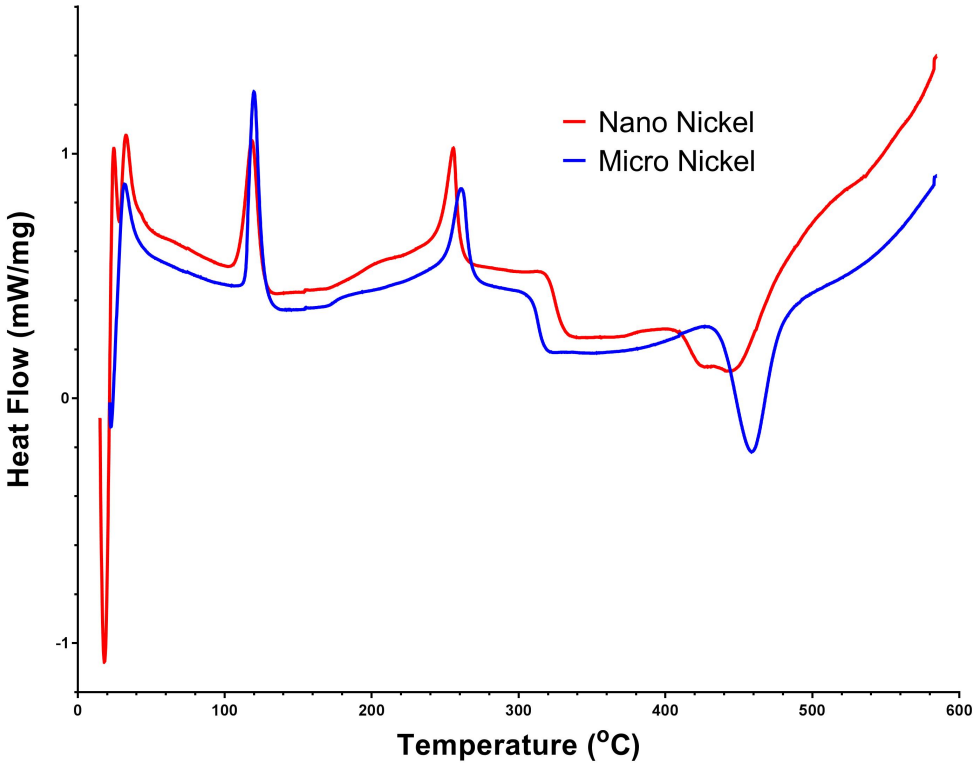

Figure 4.18: DSC data for the $LiBH_4$:2Ni system using micro-scale and nano-scale nickel precursors heated to 585°C at 10 °C min^{-1}.

Figure 4.19 shows the SEM/EDX data for the as-milled $LiBH_4$:2Ni system. While using the back scattered electron detector there is a distinct contrast between lighter and darker areas on particles. Site 1 (A) was chosen as it was a light area implying that it was primarily made of a heavier element. EDX analysis showed that the boron signal was weak (red line) while the nickel signal was strong. Site 2 (B) was chosen as it was primarily a much darker region implying that lighter elements were present. EDX analysis showed that the boron signal was much stronger here and the nickel signal much weaker.

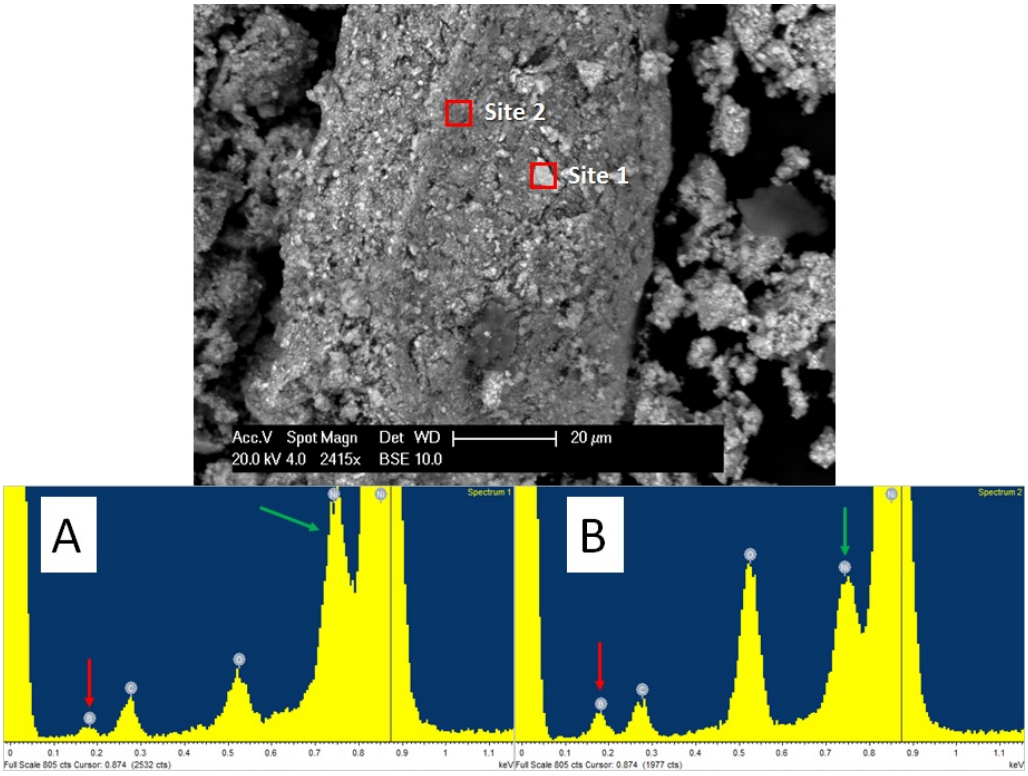

Figure 4.19: SEM data for the as-milled $LiBH_4$:2Ni system. EDX analysis was also performed for site 1 (A) and site 2 (B).

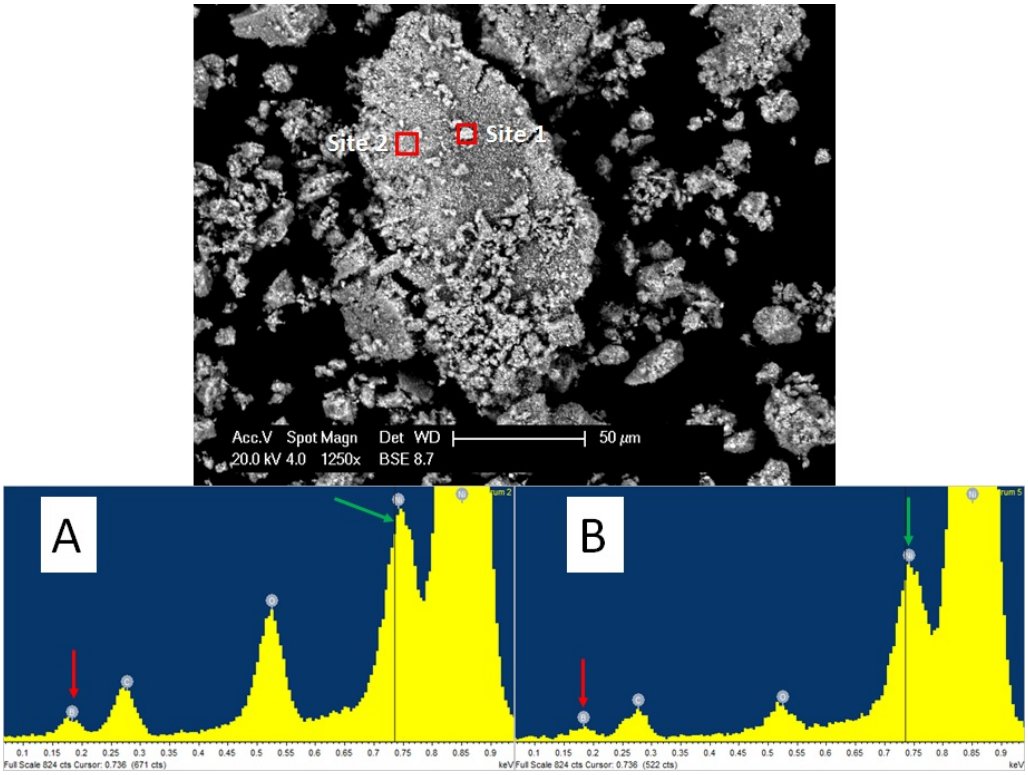

Figure 4.20: SEM data for the decomposed up to 585 °C $LiBH_4$:2Ni system. EDX analysis was also performed for site 1 (A) and site 2 (B).

Figure 4.20 shows the SEM/EDX data for the $LiBH_4$:2Ni system decomposed up to 585 °C. Unlike the as-milled samples dark areas were much more uncommon upon decomposition. EDX analysis (A) on a lighter area showed a weak boron signal, similar to the as-milled sample, but site EDX analysis (B) of a darker area did not show a significant increases in the boron signal strength (when comparing against the carbon signal nearby). The nickel signal was slightly weaker but can be explained by the lower count strength of the EDX scan.

Figure 4.21 shows the *in-situ* powder neutron diffraction (PND) data for the $LiBD_4$:2Ni system. At the start of the experiment $LiBD_4$ is observed in its orthorhombic phase

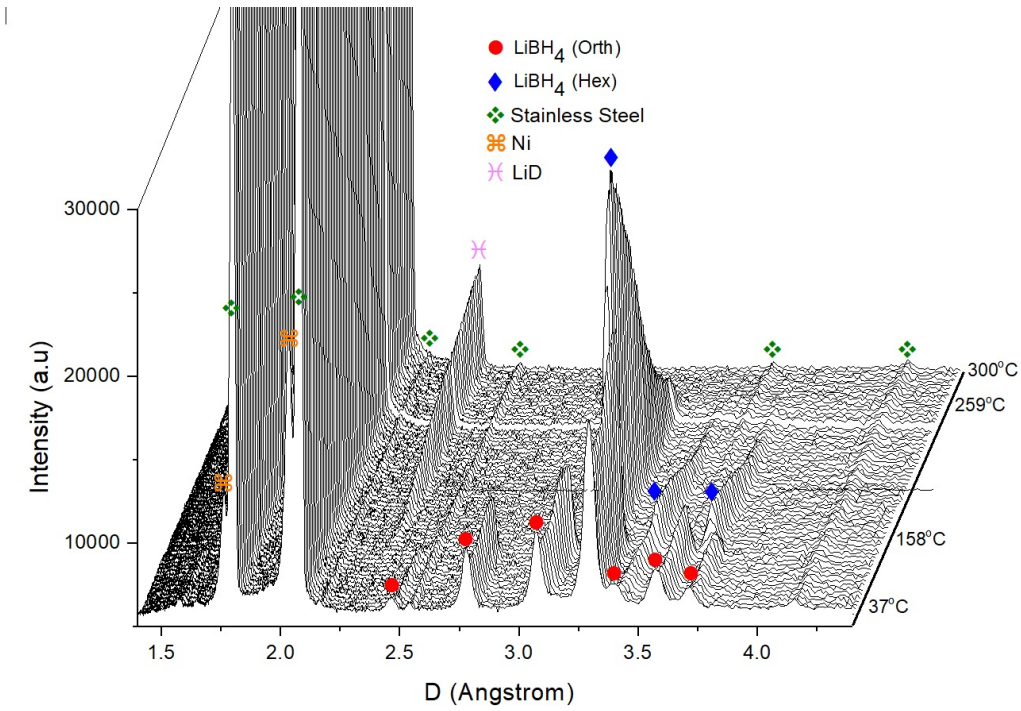

Figure 4.21: *In-situ* PND data for the $LiBD_4$:2Ni system system upon heating to 300°C.

as are two distinct nickel peaks. Upon heating the $LiBD_4$ changed phases to its hexagonal form after which the LiD species started to appear. As the LiD peak continued to grow, the $LiBD_{4(h)}$ peak reduced in size until finally disappearing and being replaced by a broad amorphous hump in the same region.

Figure 4.22 shows selected data from the PND data to highlight particular events during the decomposition. The formation of the nickel boride species is now observable in the region between the two large stainless steel peaks where by 259°C an amorphous hump is observed. However, by 300°C the nickel boride peaks have appeared from this amorphous region. Also at 259°C the broad amorphous hump, between 3.25 and 4 Å, is more easily observed in the region where the $LiBD_4$ peaks

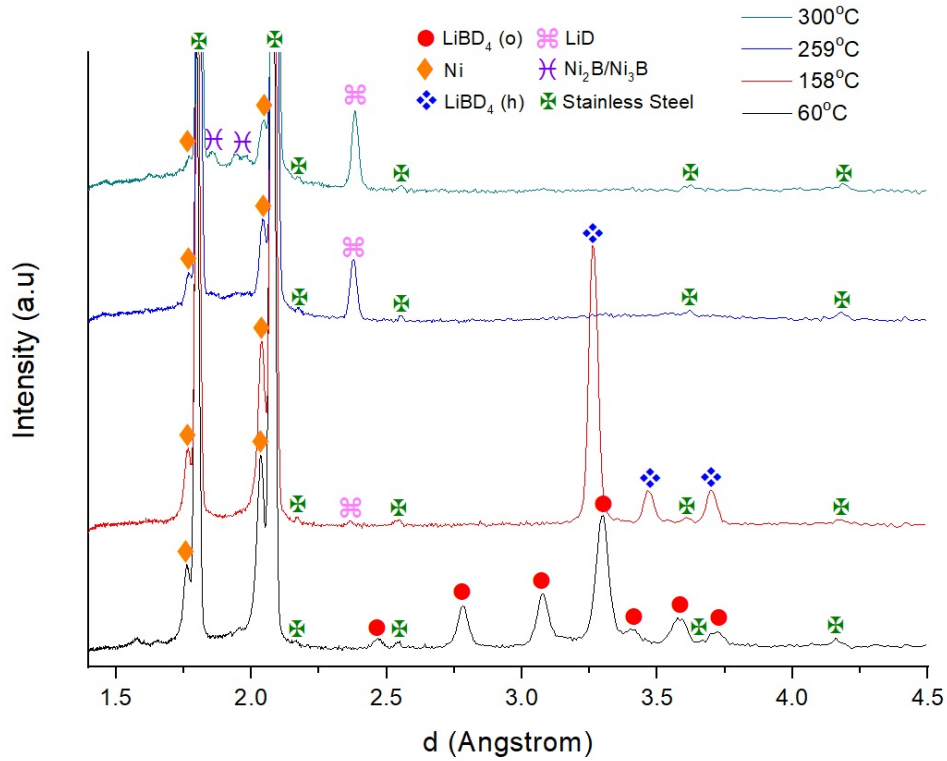

Figure 4.22: *In-situ* PND data for the $LiBD_4$:2Ni system upon heating to 300°C.

were present. The nickel peaks are observed to be reducing in size from 158°C onwards.

Figure 4.23 shows the integrated peak areas for observed species during the reaction and allows the tracking of them during the decomposition reaction. At the beginning of the reaction orthorhombic lithium borodeuteride, $LiBD_4$(o), and nickel are both observed and the peak areas for them remain stable until 120°C until the phase change between $LiBD_4$(o) and hexagonal lithium borodeuteride, $LiBD_4$(h), occurs. By 140°C the $LiBD_4$(h) peak reached its maximum, after which both it and the nickel peaks start to decrease in area as well as the LiD peak appearing and increas-

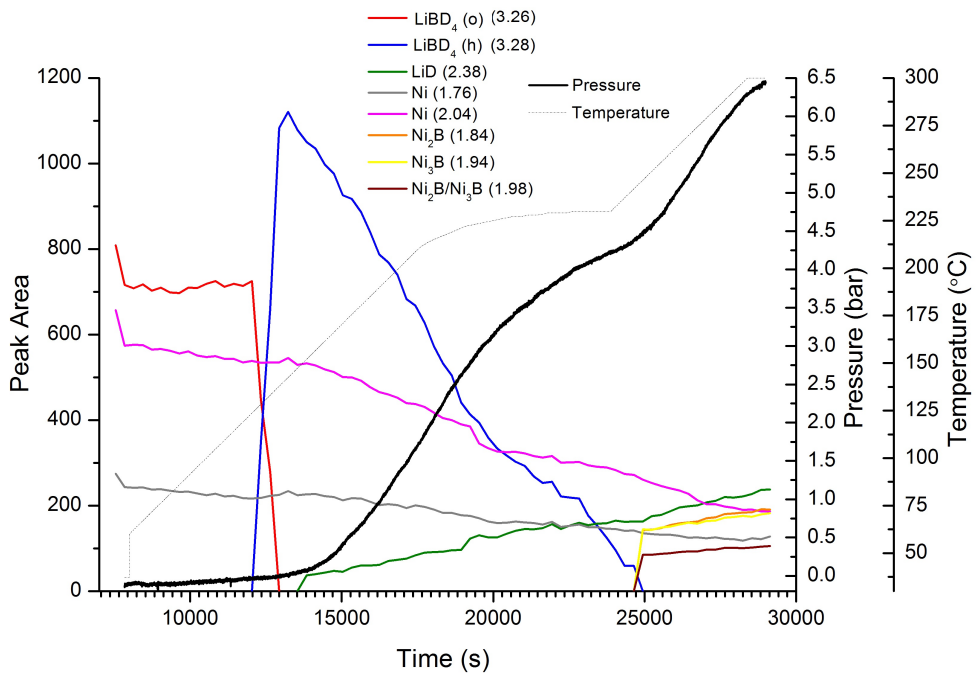

Figure 4.23: Integrated peak areas for species for the $LiBD_4$:2Ni system observed during PND experiments upon heating to 300°C.

ing in area. This decrease in the $LiBD_4$(h) also corresponds to a sharp increase in the amount of D_2 being released from the system indicated by the pressure rise. By 250°C the $LiBD_4$(h) peak was no longer observed but the nickel peaks continued decreasing and LiD peak increasing in area. Also, upon the disappearance of the $LiBD_4$ peak, the nickel boride peaks appeared which continued to increase in area until the end of the experiment.

Further evidence for the melting of the $LiBD_4$ at 260 °C is demonstrated in figure 4.24. Plot A shows the region at which the $LiBD_4$ peaks are observed (2.75 - 4 Å) after which heating to 249 °C shows broad amorphous hump is present too. Upon

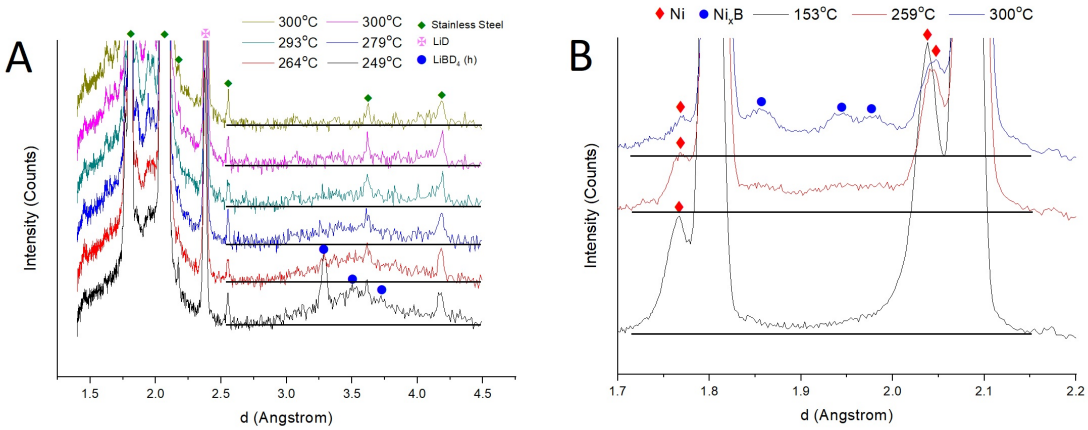

Figure 4.24: Selected PND plots for the $LiBD_4$:2Ni system demonstrating (A) the melting of the $LiBD_4$ at 260 °C and (B) the crystallisation of nickel borides from an amorphous region at the same temperature.

heating further to 264 °C the amorphous hump remains but the $LiBD_4$ peaks are no longer observed. As temperature increases further to 300 °C the intensity of the amorphous hump lessens implying that the $LiBD_4$ continues to decompose but in an amorphous state. Plot B shows the region in which nickel borides are observed at higher temperatures. At 153 °C no amorphous region is present but by 259 °C, a temperature at which the amorphous $LiBD_4$ region can be observed, there is now an amorphous hump seen between the two stainless steel peaks. By 300 ° the nickel boride peaks are seen to emerge from this same amorphous region.

Figure 4.25 shows the isothermal decomposition data carried out on the TGA. When decomposed at 200 °C the system showed a initial mass loss of 1 wt% within 20 min and a total mass loss of 1.4 % within 60 min. When the temperature was increased to 225 °C the 1.4 % mass loss could be achieved within the first 20 min and the

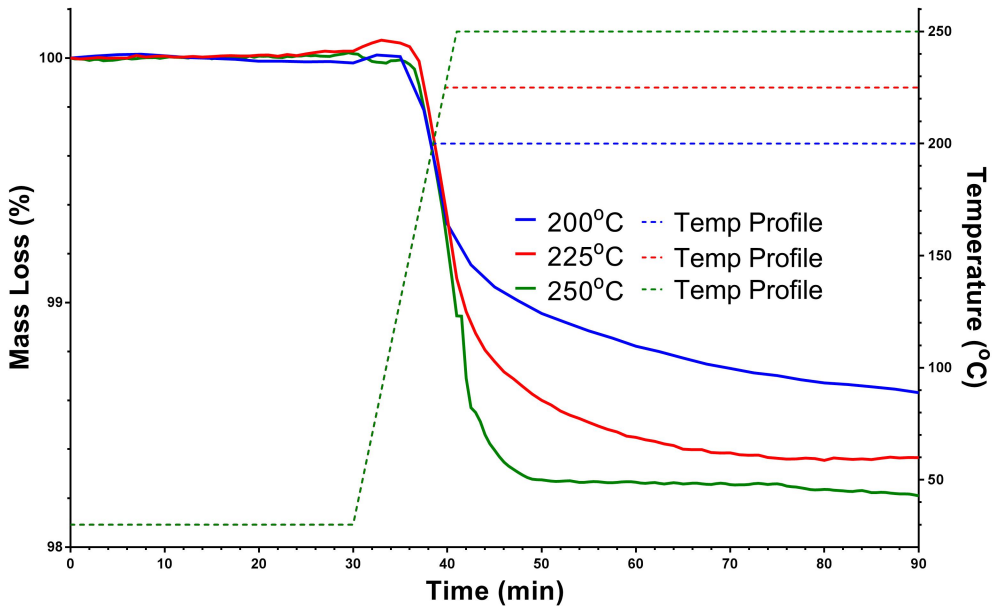

Figure 4.25: Isothermal decomposition data for the $LiBH_4$:2Ni system carried out on the TGA with an initial 30 °C^{-1} ramp rate followed by the isothermal decomposition at the desired temperature.

total loss was increased to 1.6 % after 60 min. Increasing the temperature again to 250°C showed a mass loss of 1.7 % after 20 min which was the majority of the H_2 able to be released at this temperature because after 60 minutes only a further 0.1 % could be liberated. None of the three temperatures shown here were able to reach the 2.1 wt% system capacity when decomposed at higher temperatures.

Figure 4.26 shows the FTIR data for the $LiBH_4$:2Ni system decomposed during the isothermal decomposition experiments at 200, 225 and 250 °C. All three spectra show inverted peaks in the location of expected borohydride peaks, as seen on the as-milled data, and the intensity of these peaks get weaker as the temperature at which the experiments carried out increases. No significant shifting of the peaks was

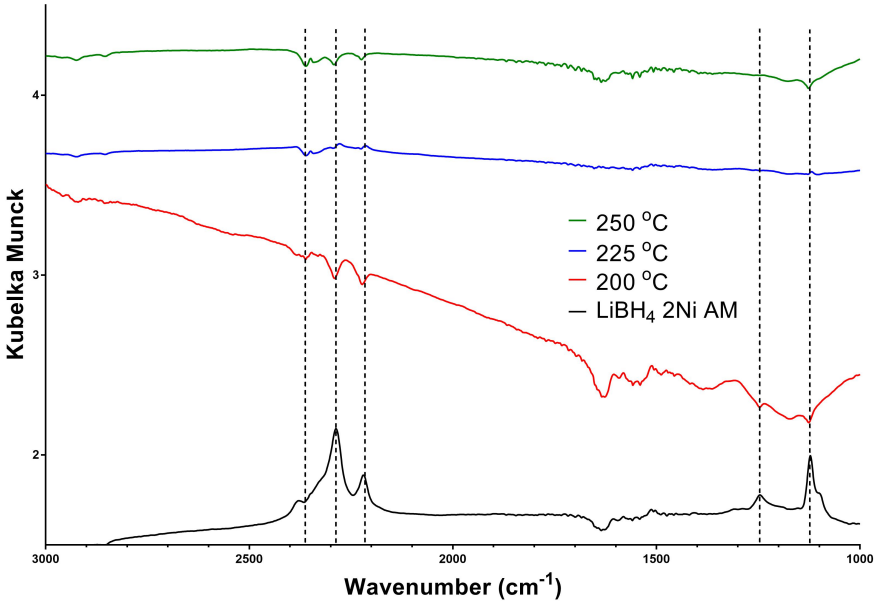

Figure 4.26: FTIR spectra for the $LiBH_4$:2Ni system after isothermal experiments at different temperatures. Dotted lines show any phase shifting of species.

observed between the three temperatures.

Figure 4.27 shows the XRD data for the $LiBH_4$:2Ni system decomposed during the isothermal decomposition experiments at 200, 225 and 250 °C. For the 200 °C sample the nickel peak is the prominent species present with some weak signals observed for both the Ni_2B and Ni_3B species. Upon increasing the temperature to 225 °C nickel is still the dominant species but the nickel boride peaks are now much more obvious. When the temperature was increased again to 250 °C the nickel peak intensity was now reduced when compared to the nickel boride species.

Figure 4.28 shows the hydrogenation isotherms for the $LiBH_4$:2Ni system at 200, 225 and 250 °C. Total uptakes at the three temperatures were observed to be 1.42 %

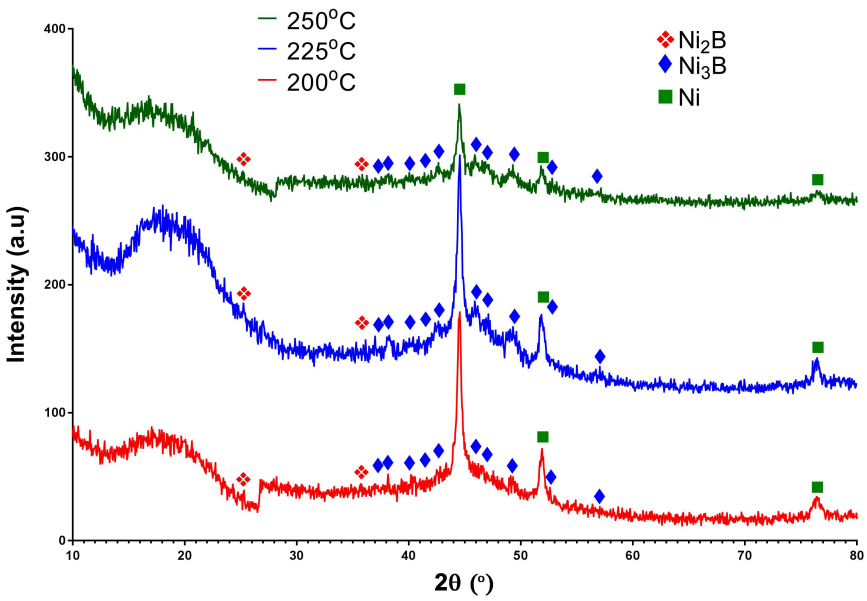

Figure 4.27: XRD data for the $LiBH_4$:2Ni system after isothermal experiments at different temperatures.

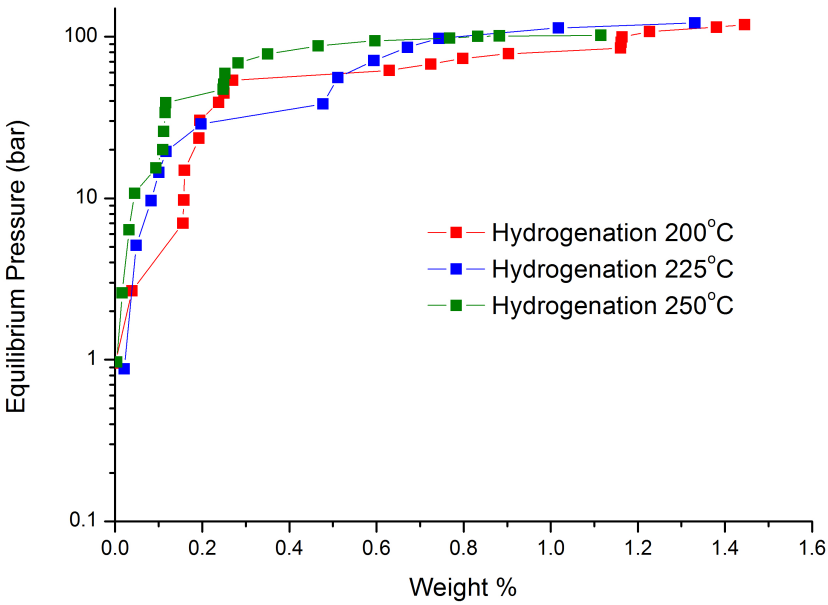

Figure 4.28: Hydrogenation isotherms for the $LiBH_4$:2Ni system at 200, 225 and 250 °C.

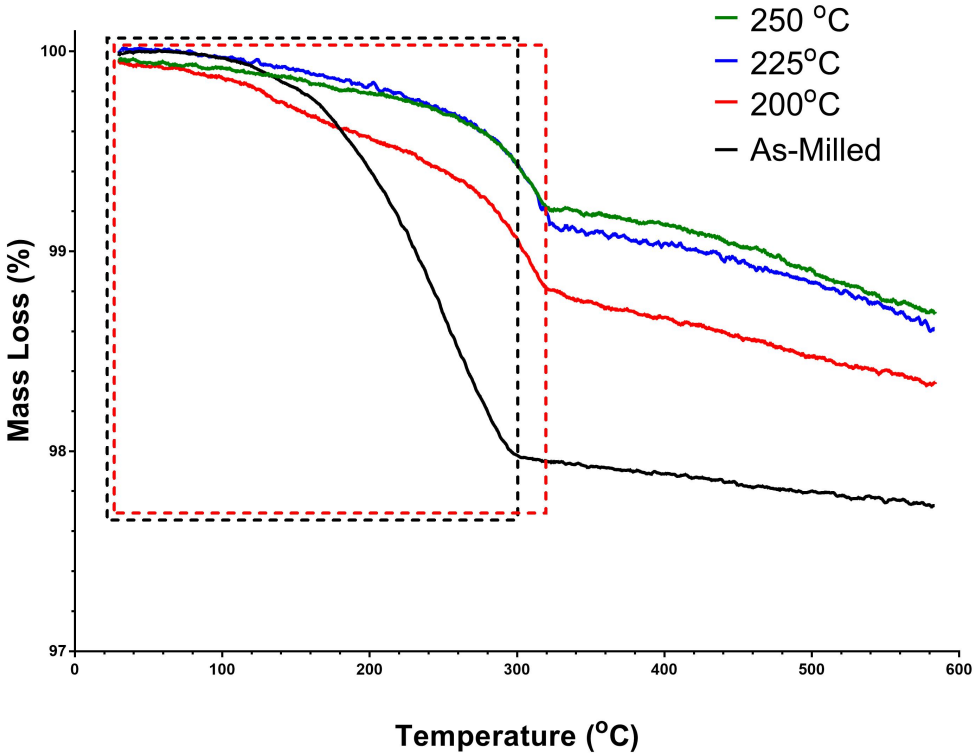

Figure 4.29: Post-hydrogenation TGA data for the $LiBH_4$:2Ni system at 200, 225 and 250 °C compared against the as-milled system. Samples were heated to 585 °C at 10 °C min^{-1}. Black dotted box shows decomposition up to 300°C and red dotted box shows decomposition up to 320°C.

at 200 °C, 1.32 % at 225 °C and 1.1 % at 250 °C. Complete PCIs were not possible owing to the limited bottle pressure on the available apparatus.

To further quantify the hydrogen uptake for the system a post-hydrogenation TGA assessment was performed, shown in figure 4.29. All three systems show a similar shaped curve to the as-milled sample with the majority of decomposition finished by 320 °C (compared to 300 °C for as-milled). Mass losses were 1.6 % for the 200 °C sample, 1.4 % for the 225 °C samples and 1.3 % for the 250 °C sample.

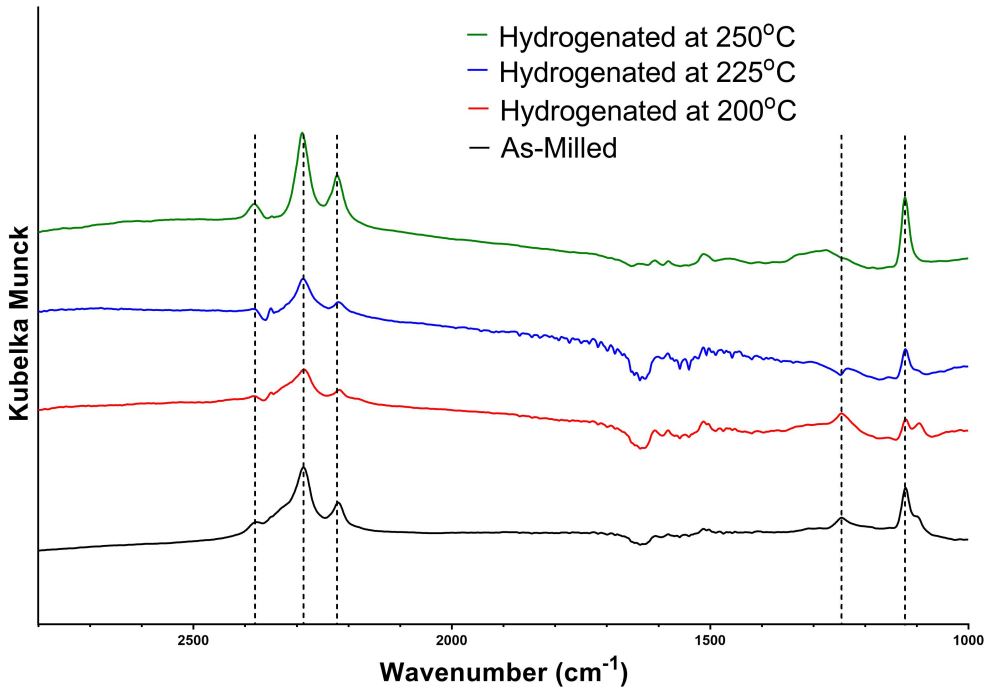

Figure 4.30: Post-hydrogenation FTIR data for the $LiBH_4$:2Ni system at 200, 225 and 250 °C compared against the as-milled system. Dotted lines show any phase shifting of species.

FTIR was also performed to confirm the presence of $[BH_4]^-$ species post-hydrogenation, shown in figure 4.30. The as-milled sample shows expected $[BH_4]^-$ bending peaks at 2215, 2287 and 2382 cm^{-1} and stretching peaks at 1120, 1244 and 1312 cm^{-1}. The three hydrogenated samples also show peaks at each of these locations with no significant shifting of the peaks.

4.3 Lithium Borohydride and Silicon Systems

4.3.1 Introduction

In this section two approaches were used to destabilise $LiBH_4$ using silicon. Firstly the silicon was used to attempt to form silicon borides, upon reaction with $LiBH_4$, not seen in previous experiments using SiO_2. Secondly efforts were made to react the silicon with the lithium to form lithium silicides in a reaction similar to previous papers, using SiO_2 , or Ge, with the addition of a TiF_3 catalyst to encourage the formation of LiH first.

4.3.2 As-received materials

Figure 4.31 shows the XRD data for as-received silicon to compare against later samples. Peaks can be seen at 28.3, 47.3, 56.5, 69.1 and 76.4 °. Figure 4.32 shows the as-received XRD data for the TiF_3 catalyst. Peaks can be seen at 23, 32.5, 33.2, 38.7, 47.3, 53.2, 59, 68.3, 69.6 and 74.4 °.

4.3.3 Reaction Between Silicon and Boron

4.3.3.1 One Hour Ball-Milling

Figure 4.33 shows the XRD data for the 1 hour ball-milled $6LiBH_4$:Si system. Peaks can be seen for both $LiBH_4$ and Si as expected. Figure 4.34 shows the DSC and

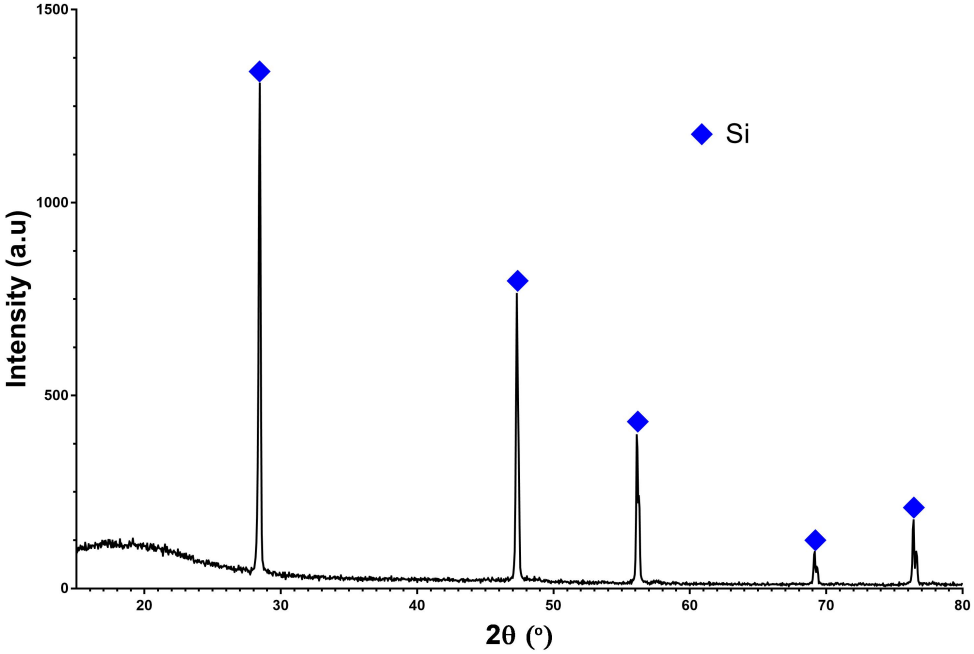

Figure 4.31: XRD data of as-received silicon powder.

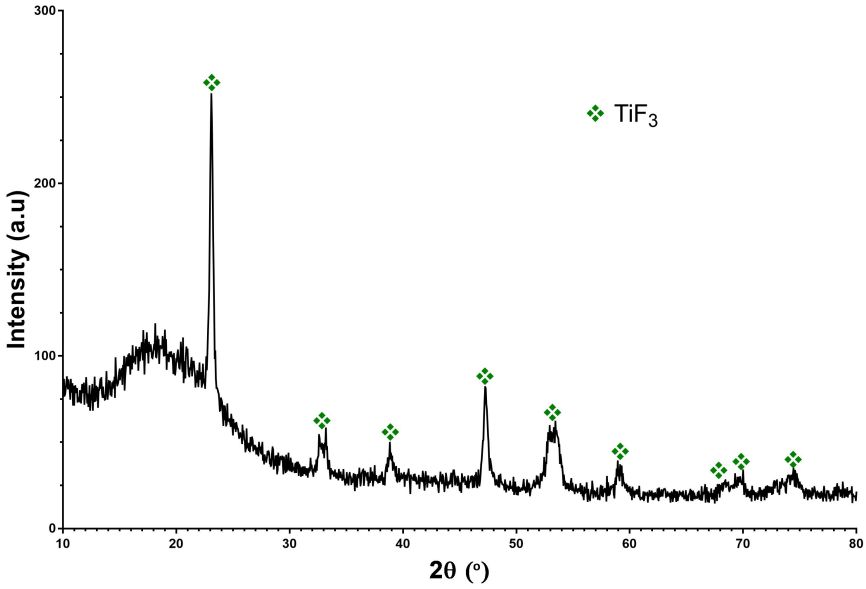

Figure 4.32: XRD data of as-received titanium fluoride powder.

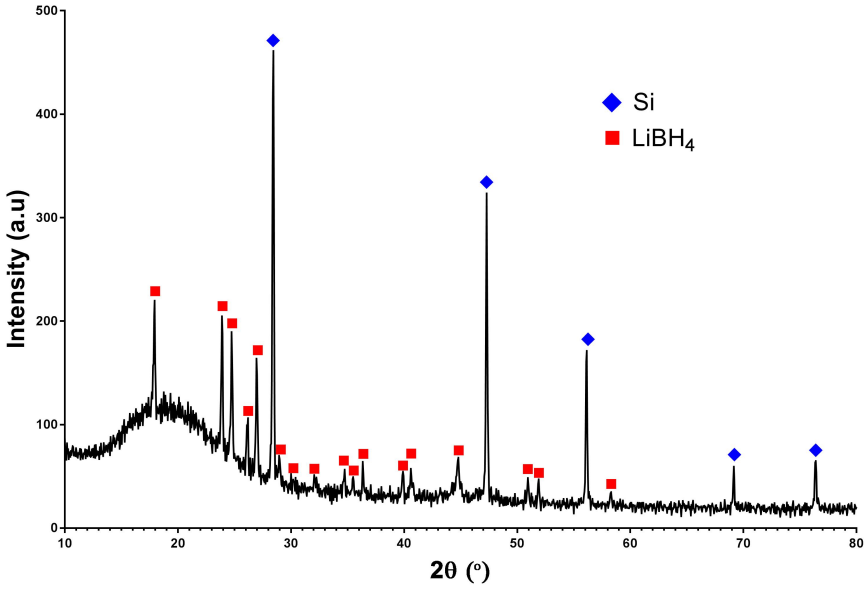

Figure 4.33: XRD data for the 1 hour ball-milled $6LiBH_4$:Si.

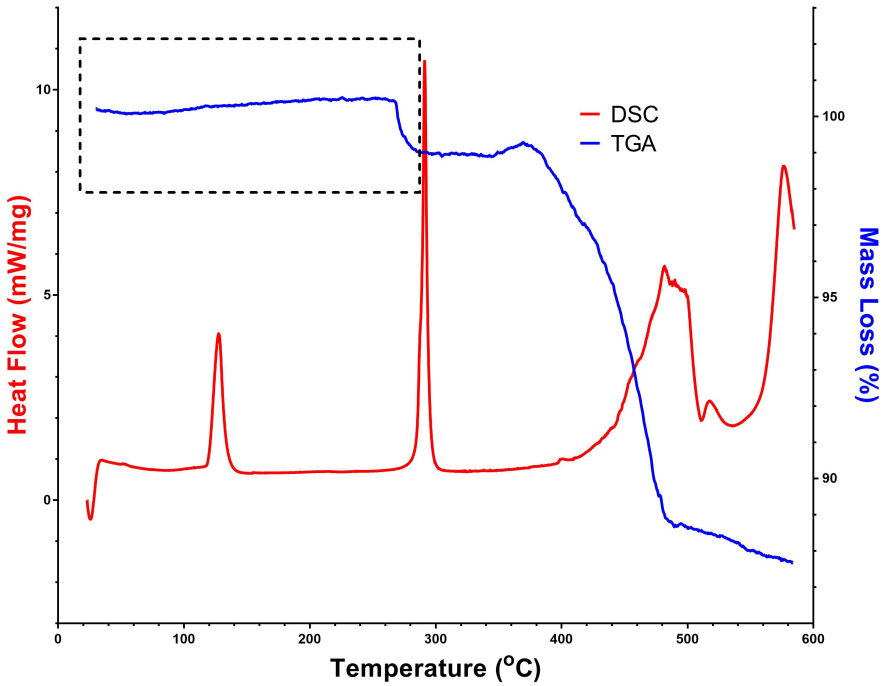

Figure 4.34: DSC and TGA data for the 1 hour ball-milled $6LiBH_4$:Si system heated to 585°C at 10 °C min^{-1}. Dotted box indicates decomposition occurring within the solid-state.

TGA for the system heated to 585°C at 10 °C min^{-1}. The peak on the DSC at 130 °C corresponds to the orthorhombic to hexagonal phase transition of the $LiBH_4$. At 295 °C the melting of the $LiBH_4$ is observed which matches a mass loss of 1 % seen on the TGA data. Between 400 °C and 500°C the main decomposition of the $LiBH_4$ is seen on the TGA which matches the large broad endotherm observed on the DSC. Foaming of the sample during decomposition did not allow post-decomposition analysis.

4.3.3.2 Four Hours Ball-Milling

Figure 4.35 shows the XRD data for the as-milled $6LiBH_4$:Si, $3LiBH_4$:Si and $LiBH_4$:Si systems. Each system shows the expected peaks for both $LiBH_4$ and Si with decreasing intensity of the $LiBH_4$ signal compared to the Si as the ratio of $LiBH_4$ decreases from 6:1 to 1:1.

Figure 4.36 shows the TGA and DSC data for the four hour ball-milled $6LiBH_4$:Si system. The orthorhombic to hexagonal phase transition is observed on the DSC data at 120 °C followed by the melting of the $LiBH_4$ occurring at 295 °C. Upon melting the $LiBH_4$ begins to decompose, observed by the mass loss event on the TGA, and continues to decompose until 500 °C. This event also corresponds with the large, broad decomposition peak on the DSC data. The mass loss for the system was observed to be 15 wt% and foaming of the sample did not allow for post-decomposition analysis.

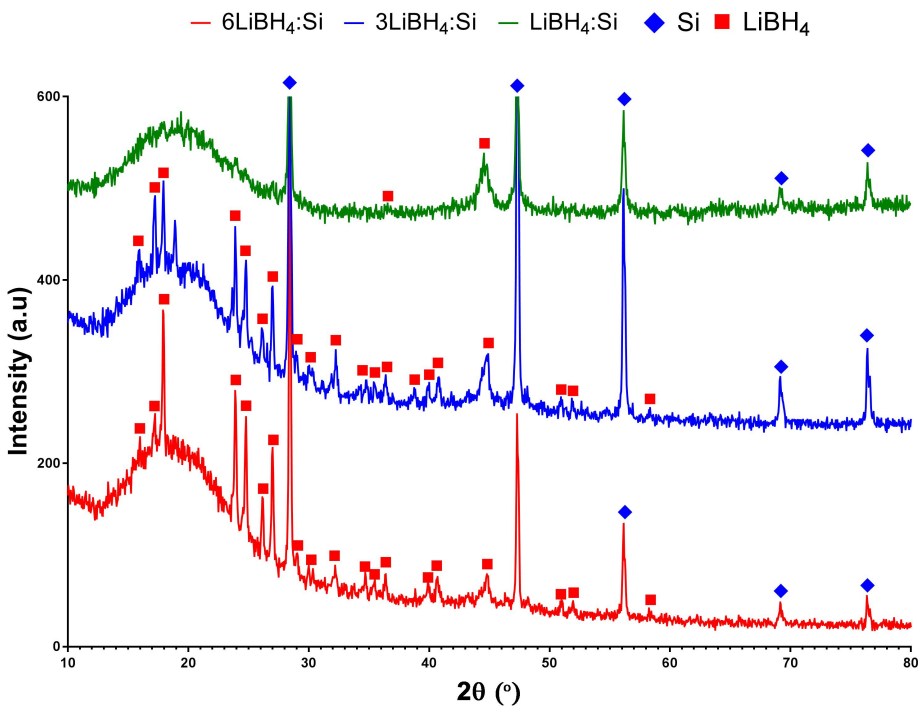

Figure 4.35: XRD data for the four hour ball-milled $6LiBH_4$:Si, $3LiBH_4$:Si and $LiBH_4$:Si systems.

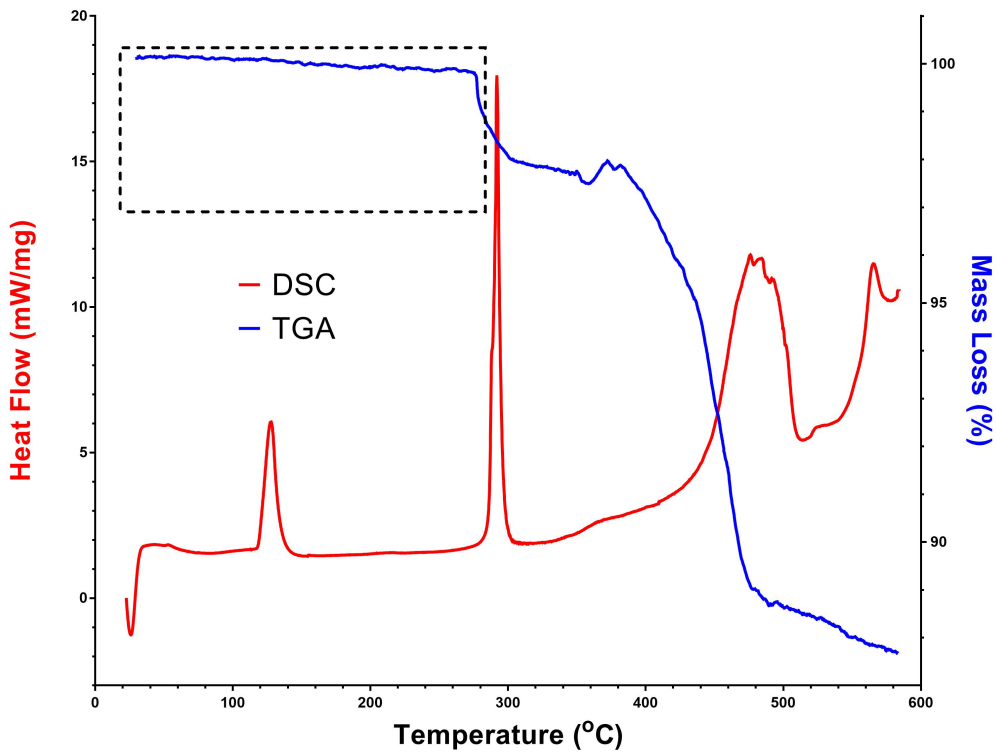

Figure 4.36: DSC and TGA data for the four hour ball-milled $6LiBH_4$:Si system heated to 585°C at 10 °C min^{-1}. Dotted box indicates decomposition occurring within the solid-state.

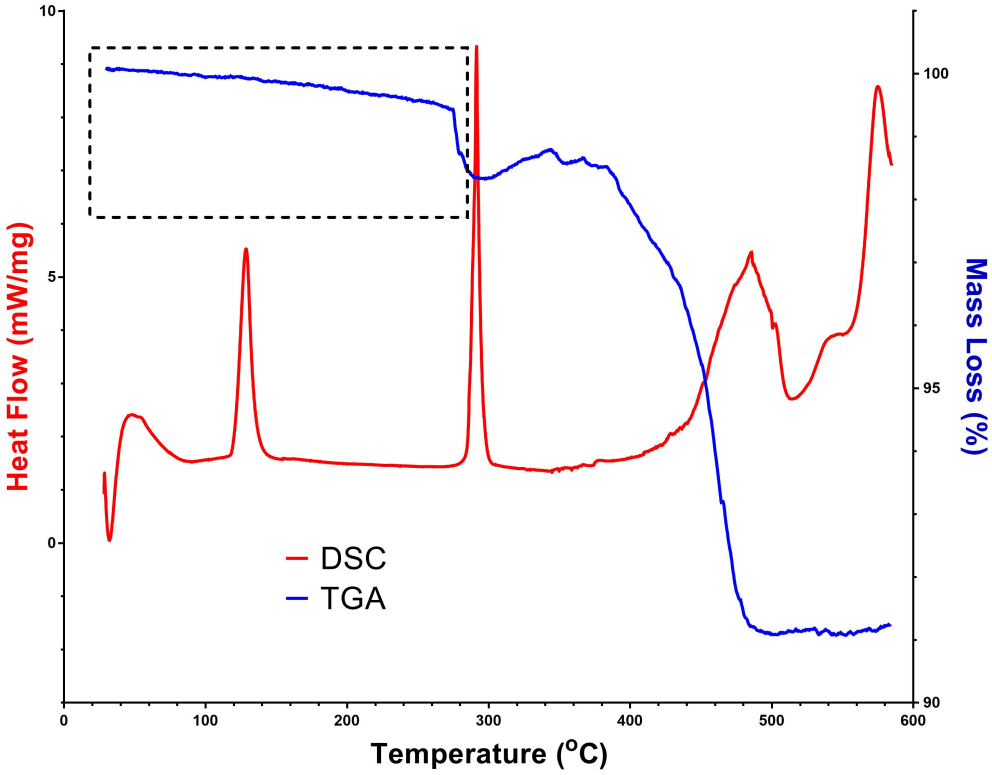

Figure 4.37: DSC and TGA data for the four hour ball-milled $3LiBH_4$:Si system heated to 585°C at 10 °C min^{-1}. Dotted box indicates decomposition occurring within the solid-state.

Figure 4.37 shows the TGA and DSC data for the four hour ball-milled $3LiBH_4$:Si system. The orthorhombic to hexagonal phase transition is observed on the DSC data at 120 °C followed by the melting of the $LiBH_4$ occurring at 295 °C. Upon melting a small mass loss is observed on the TGA after which a small mass gain in seen but can be attributed to foaming of the material. After the small mass loss the main decomposition occurs between 400 and 500 °C as seen on both the TGA and DSC data. A total mass loss for the system was 9 wt% and foaming of the sample did not allow for post-decomposition analysis.

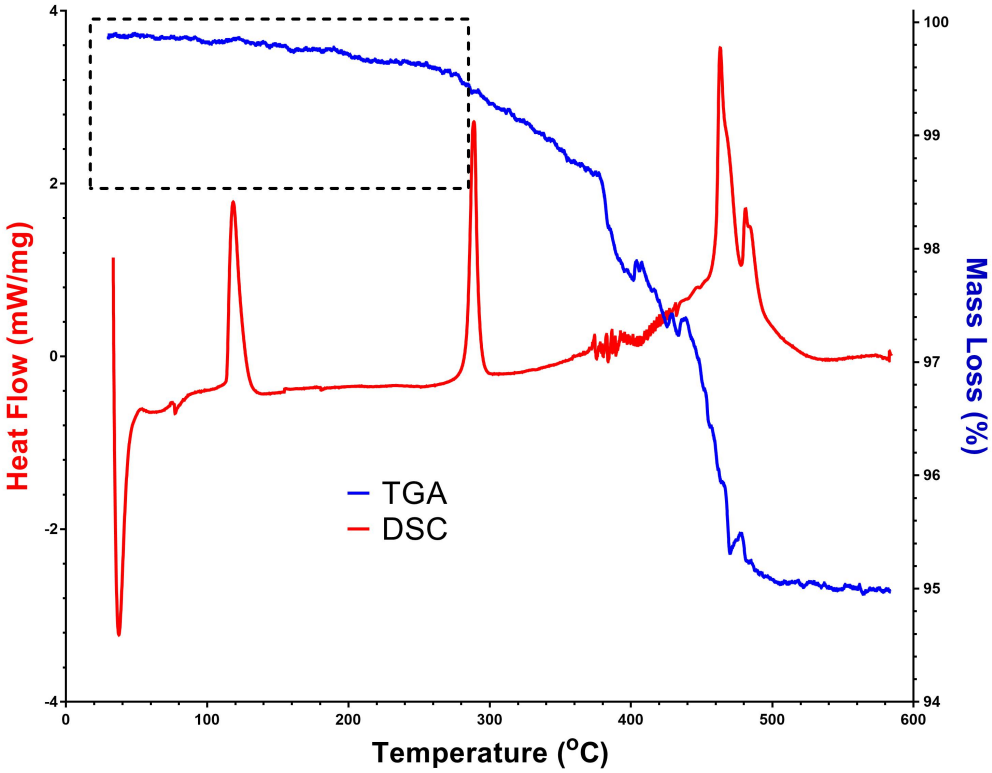

Figure 4.38: DSC and TGA data for the four hour ball-milled $LiBH_4$:Si system heated to 585°C at 10 °C min^{-1}. Dotted box indicates decomposition occurring within the solid-state.

Figure 4.38 shows the TGA and DSC data for the four hour ball-milled $LiBH_4$:Si system. The orthorhombic to hexagonal phase transition is observed on the DSC data at 120 °C followed by the melting of the $LiBH_4$ occurring at 295 °C. Upon melting a small mass loss is observed on the TGA after which the main decomposition occurs between 400 and 500 °C, as seen on both the TGA and DSC data. Whereas the other two systems showed a broad decomposition peak at 480 °C the DSC data here showed two sharper peaks at 480 °C and 500 °C but owing to the foaming of the material no post-decomposition analysis could be performed to determine any new species. A total mass loss for the system was 5 wt%.

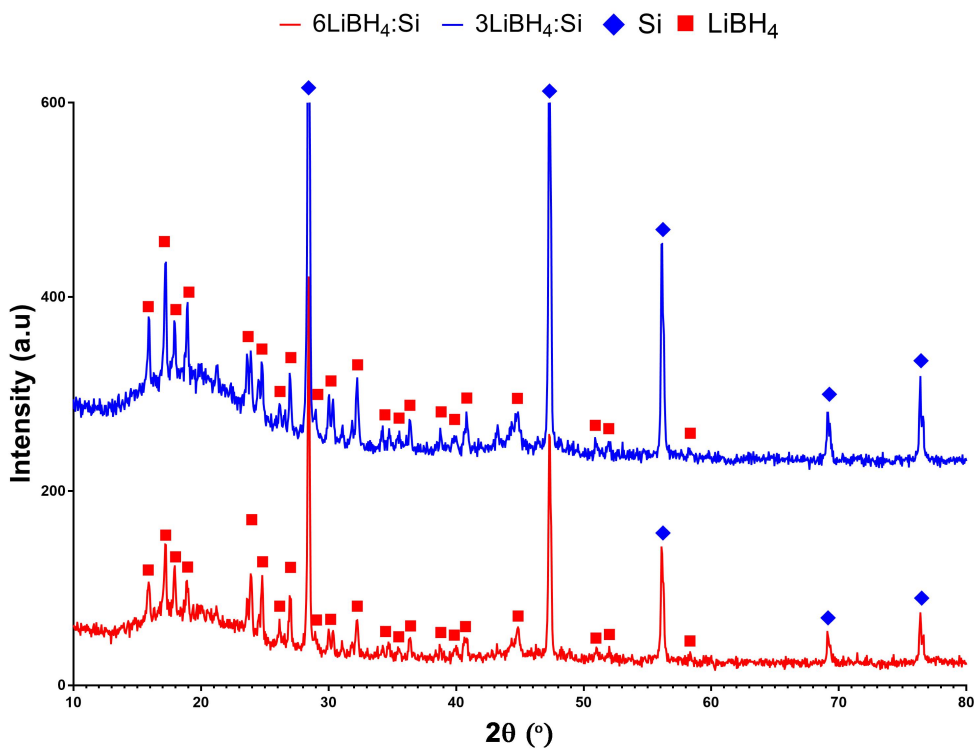

Figure 4.39: XRD data for the five hour total ball-milled $6LiBH_4$:Si and $3LiBH_4$:Si systems.

4.3.3.3 Five Hours Ball-Milling

Figure 4.39 shows the XRD data for the four hour ball-milled with 1 hour soft milled $6LiBH_4$:Si and $3LiBH_4$:Si systems. Peaks indicative of $LiBH_4$ and Si are visible for all three systems with Si peak intensity increasing along with its molar ratio and $LiBH_4$ peak intensities usually decreasing along with its molar ratio in the system.

Figure 4.40 shows the DSC and TGA data for the five hour ball-milled $6LiBH_4$:Si system. Upon heating the orthorhombic to hexagonal phase transition is observed at 120 °C, on the DSC data, followed by the melting of the $LiBH_4$ at 295 °C.

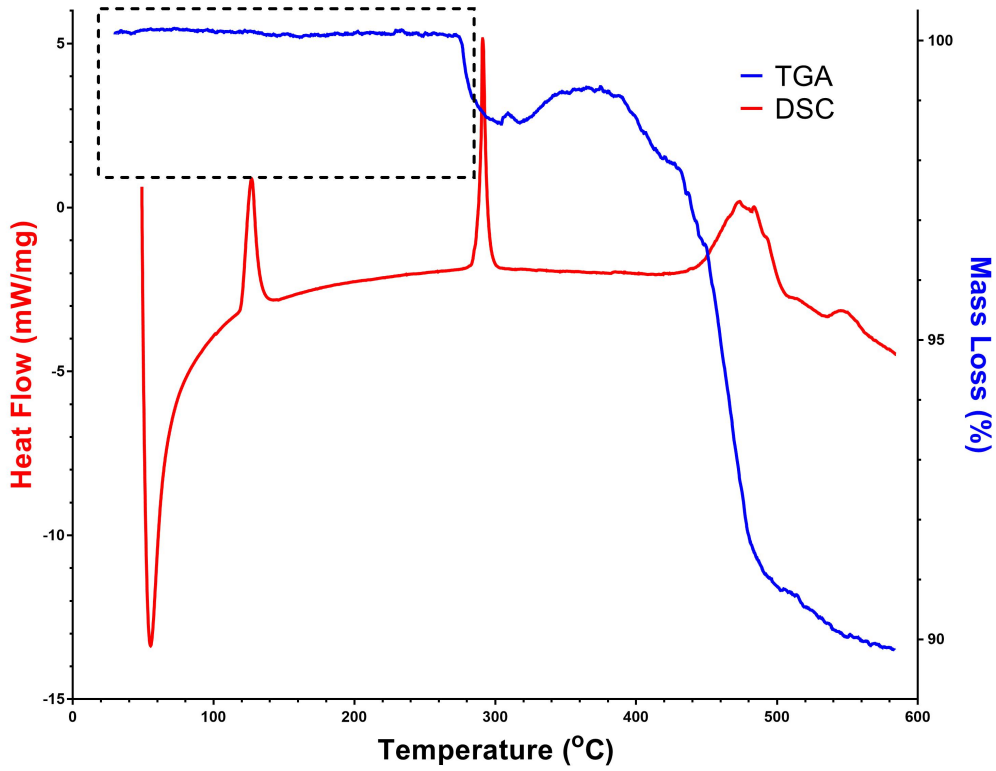

Figure 4.40: DSC and TGA data for the five hour total ball-milled $6LiBH_4$:Si system heated to 585°C at 10 °C min^{-1}. Dotted box indicates decomposition occurring within the solid-state.

Upon melting a small mass loss is observed on the TGA data after which a small mass gain follows owing to the foaming of the material. The primary mass loss occurs between 400 and 500 °C and can be seen on the TGA mass loss and the endotherm on the DSC in the same region. Total mass loss for the system was 10 wt% and post-decomposition analysis was not possible owing to the foaming of the material.

Figure 4.41 shows the DSC and TGA data for the five hour ball-milled $3LiBH_4$:Si system. Upon heating the the orthorhombic to hexagonal phase transition is ob-

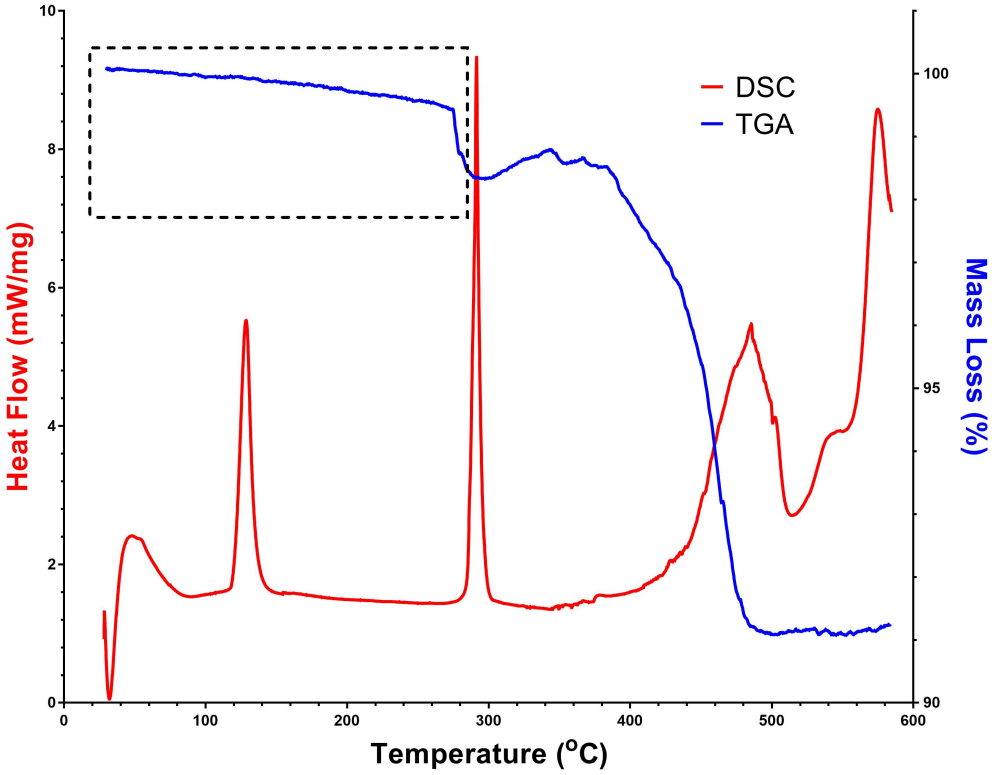

Figure 4.41: DSC and TGA data for the five hour ball-milled $3LiBH_4$:Si system heated to 585°C at 10 °C min^{-1}. Dotted box indicates decomposition occurring within the solid-state.

served at 120 °C, on the DSC data, followed by the melting of the $LiBH_4$ at 295 °C. Upon melting a small mass loss is observed on the TGA data after which a small mass gain follows owing to the foaming of the material. The primary mass loss occurs between 400 and 500 °C and can be seen on the TGA mass loss and the endotherm on the DSC in the same region. Total mass loss for the system was 9 wt% and post-decomposition analysis was not possible owing to the foaming of the material.

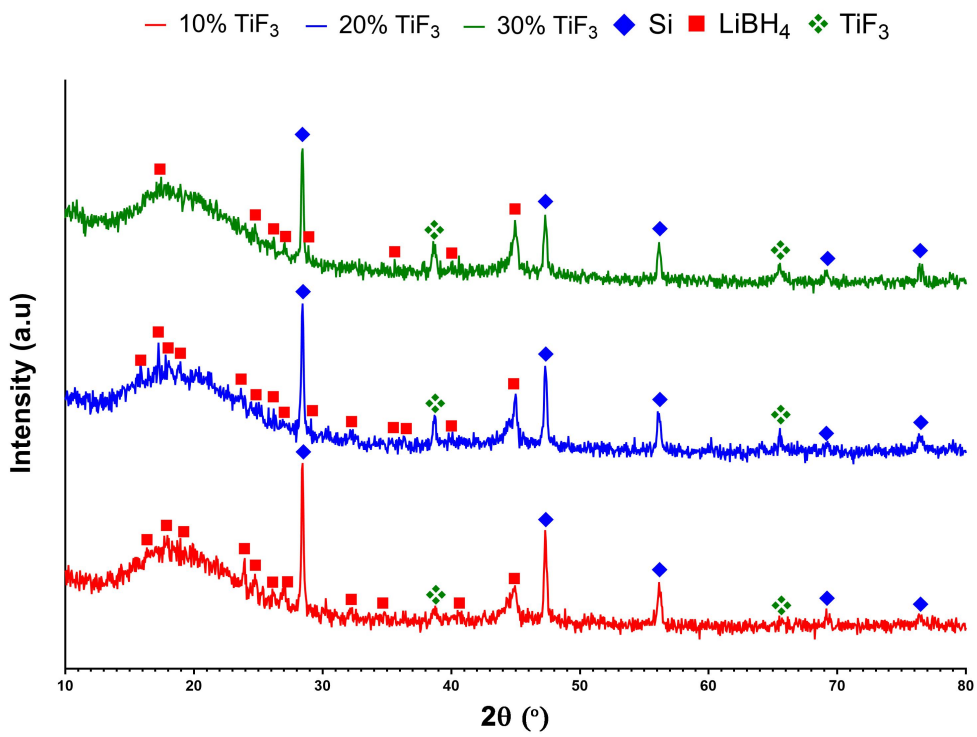

Figure 4.42: XRD data for the five hour ball-milled 4.4$LiBH_4$:Si system with 10, 20 and 30% by mass added TiF_3.

4.3.4 Effect of Titanium Catalyst on $LiBH_4$:xSi System

Figure 4.42 shows the XRD data for the 4.4$LiBH_4$:Si system with added TiF_3 catalyst at 10, 20 and 30% by mass. Peaks shown are indicative of $LiBH_4$ and Si but no peaks are observed for the presence of TiF_3.

Figure 4.43 shows the DSC and TGA data for the 4.4$LiBH_4$:Si system with 10% TiF_3 by mass. While the orthorhombic to hexagonal phase transition is still observed to occur at 120 °C the decomposition of the $LiBH_4$ is shown to begin as low as 100 °C seen on the TGA data. The $LiBH_4$ is seen to slowly decompose up until it melts

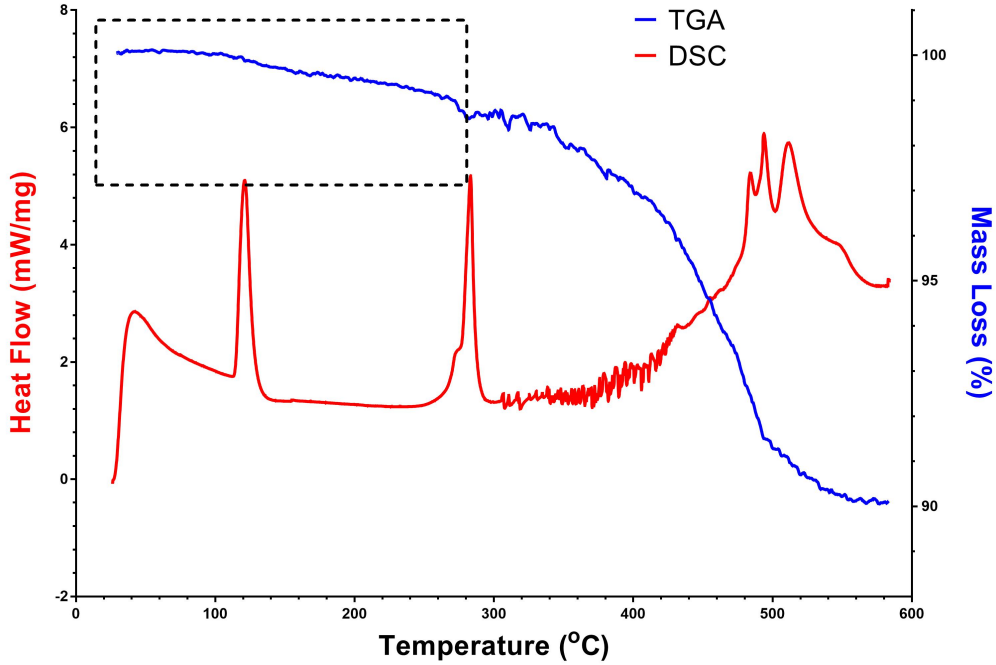

Figure 4.43: DSC and TGA data for the five hour ball-milled 4.4$LiBH_4$:Si system with 10% TiF_3 by mass heated to 585°C at 10 °C min^{-1}. Dotted box indicates decomposition occurring within the solid-state.

as seen on the DSC data at 295 °C. After the melting the $LiBH_4$ is observed to decompose more quickly in the expected region of 400-500 °C. Interestingly, the DSC data for this region does not consist of a single broad peak but instead is composed of several smaller peaks. This suggests that there are other reactions occurring which were not detected for the previous systems. The total mass loss for this system was 10 wt%.

Figure 4.44 shows the DSC and TGA data for the 4.4$LiBH_4$:Si system with 20% TiF_3 by mass. Decomposition of this system is observed to occur at 100 °C followed by the phase transition at 120 °C which was less intense than as-received $LiBH_4$.

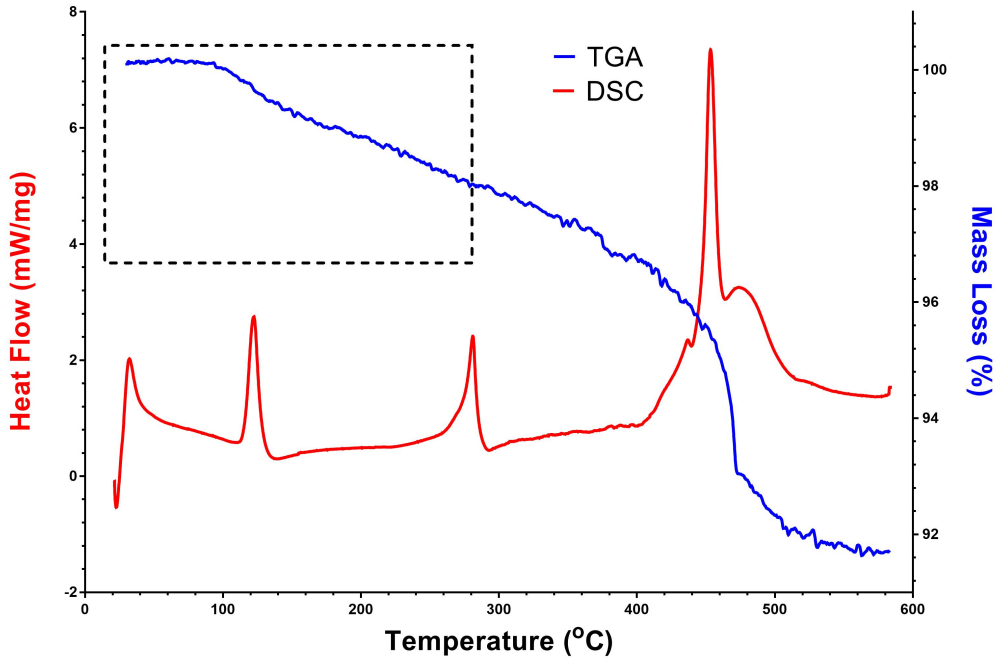

Figure 4.44: DSC and TGA data for the five hour ball-milled $4.4LiBH_4$:Si system with 20% TiF_3 by mass heated to 585°C at 10 °C min^{-1}. Dotted box indicates decomposition occurring within the solid-state.

Decomposition was observed to occur steadily and the melting of the $LiBH_4$ at 290 °C was not shown to affect the decomposition rate. By 440 °C a mass loss of 4 wt% was observed after which a sharp mass loss occurred resulting in a further 4% loss by 500 °C. During the period of sudden mass loss the broad endotherm expected in this region is superimposed by one sharp peak at 450 °C and a possible small peak on the side at 440 °C. Total mass loss for the system was 8.2 wt%.

Figure 4.45 shows the DSC and TGA data for the $4.4LiBH_4$:Si system with 30% TiF_3 by mass. Mass loss for this system is observed to occur as low as 40 °C for this system. The phase transition for the $LiBH_4$ still occurs at 120 °C but is weak

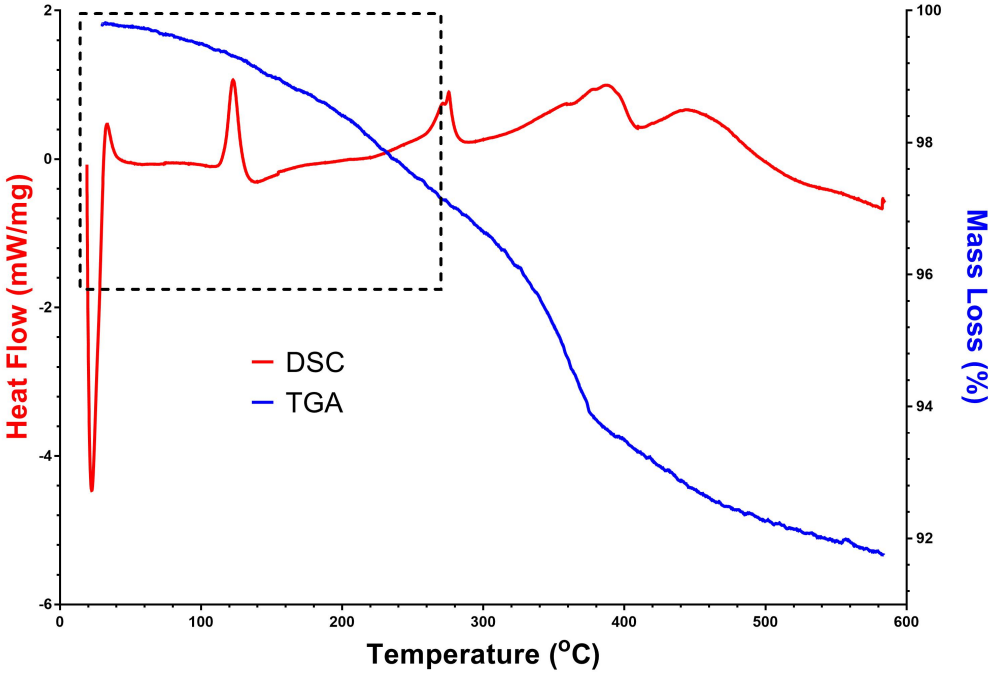

Figure 4.45: DSC and TGA data for the five hour ball-milled 4.4$LiBH_4$:Si system with 30% TiF_3 by mass heated to 585°C at 10 °C min^{-1}. Dotted box indicates decomposition occurring within the solid-state.

compared to previous systems. A broad endotherm on the DSC that lasts until the end of the reaction begins to occur at 140 °C. The weak endotherm at 290 °C relates to the melting of of the $LiBH_4$ and is followed by two broad endotherms at 380 °C and 450 °. A rapid increase in the mass loss occurs between 320 and 380 °C which steadily declines until the end of the reaction. Total mass for the system was observed to be 8.2 wt%.

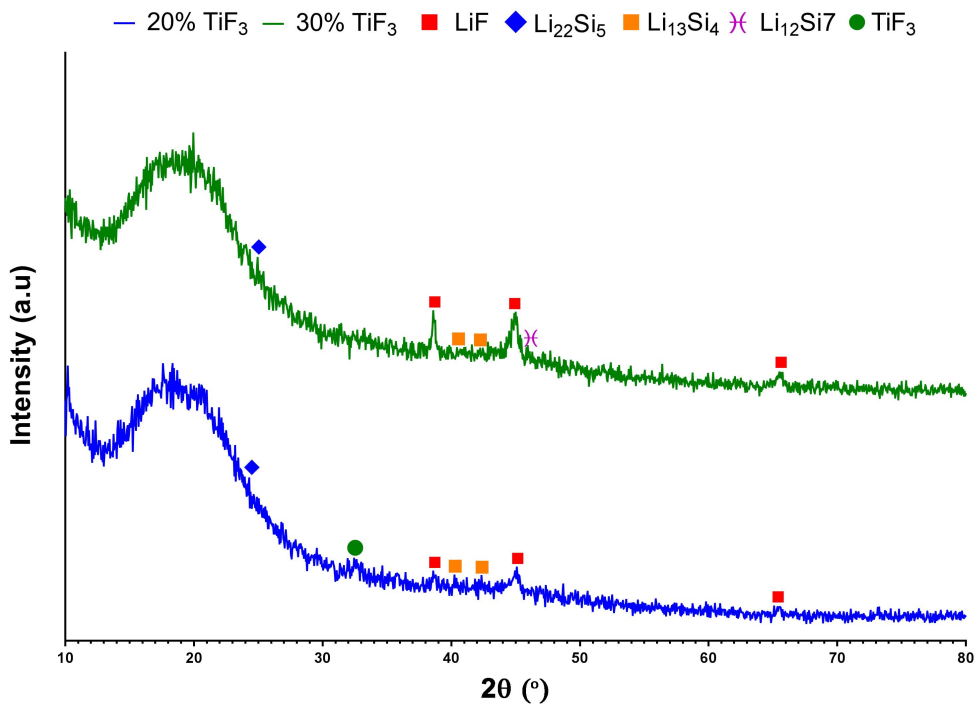

Figure 4.46: XRD data for the five hour ball-milled 4.4$LiBH_4$:Si system with 20 and 30% by mass added TiF_3 after heating to 585 °C.

Owing to the lack of foaming for the 4.4$LiBH_4$:Si (20 wt% TiF_3) and 4.4$LiBH_4$:Si (30 wt% TiF_3) systems post decomposition analysis was possible. Figure 4.46 shows the XRD for the recovered samples and the primary species observed for both samples was lithium fluoride (LiF). Other species observed included three different lithium silicides including the desired $Li_{22}Si_5$, $Li_{13}Si_4$, $Li_{12}Si_7$ but all of these peaks were extremely weak compared to the LiF. Some remaining TiF_3 was also observed in the 20 wt% sample.

4.4 Lithium Borohydride and Iron/Cobalt Systems

4.4.1 Introduction

This work investigated the addition of both Fe and Co to $LiBH_4$ to replicate the reaction seen when using nickel. Ratios of 1:2 and 1:1 ($LiBH_4$ to Co or Fe) will be used to match the most successful ratio used with nickel (1:2) and to determine if a more metal lean system is viable.

4.4.2 As-received Materials

Figure 4.47 shows the XRD data for as-received cobalt and iron. The iron data shows two distinct peaks at 44.7 and 65 °. The cobalt data shows two less intense peaks at 44.6 and 47.3 °. Both metals fluoresce during XRD spectroscopy and demonstrate a distinct background signal arising from just after the hump from the amorphous tape at 30 ° to 80 °.

4.4.3 Use of Iron

Figure 4.48 shows the XRD data for the as-milled $LiBH_4$:2Fe and $LiBH_4$:Fe systems. Peaks indicating the presence of iron are clearly observed on both sets of data at 44.6

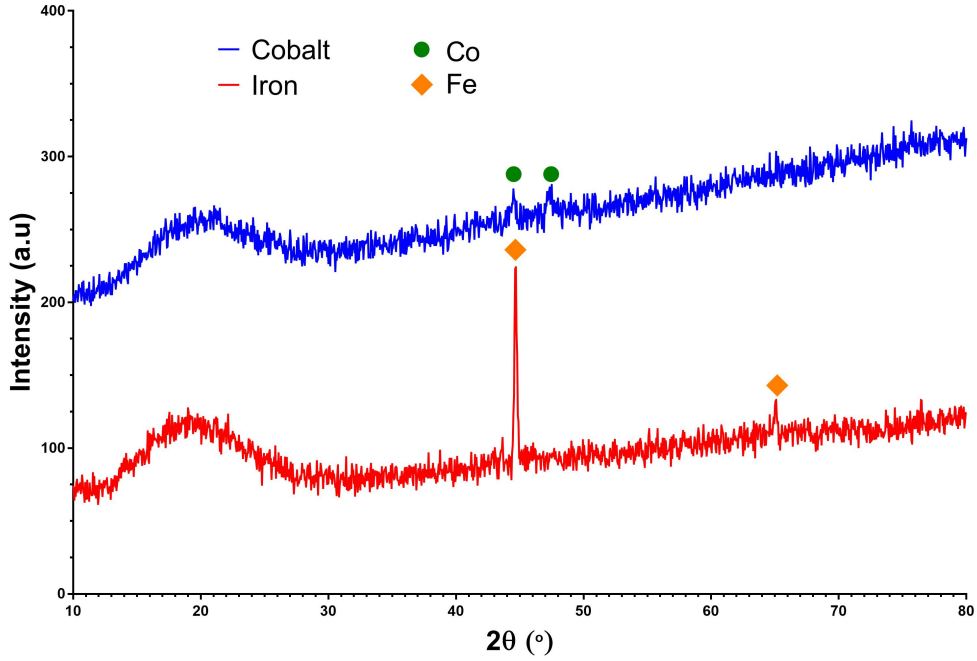

Figure 4.47: XRD data for as-received cobalt and iron.

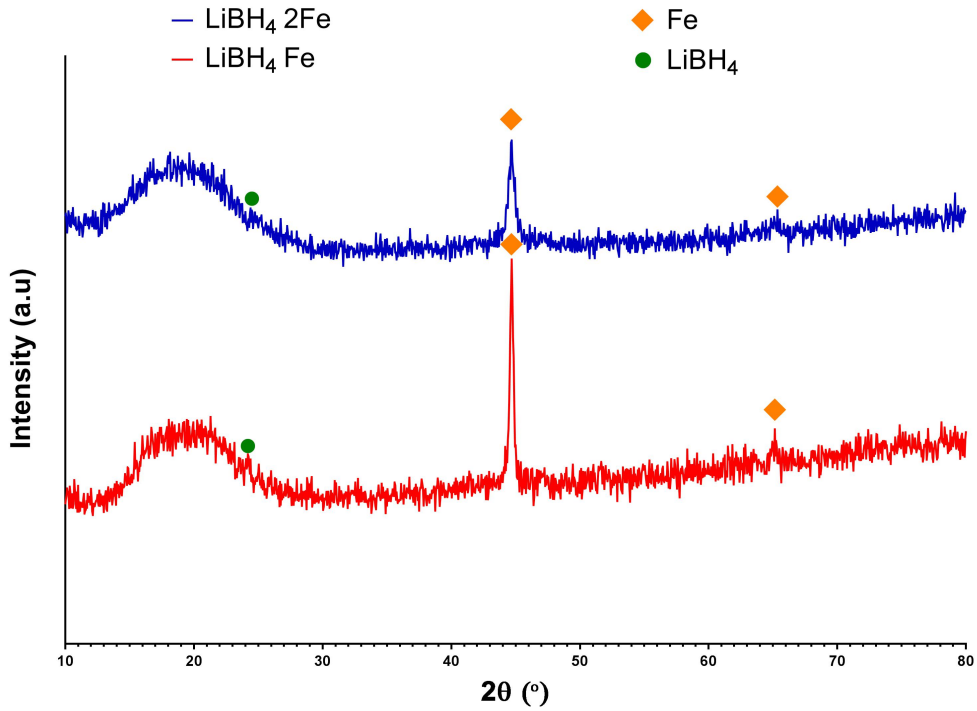

Figure 4.48: XRD data for as-milled $LiBH_4$:2Fe and $LiBH_4$:Fe systems milled for 3 hours.

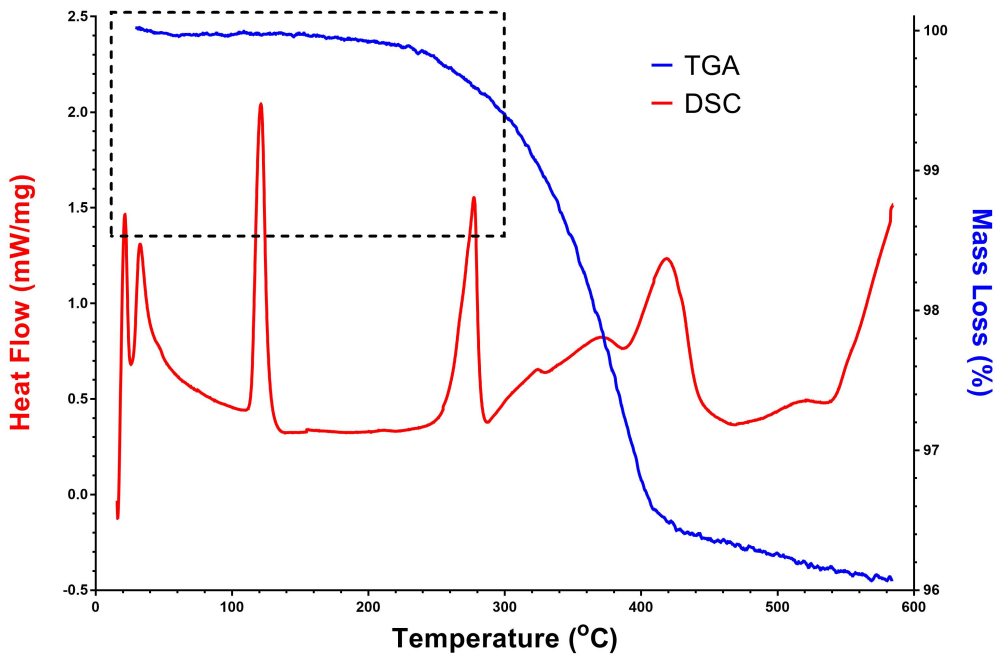

Figure 4.49: DSC and TGA data for the $LiBH_4$:Fe system heated to 585°C at 10 °C min^{-1}. Dotted box indicates all decomposition occurring below 300°C.

and 65.4 °. One weak $LiBH_4$ peak is observed on both of the data at 24.2 °C owing to the poor X-ray scattering of the $LiBH_4$ diluted by the iron component.

Figure 4.49 shows the DSC and TGA data for the $LiBH_4$:Fe system. The phase transition of the $LiBH_4$ can be seen to occur at 120 °C followed by the onset decomposition at 230 °C observed on the TGA data. Melting of the $LiBH_4$ is observed to occur at 270 °C indicated by the broad endotherm which is followed by a combination of three endotherms into one broad one between 285 and 470 °C corresponding with the primary decomposition occurring on the TGA data which is seen to slow from 425 °C onwards. Total mass loss for the system was observed to be 3.9 wt%.

Figure 4.50 shows the DSC and TGA data for the $LiBH_4$:2Fe system. The phase

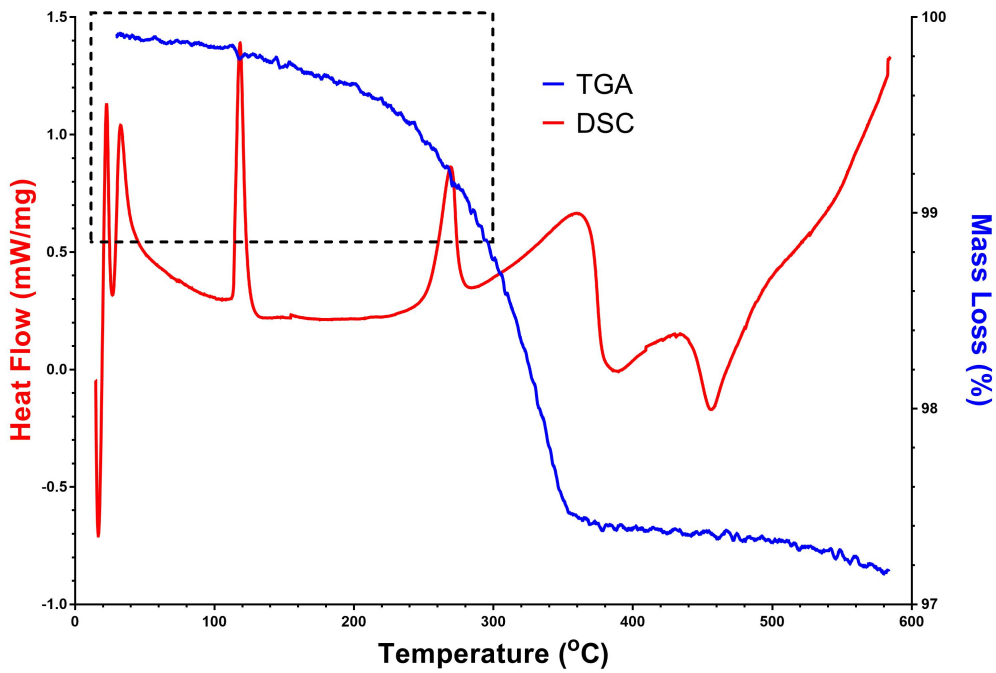

Figure 4.50: DSC and TGA data for the $LiBH_4$:2Fe system heated to 585°C at 10 °C min^{-1}. Dotted box indicates all decomposition occurring below 300°C.

transition for the $LiBH_4$ is observed to occur at 120 °C which coincides with the increased rate of decomposition. Melting of the $LiBH_4$ is seen to occur at 270 °C but is superimposed over the top of a broad endotherm observed to begin at 220 °C and finish by 390 °C. The fastest decomposition rate occurs between 220 and 370 °C after which mass is only lost slowly. Total mass loss for the system is observed to be 2.8 wt%.

Figure 4.51 shows the XRD for the $LiBH_4$:2Fe and $LiBH_4$:Fe systems upon decomposition up to 585 °C. For the $LiBH_4$:Fe system a mix of three different iron borides are observed (FeB, Fe_2B and Fe_3B) but the stoichiometrically expected species, FeB, is not the primary species formed. For the $LiBH_4$:2Fe a mix of the three iron

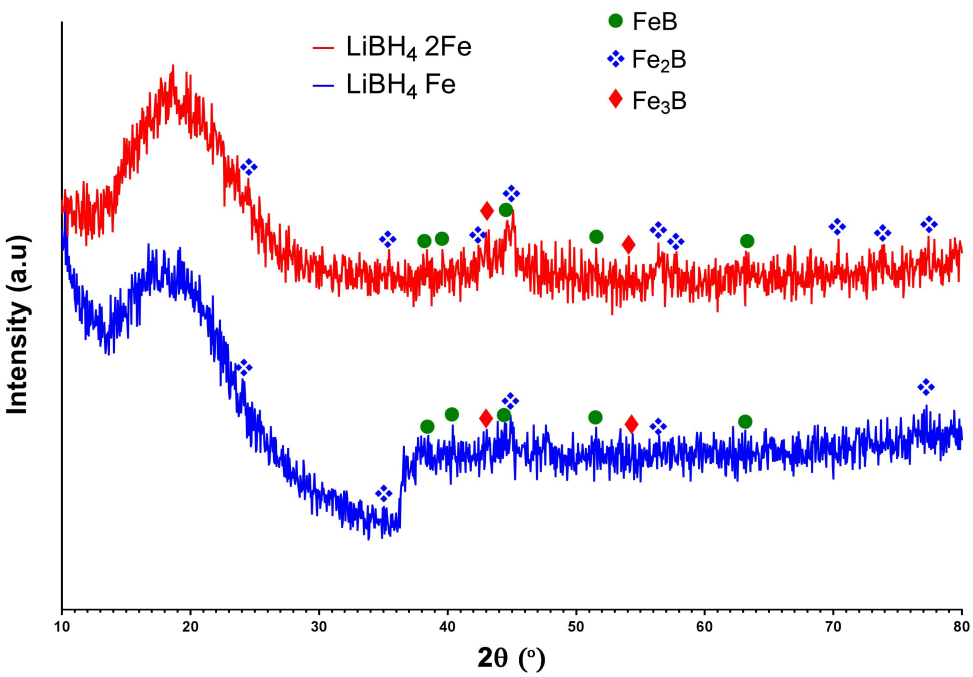

Figure 4.51: XRD data for the $LiBH_4$:2Fe and $LiBH_4$:Fe systems decomposed up to 585 °C.

borides is still observed but the Fe_2B is seen to be dominant species.

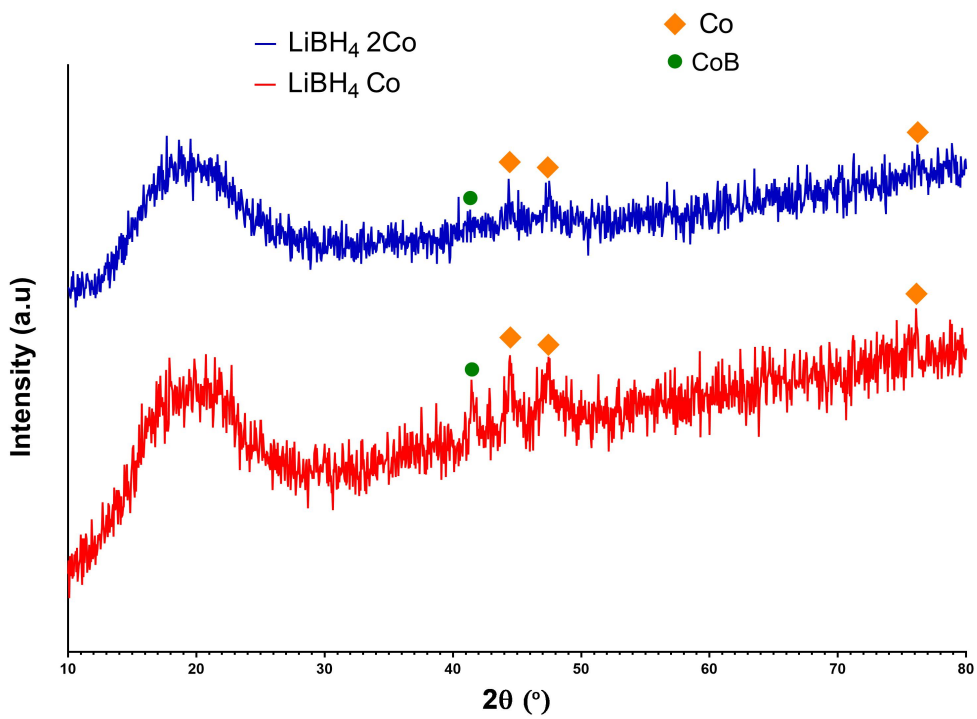

Figure 4.52: XRD data for as-milled $LiBH_4$:2Co and $LiBH_4$:Co systems milled for 3 hours.

4.4.4 Use of Cobalt

Figure 4.52 shows the XRD data for the $LiBH_4$:Co and $LiBH_4$:2Co systems post-milling. Peaks relating to Co are clearly seen on both data at 44.5, 51.2 and 76.2 °. Also present on the data are the formation of CoB and Co_3B cobalt borides implying some decomposition of the $LiBH_4$ has occurred during the milling process.

Figure 4.53 shows the DSC and TGA data for the $LiBH_4$:Co system. Upon heating mass loss is observed to occur almost immediately at 40 °C followed by the $LiBH_4$ phase transition at 120 °C. The rate of mass loss increases slightly after the phase transition and increases further still after the melting of the $LiBH_4$ is observed to occur at 275 °C. After the melting a broad endotherm is observed from 320 to

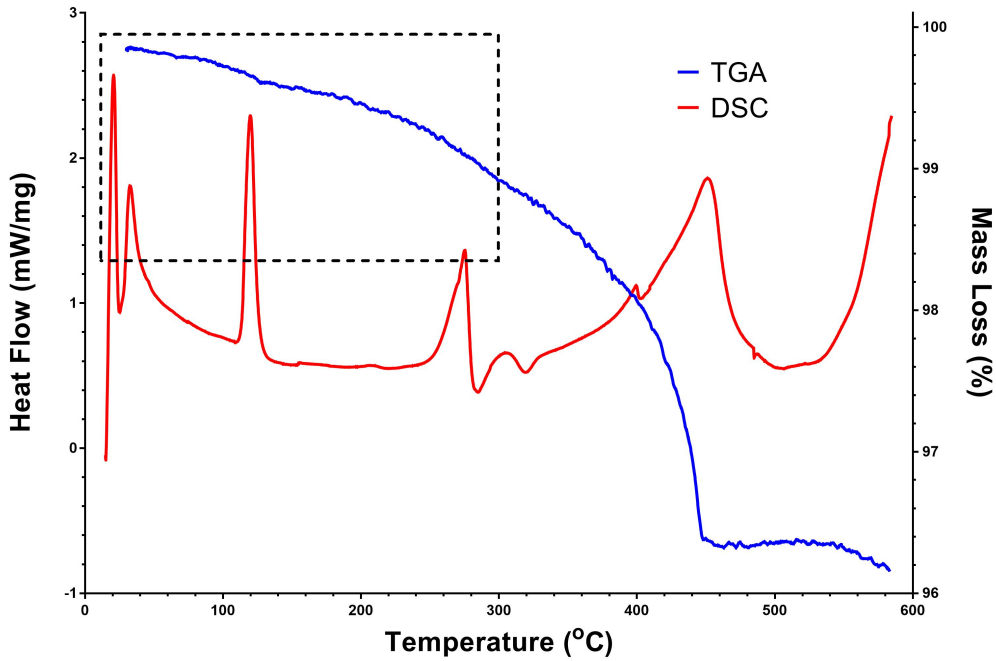

Figure 4.53: DSC and TGA data for the $LiBH_4$:Co system heated to 585°C at 10 °C min^{-1}.

Dotted box indicates all decomposition occurring below 300°C.

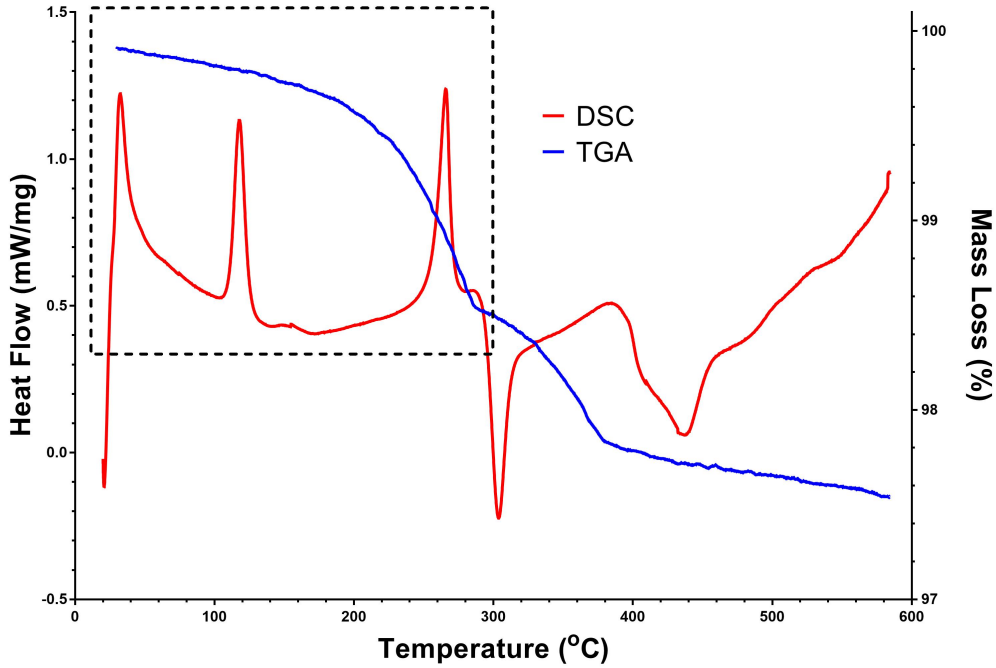

Figure 4.54: DSC and TGA data for the $LiBH_4$:2Co system heated to 585°C at 10 °C min^{-1}. Dotted box indicates all decomposition occurring below 300°C.

500 °C, corresponding to the primary mass loss observed on the TGA data. Total mass loss for the system was seen to be 3.8 wt%.

Figure 4.54 shows the DSC and TGA data for the $LiBH_4$:2Co system. Mass loss is observed to begin almost immediately at 40 °C followed by the phase transition of the $LiBH_4$ at 120 °C. Rate of mass loss increases at 190 °C until 290 °C after which another slower but significant mass loss occurs between 290 and 380 °C. During the first mass loss the endotherm at 265 °C indicates the melting of the $LiBH_4$ while during the second mass loss an exotherm is observed at 300 °C. Following this exotherm, a broad endotherm is seen at 395 °C. Total mass loss for the system was observed to be 2.4 wt%.

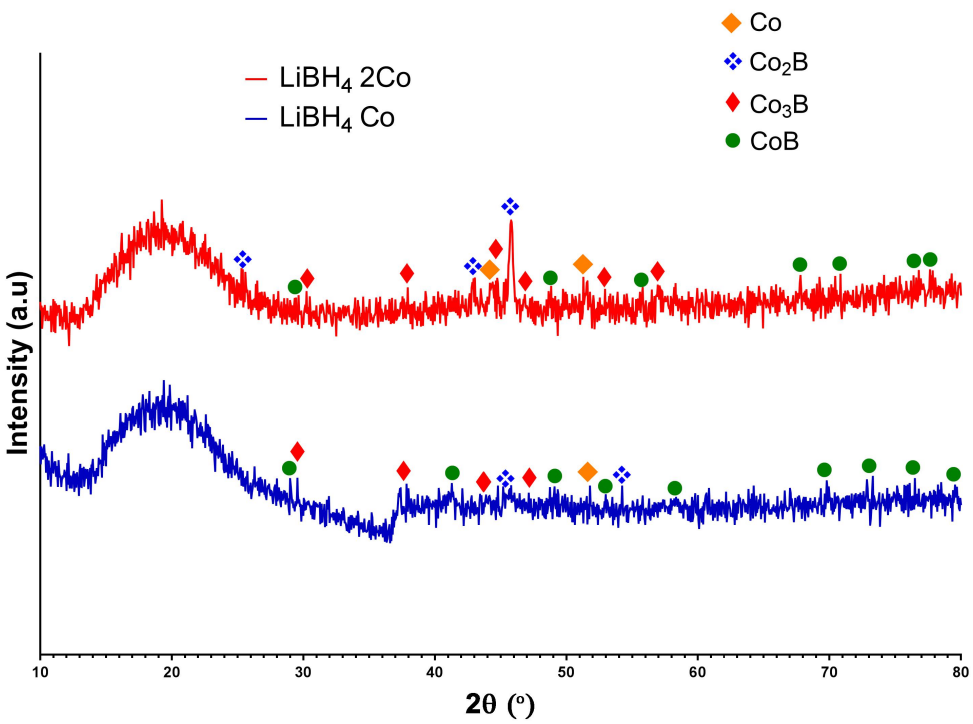

Figure 4.55: XRD data for the decomposed, up to 585 °C, $LiBH_4$:2Co and $LiBH_4$:Co systems.

Figure 4.55 shows the XRD data for the decomposed $LiBH_4$:2Co and $LiBH_4$:Co systems. The $LiBH_4$:Co system shows a mix of three different cobalt borides: CoB, Co_2B and Co_3B. CoB is observed to be the most distinct of the three borides formed and conforms with the stoichiometry of the system. The $LiBH_4$:2Co system also shows a mix of the three borides but this time the Co_2B is the most prominent species observed as predicted by the stoichiometry.

Chapter 5

Discussion

5.1 Lithium Borohydride and Nickel Systems

5.1.1 Introduction

Section 4.2 of this work dealt with the addition of nickel to improve the thermodynamics of $LiBH_4$ decomposition. The rational behind this was the previous use of $CaNi_5$ to decompose $LiBH_4$, presented here and by Meggough *et al.* [55], which formed nickel borides as an end product after completing its decomposition by 200 °C. When looking at the phase diagram for boron-nickel system [149], figure 5.1, it can be seen that several different nickel borides can be formed including NiB, Ni_4B_3, Ni_2B and Ni_3B. When considering the $2LiBH_4$:$CaNi_5$ system the ratio between boron and nickel is 1:2.5, which correlates to the stoichiometric end products

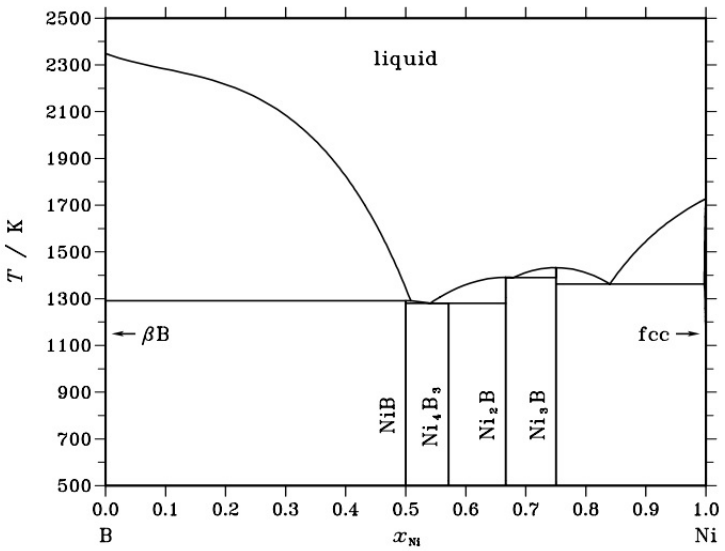

Figure 5.1: Phase diagram for the boron-nickel system. [149].

which were a mix of Ni_2B and Ni_3B. For this work the ratios of boron to nickel were chosen to match the $CaNi_5$ ratio, study a more nickel rich system and two more nickel lean systems to see if Ni_3B, Ni_2B and NiB could be formed via thermodynamic reactions.

The use of nickel has also been studied by Xia *et al.* where the $2LiBH_4$:Ni system showed some reversibility with 3.3 wt% taken up at 600 °C and 100 bar [43] but, unlike the results presented here, this reaction did not take place in the solid state with temperatures exceeding 300 °C. Studies by Negene *et al.* and Xu *et al.* both used a combination of confinement and dopant levels of nickel in their studies and found that low pressures could be used (40 and 30 bar respectively) but high temperatures were also required (320 and 400 °C respectively) [107,108,110]. The Xu *et al.* system showing the most promising uptake results with 9.8 wt% maintained over

30 cycles compared to 2.3 wt% for the Negene *et al.* system. To improve upon these systems any decomposition or reversibility occurring below 300 °C will be important while trying to match the 3.3 wt% able to be reversed in the Xia *et al.* paper.

5.1.2 Varying Nickel Content

XRD data for the four nickel systems is presented in figure 4.8 and primarily showed diffraction lines of nickel. $LiBH_4$ peaks were difficult to observe in all but the 1:1 ratio system owing to it being masked by the large quantity of nickel in the systems and it being a poor X-ray scatterer. One potential technique that could have better distinguished the crystal structure of the $LiBH_4$, from the background, would be Raman spectroscopy. Raman spectroscopy has been shown to be effective in the study in the phase change of $LiBH_4$ and would confirm its presence both pre and post-milling [150]. Nickel peaks were demonstrated to broaden as nickel content increased along with greater levels of Ni_3B formed during the milling process.

Decomposition for the four systems are presented in figures 4.9 & 4.10 and summarised in figure 5.2. All four systems showed an overall reduction in their decomposition temperatures, as seen on the TGA data, with the 2, 2.5 and 3Ni systems in particular showing a large decrease over the as-received $LiBH_4$. The $LiBH_4$:Ni system showed a two stage decomposition at 200-400 and 500-600 °C whereas the other three systems demonstrated a one step decomposition beginning at 140 °C and finishing between 260 and 300 °C. Storage capacities of the 2.5 and 3Ni sys-

tems did not improve over that of the $2LiBH_4$:$CaNi_5$ but the 2Ni system was able to decompose up to 2.3 wt% by 585 °C, an increase of 1 wt%. While the storage capacity of the $LiBH_4$:Ni system was much higher than that of the other three systems by 585 °C, by 300 °C it has a lower capacity than those of the others if the reaction is to be carried out in the solid state. While the expected phase transition of the $LiBH_4$ occurs at 120 °C for all four systems, unlike the $CaNi_5$ system, the intensity of the peak reduces as the nickel content increases. The melting of the $LiBH_4$ is still observed for all four systems but appears to occur at a lower temperature and become less intense with increasing nickel content which implies that it has thermodynamically altered the $LiBH_4$ melting temperature. In contrast, for the $2LiBH_4$:$CaNi_5$ system no melting of the $LiBH_4$ is observed at all suggesting that the addition of calcium is able to suppress the melting or the decomposition is so rapid that there is no $LiBH_4$ remaining to melt. For the three most nickel rich systems this melting peak is observed to be superimposed over that of a broad endotherm which is attributed to the decomposition for these systems below 300 °C. For the $LiBH_4$:Ni system a broad decomposition peak between 320 and 420 °C corresponds with the large mass loss observed on the TGA confirming its higher decomposition temperature than the other three systems. Both the 2Ni and 2.5Ni systems show an exotherm at 460 °C which is attributed to the formation of Ni_2B, seen in the XRD data. The decomposition temperature of the three nickel rich systems compares favourably to those reported in the literature. Xia *et al.* reported decomposition of $LiBH_4$ occurring only above 300 °C when a 2:1 ratio ($LiBH_4$:Ni) was used. For

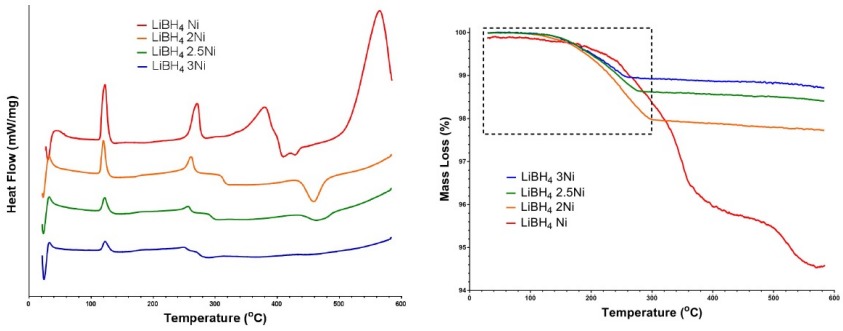

Figure 5.2: DSC and TGA data for the four nickel systems studied.

a $LiBH_4$:0.25Ni system, Li *et al.* reported that significant decomposition did not occur below 330 °C [43, 109].

Analysis of species formed during the decompositions were performed using XRD and are presented in figures 4.11, 4.12, 4.13, 4.14 and summarised in figure 5.3. For the $LiBH_4$:Ni system no significant products were formed by 300 °C, the temperature at which the other three systems had experienced their primary decomposition, but showed a reduction in the intensity of the nickel peaks indicating that some reaction had occurred between the two components. By 585 °C new products had been formed. Nickel was no longer observable but instead a mix of several nickel borides was seen. The stoichiometrically expected NiB was formed during the reaction but alongside this Ni_2B, Ni_3B and Ni_4B_3 were also identified. The formation of Ni_4B_3 with low stoichiometries of nickel correlates well with the reported literature as it was observed by Li *et al.*, Xu *et al.* and Negene *et al.* [107–110]. For the other three nickel systems by 300 °C, unlike the $LiBH_4$:Ni system, several new species are observed. Nickel peaks were still present but significantly reduced in intensity even

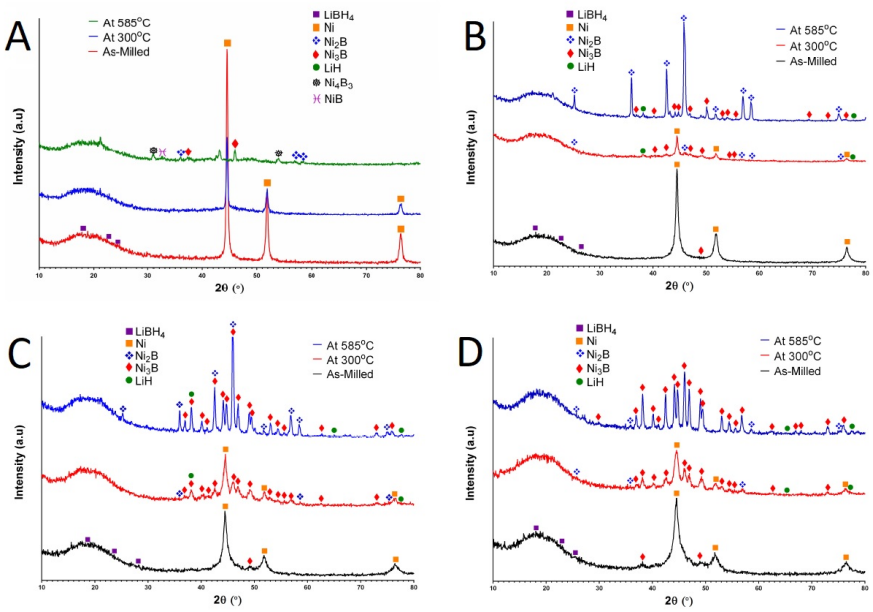

Figure 5.3: XRD data for the four nickel systems studied. A - $LiBH_4$:Ni B - $LiBH_4$:2Ni C - $LiBH_4$:2.5Ni C - $LiBH_4$:3Ni

though the majority of the decomposition for these three systems is complete by this temperature. For all three systems the formation of Ni_3B is found to be the most prevalent species formed by 300 °C with trace amounts of Ni_2B also found. By 585 °C the three systems showed a different picture depending on their stoichiometry. For the 3Ni system the primary species observed is Ni_3B which conforms with the stoichiometry of the system. Weak LiH and Ni_2B peaks are also seen for this system but this can be attributed to the weak scattering of LiH, similarly to $LiBH_4$, and a side reaction forming the Ni_2B species. For the 2Ni system Ni_2B is now the primary species, conforming to the stoichiometry, with traces of Ni_3B still present. The presence of Ni_2B peaks, instead of Ni_3B observed at 300 °C, confirms the peak at 460°C on the DSC as the rearrangement of the borides as the temperature increases.

For the 2.5Ni system a mix of Ni_2B and Ni_3B peaks are observed and explains the much broader, weaker peak at 460 °C on the DSC as not all of the Ni_3B has reacted to form Ni_2B. From these results it appears that the formation of Ni_3B is the preferred phase at low temperatures, regardless of stoichiometry, with Ni_2B forming at much higher temperatures. This is in agreement with Teppa *et al.* who found that the Gibbs energy of formation of Ni_2B was more favourable at high temperatures compared to Ni_3B [151]. For the $CaNi_5$ system this preference for Ni_3B occurs as well with Ni_3B peaks occurring from 325 °C, observed from the PND data, with the Ni_2B peaks not forming until after 460 °C [55].

The $LiBH_4$:2Ni system was chosen for further studies over the other nickel systems owing to a superior gravimetric weight capacity, 2.3 wt%, compared to the $2LiBH_4$:$CaNi_5$, $LiBH_4$:3Ni and $LiBH_4$:2.5Ni systems. The $LiBH_4$:Ni system was also discounted owing to it showing a an inferior level of decomposition when the temperature was kept below 300 °C.

5.1.3 Focus on the $LiBH_4$:2Ni System

Once it was decided to focus on the $LiBH_4$:2Ni system, owing to its superior weight capacity at low temperatures, it was necessary to confirm that the reaction between the nickel and $LiBH_4$ was a thermodynamic reaction, and not a kinetic improvement, the decomposition was performed under a H_2 back pressure for both TGA and DSC experiments. Figure 4.16 presented this data and it was observed that no significant

change in the decomposition temperature or mass loss was observed on the TGA data while the peaks on the DSC were all present in the same regions as seen under argon. The lack of change under the two different gasses does indicate that this is a thermodynamic reaction as expected as a kinetics limited reaction would show an increased decomposition temperature because the hydrogen back pressure would increase the amount of energy required to increase the pressure further. For this reason a reaction was postulated, equation 5.1, to show the thermodynamic tuning mechanism where the boron has reacted with the nickel to form Ni_2B, releasing the three quarters of the stored hydrogen, while the remaining lithium has formed lithium hydride.

$$LiBH_4 + 2Ni \rightarrow LiH + Ni_2B + \frac{3}{2}H_2 \tag{5.1}$$

To determine if microstructure would have an affect on the decomposition properties of the system two different kinds of nickel were investigated. Previous experiments, up until this point, had been conducted using a micro-scale nickel powder precursor, <150 μm, which was then compared against nano-scale nickel powder, <100 nm. The aim of this experiment was to see if a reduced particle size could improve reaction kinetics as the smaller grain size increases the overall surface area which allows for an increased reaction rate. Figures 4.17 and 4.24 presented the SEM and DSC data for this comparison and from the SEM data it can be seen that after three hours of milling no significant difference in particle size was observed with both

systems showing primarily small particles smaller than 50 μm with the occasional larger particle larger than 50 μm. From the DSC data it was observed that the use of the nano-nickel does not impact significantly the temperature that expected events occur with the only noticeable change being the rearrangement peak for Ni_3B to Ni_2B, occurring at 460 °C, being broader and less intense. The SEM data indicates that while the particle size for the micro-nickel precursor is reduced, compared to the manufacturers specification, some agglomeration of the nano-nickel has occurred as the particle size is bigger than manufacturers specification at 50 μm. With the price of nano-nickel being almost six times that of micro-nickel (32.90 for 5g nano-nickel vs 25.40 for 25 g of micro-nickel) and it providing no advantage over the micro-nickel it was decided to continue using the micro-nickel precursor for future experiments.

To determine how the nickel and boron reacted a scanning electron microscopy/energy-dispersive X-ray spectroscopy (SEM/EDX) study was conducted and the results were presented in figures 4.19 and 4.20. For the as-milled system when observing one of the large particles present, after milling, under back-scattered electron detector there is a significant contrast between light (presence of heavy elements) and dark areas (presence of light elements). It can be assumed that any light areas can be attributed to the nickel in the system and the darker areas attributed to the $LiBH_4$. When performing an EDX analysis of one of the lighter areas it can be seen that the nickel peak (green arrow) on the spectrum is intense while the boron peak

(red arrow) is weak when compared to the carbon peak next to it. An analysis on a darker area saw a reduction in the nickel peak intensity and an increase in the boron peak intensity compared to the carbon peak. From this it can be postulated that during the milling process that the $LiBH_4$, being the lesser component by mass (1:4 ratio), has been spread onto the surface the nickel particles which is why the particle surface on the SEM image appears to be primarily dark with small areas where the $LiBH_4$ has not covered the nickel. An analysis of the system after heating to 585 °C was also performed. Unlike the as-milled system the overall appearance of the particle shows an increased presence of lighter areas. When EDX was used to analyse lighter and darker areas, as with the as-milled system, no noticeable change was observed for the boron peak intensity, compared to the carbon peak, and would now suggest that the boron has reacted with the nickel to form nickel borides.

Powder neutron diffraction (PND) was used to further probe the decomposition reaction *in situ* and is presented in figure 4.21 and A in figure 5.4. From the overall waterfall plot it was difficult to determine products formed so a superplot, figure 4.22 and B in figure 5.4, was constructed to demonstrate the products at different stages during the decomposition. At room temperature the expected $LiBD_4$ and nickel peaks were observed and upon heating to 158 °C the phase transition between orthorhombic and hexagonal had occurred. By 259 °C the $LiBD_4$ was no longer observed and had been replaced by an LiH peak but at this temperature no boron containing species were observed. By 300 °C nickel boride had begun to form.

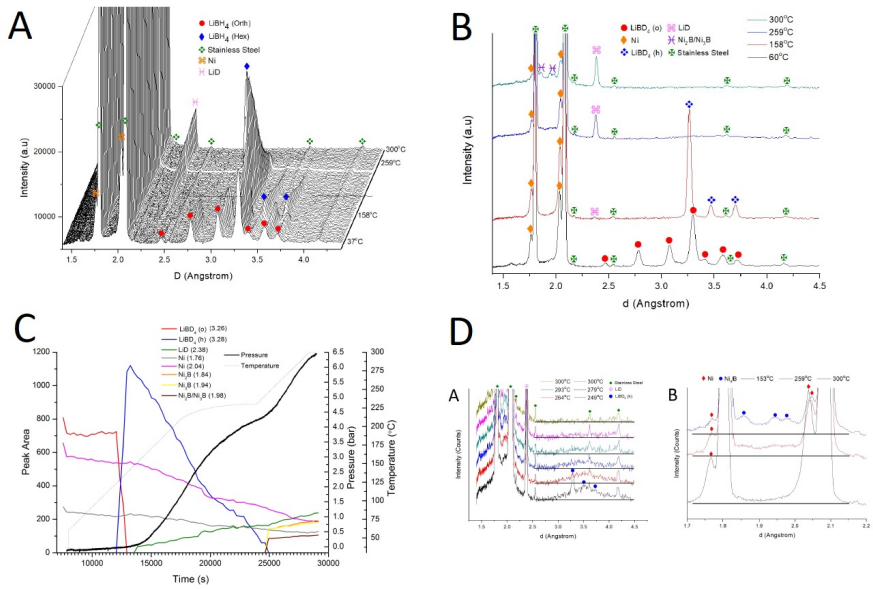

Figure 5.4: PND data for the $LiBD_4$:2Ni system. A - Waterfall Plot B - Superplot C - Integrated peaks plot D - Amorphous Region Analysis

$$LiBD_4(o)_{+}2Ni \rightarrow LiBD_4(h) + 2Ni \tag{5.2}$$

$$LiBD_4(h) + 2Ni \rightarrow LiH + [Ni_3B/Ni_2B] + \frac{3}{2}H_2 \tag{5.3}$$

To more accurately track at which temperatures the different reactions occurred, equations 5.2 and 5.3, an integrated peaks plot was constructed, figure 4.23 and C in figure 5.4. From this it can be seen that no significant decomposition of the system occurs before the phase transition at 120 °C, equation 5.2, but once this was complete the decomposition began rapidly. This reduction in the hexagonal peak area is accompanied by the reduction in the two nickel peak areas as well as an appearance of an LiD peak. Interestingly while the LiD peak area continues to increase, with reductions to both $LiBD_4$ and nickel, no observable boron containing

species were observed until the nickel boride peaks appear at 260 °C which occurred at the same time as a complete loss of the $LiBD_4$ peak. However, while the $LiBD_4$ peak was no longer observed, an increase in the deuterium pressure above the sample, which is assumed to be pure for these experiments, was still occurring implying that the $LiBD_4$ had melted rather than fully decomposed, agreeing with the DSC data which also indicated that the $LiBH_4$ had melted at the same temperature. To confirm that this was indeed a melting of the $LiBD_4$ occurring selected plots were investigated and presented in figure 4.24. From these plots it can be seen that at 249 °C a significant amorphous hump is observed in the region in which the $LiBD_4$ peaks are observed and by 260 °C these peaks are no longer seen with only the amorphous hump present. As the temperature increases further still this amorphous hump decreases in intensity before being no longer observable by 300 °C indicating a full decomposition. While this melting of the $LiBH_4$ occurs another amorphous hump is observed between 1.85 and 2.05 Å and selected plots showing this are presented in figure 4.24 and D in figure 5.4. At 160 °C no amorphous hump in the region between the two stainless steel peaks is present but by 259 °C a significant hump has appeared. By 300 °C the first nickel boride peaks are observed to appear from this amorphous hump. PND studies for the $LiBD_4$:$CaNi_5$ system could not determine in what state the boron had taken during the decomposition until nickel borides had formed at higher temperatures. From this study it appears that as the nickel reacts with the $LiBD_4$ at low temperatures it forms an amorphous Ni_3B species, indicated by the hump, after which crystalline nickel borides form

once a temperature of 300 °C has been reached.

Owing to the melting of the $LiBH_4$ and the formation of crystalline nickel borides occurring at above 260 °C it was decided to investigate the possibility of keeping the temperature of decomposition below the melting point. Figure 4.25 and A in figure 5.5 presented these isothermal experiments and found that it was possible to decompose the $LiBH_4$ at the three temperatures below 260 °C with varying success. After 1 hour of decomposition at the designated temperature it was found that at 250 °C up to 1.8 wt% could be desorbed which compared to when the system is heated at 10 °Cmin^{-1} up to 300 °C (27 minutes) 2.2 wt % is released. For the other two temperatures, 200 and 225 °C, 1.4 and 1.6 wt% were released respectively. At all three temperatures mass loss was found to be greater than that of the $2LiBH_4CaNi_5$

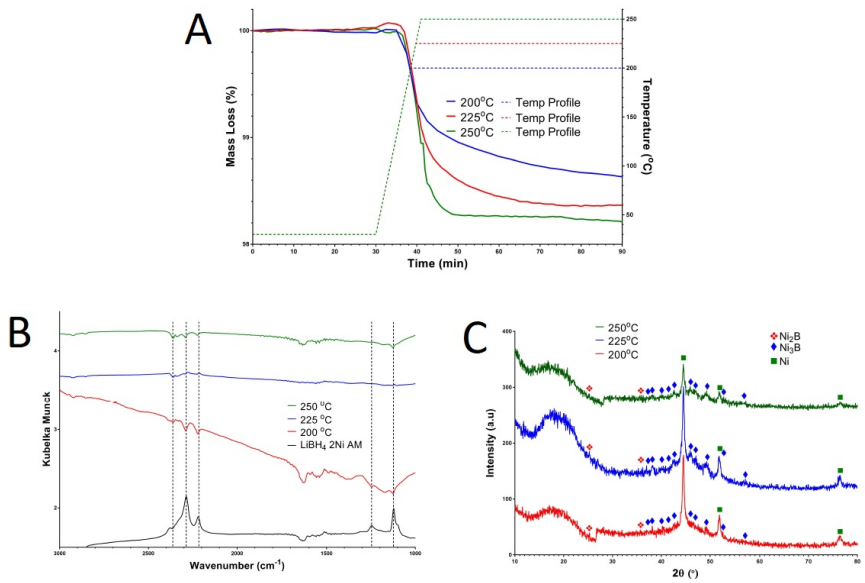

Figure 5.5: Low temperature data for the $LiBD_4$:2Ni system. A - Isothermal decomposition profiles B - FTIR data C - XRD data.

system upon heating to 585 °C. When the end products were analysed using FTIR and XRD, figures 4.26, 4.27 and B/C in figure 5.5 , it was found that from the FTIR results some $LiBH_4$ is still present for all three systems, especially for the sample decomposed at 200 °C, owing to full decomposition taking longer than the two hours tested for in total. XRD data for the formed products shows that all three systems have begun to form nickel borides, especially Ni_3B, with the relative nickel intensity decreasing and Ni_3B increasing as the temperature was raised.

5.1.4 Reversibility

One of the key challenges for using $LiBH_4$ as an on-board hydrogen storage medium for cars is that it suffers from poor reversibility and needs to be improved. To continue the efforts to carry out all reactions for the $LiBH_4$:2Ni system in the solid state the same three temperatures used for the isothermal decompositions were also chosen to conduct reversibility studies at. Figure 4.28, and A in figure 5.6, presents the three hydrogenation isotherms at 200, 225 and 250 °C. From this data it can be seen that none of the three systems are able to reach the end of the hydrogenation plateau for the system and therefore it was not possible to conduct a van't Hoff plot for this system. With the apparatus available it was only possible to reach 120 bar of pressure above the sample and from these results it appears that the plateau pressure is around this value. To reach the end of the plateau higher pressures of H_2 are required to complete the PCI plots. Another indicator that the end of the

plateau has not been reached is that the total uptake at the three temperatures only reached a maximum of 1.42 wt% at 200 °C where a total uptake of greater than 2 wt% would be expected for the system. To further quantify the extent of reversibility post-hydrogenation TGA results were collected and presented in figure 4.29 and B in figure 5.6. From these it can be seen that there is a mismatch between the results presented in the hydrogenation isotherms and those of the TGAs. For the 200 °C sample there was a difference of 0.18 %, for the 225 °C system a difference of 0.08 % and for the the 250 °C sample a difference of 0.2 % was observed. This discrepancy between the two apparatus is attributed to incomplete decomposition of the sample at the particular temperatures and also a small leak was detected after the completion of the experiments. For this reason the results presented in the TGA are the more convincing of the two results.

To ensure that $LiBH_4$ has been reformed, rather than another species, FTIR was used to detect the presence of the B-H bonds and these results are presented in figure 4.30 and C in figure 5.6. The results at all three temperatures show that the expected peaks at 1000-1300 and 2200-2400 cm^{-1} regions were all observed indicating that at least some of the $LiBH_4$ has begun to reform from the decomposition end products.

One area to consider in future work is how the density of the material will fluctuate during cycling experiments. This change in density could result in contracting and swelling of the material which will affect the integrity of the reaction vessel. Early

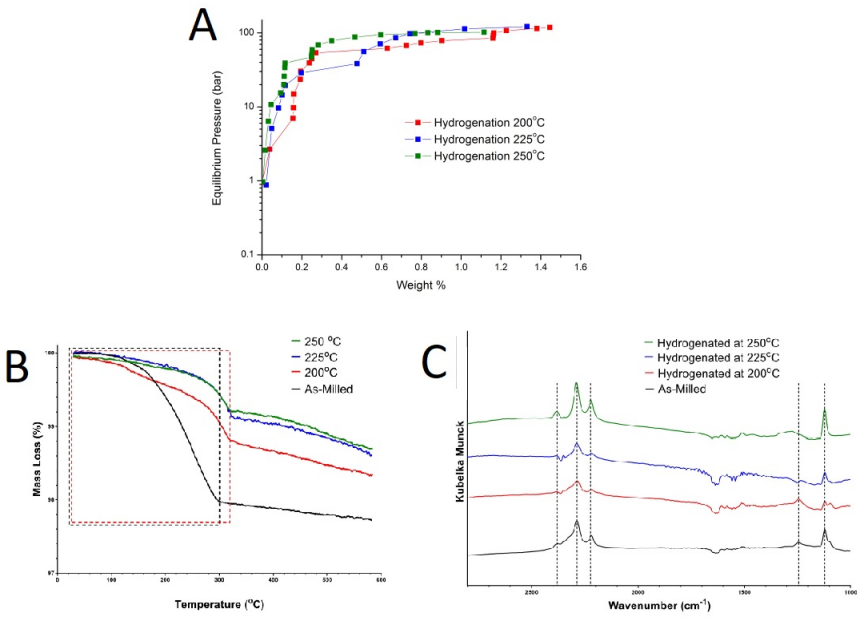

Figure 5.6: Reversibility data for the $LiBD_4$:2Ni system. A - PCI plots B - TGA data C - FTIR data.

studies bv Nasako *et al.* demonstrated that the greatest amount of stress occurs at the bottom of the reaction vessel during cycling and that stress on the vessel increases every cycle [152]. Further experiments by Charlas *et al.* showed that three different mechanisms were responsible for the mechanical stress on the reaction vessel [153]. These included the change in porosity of the material, settlement of the hydride during cycling and finally the difference in porosity between hydrided and unhydrided states of the material.

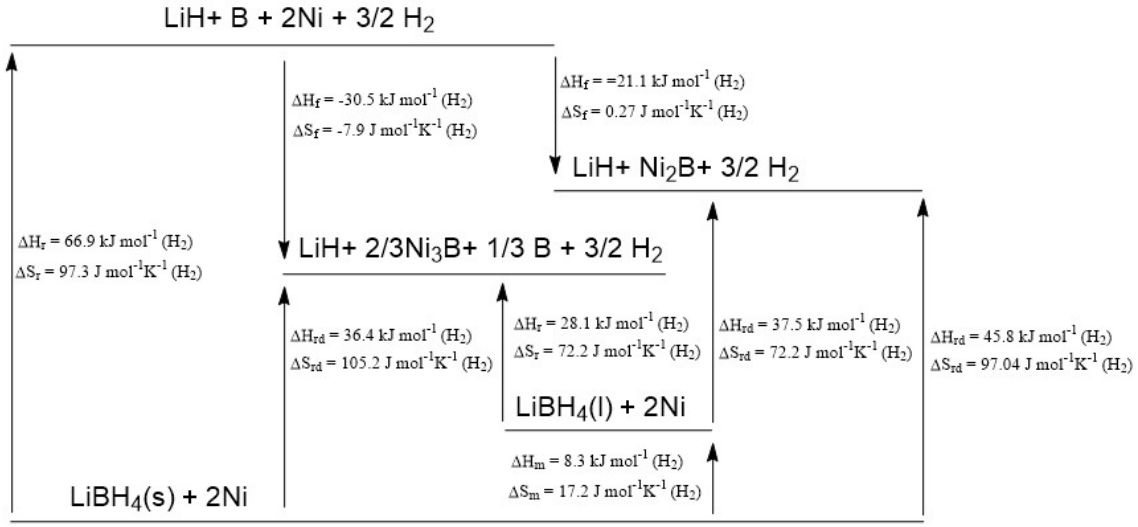

Figure 5.7: Enthalpy and entropy diagram for the $LiBH_4$:2Ni system using data from Price *et al.* and Teppa *et al.* [72, 151].

5.1.5 Thermodynamic Assessment

While no experimental data could be gathered to assess the thermodynamics of the system theoretical data can be used to calculate the T(1 bar) for the destabilisation reactions occurring and is summarised in figure 5.7. The paper by Price *et al.* calculated the enthalpy and entropy values for the decomposition of $LiBH_4$ as well as the fusion of $LiBH_4$ to a liquid state [72]. For the $LiBH_4$ system it has been shown that by 300 °C the primary species formed is Ni_3B and by 585 °C Ni_2B has been formed instead and the formation enthalpies and entropies for both species have been included in the table, as a comparison, with values for them taken from the Teppa *et al.* paper [151]. For the formation of Ni_3B, which can occur below the melting of $LiBH_4$, a calculated ΔH_{rd} of 36.4 kJ mol^{-1}(H_2) and a ΔS_{rd} 105.2 J mol^{-1} K^{-1} (H_2). T(1 bar) is calculated using equation 5.4, with the resulting

T(1bar) for the destabilisation of $LiBH_4$ and formation of Ni_3B as 73 °C. When the formation of Ni_2B is taken into account instead then the T(1 bar) is calculated as 199 °C. Decomposition for the $LiBH_4$:2Ni system does not begin until 140 °C so the value of 73 °C does seem slightly low but both these values compare favourably against previous systems such as the addition of lithium alanate by Meggough *et al.* who found that the T(1 bar) could be reduced to 240-300 °C and the value for as-received $LiBH_4$ of 414 °C.

$$\mathrm{T(1bar)} = \frac{\Delta \mathrm{H}}{\Delta \mathrm{S}} \tag{5.4}$$

5.1.6 Summary

Initial experiments indicated that the $LiBH_4$:2Ni system showed the most promise in improving the properties observed from the $2LiBH_4$:$CaNi_5$ system. From the decomposition experiments it appears that reaction between the nickel and boron produces an amorphous nickel boride species before crystallising to primarily form Ni_3B by 300 °C. Other experiments also indicate that the stoichiometrically preferred Ni_2B does not form until the decomposition temperature is increased past the melting point of the $LiBH_4$. The reaction equations for the system were therefore postulated below. By 300 °C, equation 5.5, a partial reaction between the $LiBH_4$ and the nickel had occurred to form two different borides, Ni_3B and Ni_2B, with some nickel and $LiBH_4$ remaining. At this temperature exact quantities of these reaction

products could not be determined. By 585 °, equation 5.6, a complete reaction has now occurred between the remaining $LiBH_4$ and nickel while the Ni_3B formed at low temperatures has changed to completely form the expected stoichiometric product Ni_2B.

$$LiBH_4 + 2Ni \rightarrow (LiH + Ni_3B + Ni_2B + LiBH_4 + Ni + H_2) \quad (300°C) \tag{5.5}$$

$$LiH + (Ni_3B + Ni_2B + LiBH_4 + Ni) \rightarrow LiH + Ni_2B + \frac{3}{2}H_2 \quad (585°C) \tag{5.6}$$

With the melting of the $LiBH_4$ confirmed to occur at 260 °C, from PND experiments, the ability to carry out the decomposition only in the solid state was investigated. Isothermal experiments below this temperature did see decomposition at 250 °C and lower while still maintaining an increased mass loss over that of the $2LiBH_4$:$CaNi_5$ system. Reversibility studies were also carried out at these solid-state temperatures and were found to be successful in regenerating $LiBH_4$ at 120 bar. Unfortunately, the experiments were limited by the inability to increase the pressure further and complete the PCIs to obtain accurate thermodynamic data from van't Hoff plots. Theoretical data, however, predicts a T(1 bar) as low as 73 °C for the formation of Ni_3B or 199 °C for the formation of Ni_2B.

Table 5.1 shows the system parameters for the $LiBH_4$:2Ni system compared against the target figures derived from the DOE targets. This system can currently only

meet a third of the desired storage capacity for the system but does maintain a 91% capacity when decomposed below 300 °C. Reversible capacity is not as superior as the original capacity but could be improved further if greater hydrogen pressures can be used during cycling experiments. While only one reversible cycle was presented here once the plateau pressure can be determined multiple cycling experiments will be required to determine if any storage capacity degradation will occur.

Table 5.1: Comparison of $LiBH_4$:2Ni system against system targets for thermodynamic turning of $LiBH_4$.

System Parameter	Target	$LiBH_4$:2Ni
Gravimetric Capacity (wt%)	6.5	2.3
Gravimetric Capacity (wt%) in Solid State (< 300 °C)	6.5	2.1
Reversible storage capacity (wt%)	6.5	1.42
Decomposition Temperature (°C)	85	140-280

5.2 Lithium Borohydride and Silicon

5.2.1 Introduction

Section 4.3 of this work dealt with the addition of silicon to attempt to thermodynamically tune $LiBH_4$ by forming either silicon borides or lithium silicates. The boron-silicon phase diagram, figure 5.8 [154], predicts that two main silicon borides will form: SiB_6 and SiB_3. From this it was decided that the 3:1 and 6:1 $LiBH_4$ to silicon systems would be studied along with a more silicon rich 1:1 system to determine if greater quantity of nickel would aid in the formation of the silicon borides.

When looking at a phase diagram of lithium and silicon, figure 5.9, it can be seen that

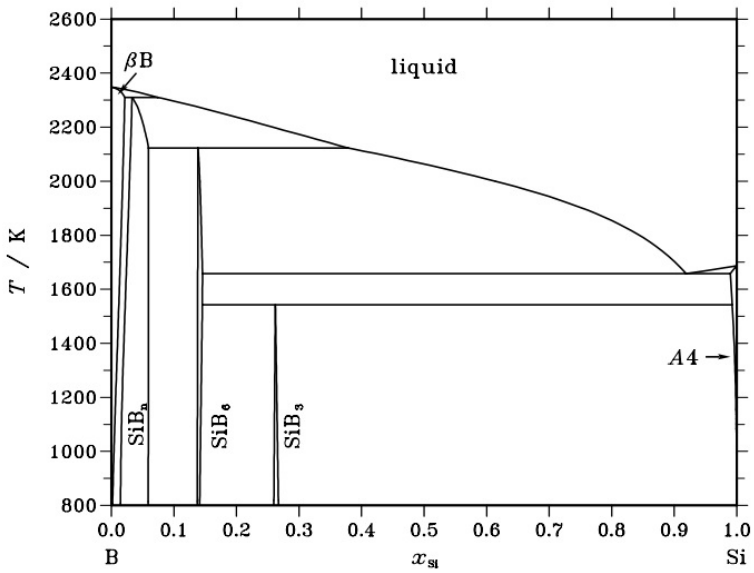

Figure 5.8: Phase diagram for the boron-silicon system. [154].

several phases can be formed including $Li_{22}Si_5$, $Li_{13}Si_4$, Li_7Si_3 and $Li_{12}Si_7$ [155]. From these potential end products it was decided to focus upon the $Li_{22}Si_5$ formation owing to the potential for the highest weight capacity of all the ratios. It was also discovered that $Li_{4.4}Si$ can also be formed through high-energy ball-milling when creating battery electrodes [156]. As milling is also a key processing step for $LiBH_4$ storage systems this was an indicator that a reaction could be expected. Zhang *et al.* demonstrated that the use of a catalyst with this reaction aided in the formation of lithium silicates during decomposition and improve the reversibility of the system with up to 4 wt% being reversible [65]. TiF_3 catalyst levels for the Zhang *et al.* research were 10 and 30 wt% of the system mass. In view of this selected catalyst levels of 10, 20 and 30wt% were chosen for investigation with 20 wt% chosen as a useful mid point reference.

From the Zhang *et al.* paper it was also found that when 30 wt% TiF_3 was used the onset decomposition was observed to be as low as 70 °C and 4 wt% was desorbed by 300 °C [65]. When compared to the results presented here the onset decomposition is comparable to Zhang *et al.*'s results but a mass loss of just over 3 wt% by 300°C is lower as it gives a total mass loss of 8 vs 10 wt%. When no TiF_3 catalyst was used Li_4SiO_4 was formed during the reaction with $LiBH_4$. Zhang *et al.* postulated that the formation of this silicate would hinder rehydrogenation and thus used the TiF_3 catalyst. The end-products formed when using the TiF_3 catalyst did not show any silicate formation and instead showed LiF as the primary species, similarly to

the results presented in this report. Regeneration was found to proceed for the catalyst containing system but no evidence of $LiBH_4$ reformation was discovered indicating that other species were formed. Moosegard *et al.* also studied the use of SiO_2, but with no catalyst, and confirmed Zhang *et al.*'s hypothesis that no reversibility was possible when silicates were formed during the reaction [63]. The use of TiF_3 as a destabilising agent has also been investigated by both Fang *et al.* and Guo *et al.* [157, 158] where $LiBH_4$ was milled with TiF_3 in a 3:1 ratio. Both papers show that the onset decomposition is occurring before 100 °C with the Fang *et al.* paper showing decomposition finishing by 90 °C compared to the Guo *et al.* paper which shows decomposition finishing by 200 °C. The differences in the decomposition temperature can be explained by different milling conditions as the

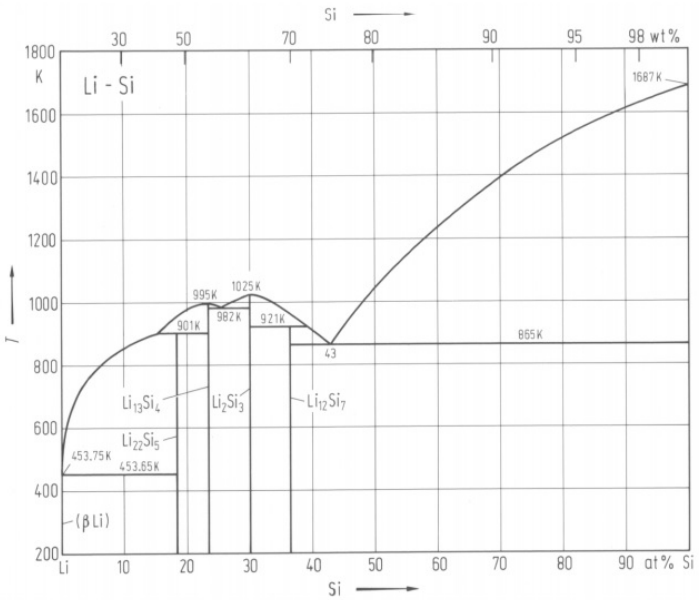

Figure 5.9: Phase diagram for the Li-Si system [155].

Guo *et al.* system was milled for only 15 minutes compared to two hours for the Fang *et al.* system. TiF_3 content, in the $3LiBH_4$:TiF_3 system, accounts for 57.5 % of the total mass compared to 30 % in the Zhang *et al.* paper.

5.2.2 Reaction Between Silicon and Boron

It has been shown that the destabilisation of $LiBH_4$ using aluminium has been successful by Kang *et al.* who were the first to demonstrate that the formation of AlB_2 could reduce the decomposition temperature to release 90 % of the stored hydrogen by 450 °C [46]. On the periodic table silicon is the next heaviest element after aluminium and should in theory only incur a small impact on the storage capacity of the system should a reaction occur. Silicon is predicted to form both SiB_6 and SiB_3 according to the phase diagram [159] and the experiments, conducted in section 4.3, primarily focused on altering milling conditions to attempt to form these compounds.

Initial milling conditions for the $6LiBH_4$:Si system were one hour to determine the minimum milling time needed to produce a reaction between the two components. XRD data for the system post-milling shows the expected peaks for both $LiBH_4$ and Si figure 4.33. Unlike the nickel systems $LiBH_4$ is observable here owing to the ratio of components favouring the $LiBH_4$. DSC and TGA data for this system, figure 4.34, showed almost identical events to those of the as-received $LiBH_4$ with the peaks corresponding to the phase transition at 120 °C, melting of the $LiBH_4$

at 295 °C and the broad decomposition between 400 and 520 °C all present. Upon melting the TGA data does show that a small mass loss is observed, as expected, but unlike the as-received $LiBH_4$ there appears to be what looks like a small mass gain of 0.2%. With the TGA apparatus confirmed to be leak tight this mass gain is attributed to the foaming of the material during the melting which appears to be more severe than that of the as-received $LiBH_4$. The only significant change compared to the as-received material, when the Si is milled in for 1 hour, is that the storage capacity has been reduced from 14 wt% to 12.5 wt% thus providing no benefit.

To enhance both the kinetics of the system and the overall mixing of the two com-

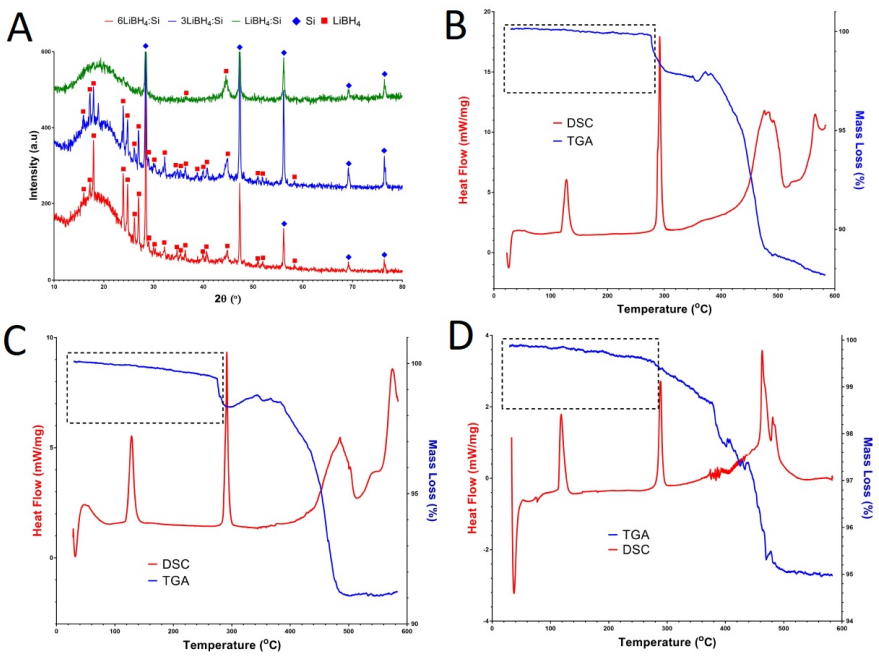

Figure 5.10: Data for the four hour ball-milled $LiBH_4$:xSi systems. A - XRD B - $LiBH_4$:6Si TGA/DSC C - $LiBH_4$:3Si TGA/DSC- D - $LiBH_4$:Si TGA/DSC.

ponents milling time was increased from 1 hour to 4 hours. For this milling time three systems were investigated: the $6LiBH_4$:Si from before, $3LiBH_4$:Si which could form the other predicted boride and $LiBH_4$:Si to determine if a higher ratio of silicon could form an unexpected product. The XRD data post-milling for the three systems, presented in figure 4.35 and A in figure 5.10, shows that for all three systems that silicon was the primary species observed with the intensity increasing as the silicon ratio increased. $LiBH_4$ was easily observed for the 6:1 and 3:1 systems but upon increasing the ratio of silicon further to the 1:1 system only two distinct $LiBH_4$ peaks were observed. Upon decomposition the $6LiBH_4$:Si system, figure 4.36 and B in figure 5.10, showed an almost identical DSC curve to that of the 1 hour milled sample with the three typical peaks observed. The TGA data again shows a similar curve to the 1 hour milled sample with the small mass loss/gain occurring alongside the melting indicating the foaming of the material. The primary mass loss occurs in the expected 400-520 °C region and a total mass loss of 12 wt% is observed. The $3LiBH_4$:Si system demonstrated similar decomposition properties, figure 4.37 and C in figure 5.10, to that of the $6LiBH_4$:Si system with the DSC data showing the three expected peaks. TGA data for this system also showed a foaming effect upon melting, the small mass gain, and a total mass loss for the system of 9 wt%. For the $LiBH_4$:Si system, figure 4.38 and D in figure 5.10, the DSC data shows the first two expected peaks, phase transition and melting, but where the broad decomposition peak usually occurs there appears to be two sharper peaks superimposed over each other. Similarly to the 6:1 system this could also indicate a reaction between the

Si and the formed end products, but again the foaming of the material prevented any analysis post-decomposition. As expected the melting of the $LiBH_4$ resulted in a small mass loss, 1 wt%, but this was a more gradual loss than usual with the primary mass loss occurring in the usual 400-520 °C region. Evidence for a reaction between the $LiBH_4$ and silicon was observed for this system but this side-reaction only seemed to occur at much higher temperatures, >400 °C, and were not able to bring the decomposition temperature below that of the melting point and prevent the foaming of the material.

Finally the milling conditions were changed once again to include one hour of soft milling followed by four hours of hard milling. This soft milling step was performed

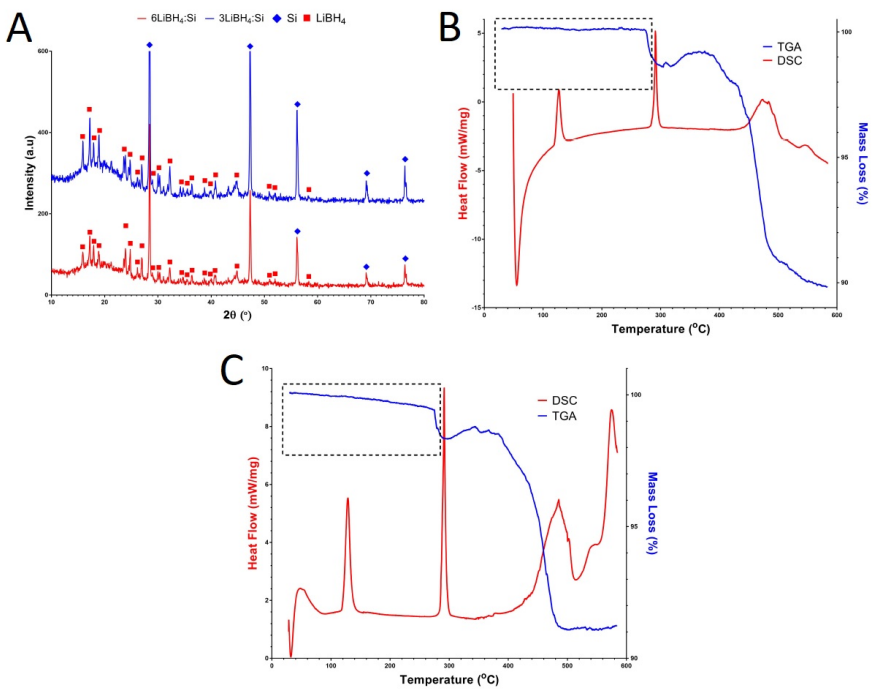

Figure 5.11: Data for the five hour ball-milled $LiBH_4$:xSi systems. A - XRD B - $LiBH_4$:6Si TGA/DSC C - $LiBH_4$:3Si TGA/DSC.

to ensure that good mixing between the two components had taken place before then hard milling at much harsher conditions. This technique by Abbas *et al.* was shown to be effective in improving the reaction between LiH and germanium [160]. The systems investigated using this two step milling technique were the $6LiBH_4$:Si and $3LiBH_4$:Si owing to their previous use and expected end products. The 1:1 system was not used owing to its much lower storage capacity than the other two systems with 5 wt% not meeting the DOE targets. XRD data for the two systems, figure 4.39 and A in figure 5.11, both show the expected $LiBH_4$ and silicon peaks more suppressed and $LiBH_4$ peaks more intense than those observed on the 3:1 system as expected. The decomposition data, figures 4.40 and 4.41 and B/C in figure 5.11, showed that for both systems the TGA data is similar to those observed with the previous milling conditions where little to no decomposition is observed until the melting of the $LiBH_4$ upon which a small mass loss, 1 wt%, is observed for both systems followed by a small mass gain owing to some oxidation occurring. After this the two systems continue to decompose in the usual 400-500 °C region and the total mass loss for the two systems is 10 and 9 wt% for the 6:1 and 3:1 systems respectively. The DSC curve for the 3:1 shows the three expected peaks for $LiBH_4$ decomposition whereas for the 6:1 system there is a suppression of the decomposition peak compared to previous experiments. This suppression of the decomposition is reflected by the slightly reduced mass loss compared to the previous milling conditions. Analysis of post-decomposition products was again not possible with the foaming of the material preventing any recovery.

From these results it can't be fully concluded if the barrier to forming silicon borides is owing to thermodynamics or kinetics. However, when looking at the literature it appears that the enthalpy of formation for AlB_2 is between -7 and -16 kJ mol^{-1} [161–163] whereas experimentally this was found to be -20 kJ mol^{-1} for the $2LiBH_4$:$LiAlH_4$ system [48]. When the enthalpy of formation for silicon borides is compared in the literature there appears to be a large range in the literature. Franke *et al.* suggested that the enthalpy of formation SiB_6 should be as low as -4.223 kl mol^{-1} (-6.415 kl mol^{-1} for SiB_3) while Domalski *et al.* indicated it could be as high as -30 kJ mol^{-1} [164]. Other papers however suggest a much higher enthalpy of formation with both Zaitsev *et al.* and Gordienko calculating the enthalpy of formation for SiB_6 to be in excess of -120 kJ mol^{-1} [165,166]. The values of -120 kJ mol^{-1} seem to be unrealistic for the formation enthalpy of SiB_6 so when the value of -30 kJ mol^{-1} is assumed to be the highest it can be, from the Domalski *et al.* paper [164], then the formation entropy will be 5.56 J mol^{-1} K^{-1}. When these values are deducted from the reaction enthalpy and entropy of $LiBH_4$ decomposition then values for destabilisation will be ΔH_{rd} of 36.9 kJ $mol^{-1}(H_2)$ and a ΔS_{rd} 91.74 J mol^{-1} K^{-1} (H_2) and this is summarised in figure 5.12. These values should give a T(1 bar) of 125 °C but because no significant decomposition for the $6LiBH_4$:Si system occurs until after 280 °C this gives evidence that kinetic barriers are preventing the reaction.

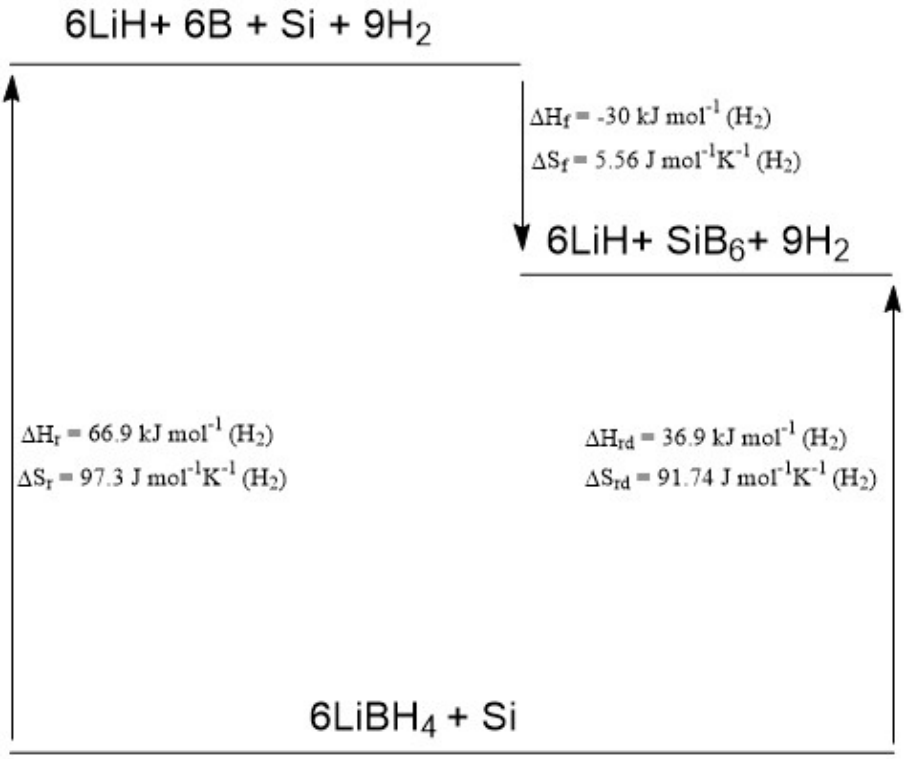

Figure 5.12: Enthalpy and entropy diagram for the $6LiBH_4$:Si system using data from Price *et al.* and Domalski *et al.* [164, 167].

5.2.3 Affect of Titanium Catalyst on reaction between $LiBH_4$ and Silicon

XRD was used to confirm the presence of components post-milling, figure 4.42. As with the non-catalysed systems the presence of both $LiBH_4$ and Si were clearly observed on the XRD patterns for all three systems. The presence of TiF_3 was also confirmed on all three spectra with the intensity of the peaks increasing with greater quantity of catalyst in the system as expected.

Decomposition data for the 4.4$LiBH_4$:Si with 10 wt% TiF_3 system was presented in figure 4.43 and A in figure 5.13, and while some decomposition for this system was observed to occur as low as 120 °C the majority of the mass loss was seen to be in the usual 400-500 °C region expected for $LiBH_4$. On the DSC curve the phase transition and melting of the $LiBH_4$ were both seen to occur at the usual temperatures of 120 and 295 °C but unlike the expected broad decomposition peak for as-received $LiBH_4$ there appeared to be three sharp peaks superimposed over the same location. These additional peaks are indicating that some reaction between the silicon and end-products, such as the LiH, are occurring but similarly to the previous systems the material foamed heavily during the melting preventing post-decomposition analysis. Decomposition for the 4.4$LiBH_4$:Si with 20 wt% TiF_3 system, figure 4.44 and B in figure 5.13, showed decomposition for the system rapidly occurring from 100 °C onwards. While the phase transition and melting of the $LiBH_4$ were still present on the DSC data they did appear to be suppressed and broader compared to that of as-

received $LiBH_4$. While decomposition was observed to occur steadily between 100 and 400 °C there was a sudden increase in the rate of mass loss which is occurring at the same time as the broad peak on the DSC curve. Similarly to the 10 wt% system this broad endotherm is superimposed but this time with one sharp peak at 460 °C. This sharp peak is another indicator that a side-reaction is occurring but unlike previous systems the foaming was suppressed by the increased quantity of TiF_3 and post-decomposition analysis was possible. As with the 20 wt% TiF_3 system, decomposition for the 4.4$LiBH_4$:Si with 30 wt% TiF_3 system was also seen to begin occurring as low as 60 °C , figure 4.45 and C in figure 5.13. On the DSC data it is observed that the phase transition and melting peaks for the $LiBH_4$ are now even more suppressed than the 20 wt% system and as a result broad peak was observed in the 300-410 °C region. This region is accompanied by an increase in the decomposition rate possibly indicating a side reaction occurring before the usual 400-500 °C decomposition region expected for as-received $LiBH_4$. Although this decomposition is observed on the DSC at 400-500 °C it is much less intense than previous systems and is only accompanied by a reduced rate in decomposition compared to the previous region. As with the 20 wt% system the melting of the $LiBH_4$ was suppressed enough to allow post-decomposition analysis.

XRD analysis of the two TiF_3 systems post-decomposition are presented in figure 4.46 and D in figure 5.13. For the 20 wt% catalyst system the dominant species observed is LiF with some trace amounts of TiF_3 still visible. With this level of catalyst

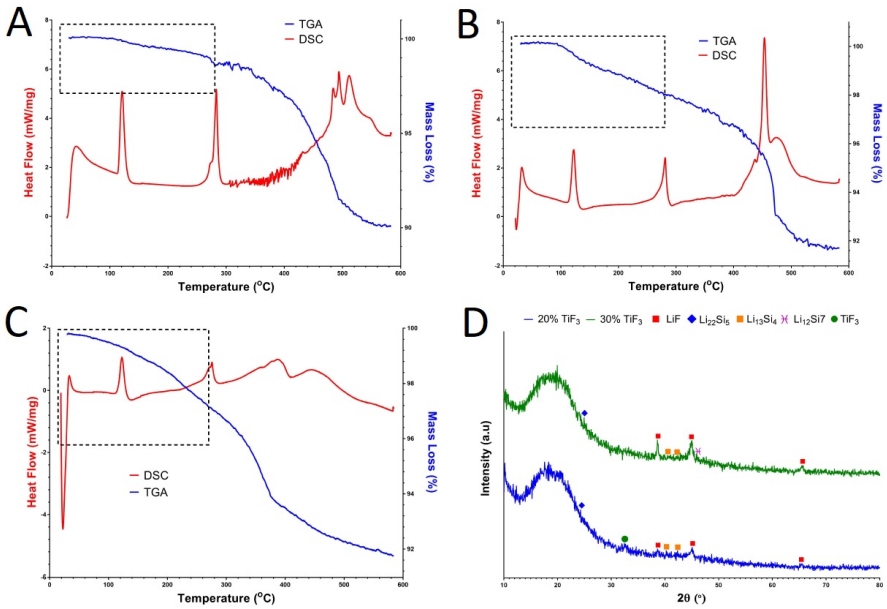

Figure 5.13: Data for the $4.4LiBH_4$:Si:x wt% TiF_3 catalyst systems. A - $4.4LiBH_4$:Si:10 wt% TiF_3 DSC/TGA B - $4.4LiBH_4$:Si:20 wt% TiF_3 DSC/TGA C - $4.4LiBH_4$:Si:30 wt% TiF_3 DSC/TGA D - XRD data for the 20 and 30 wt% TiF_3 systems.

a mix of two different lithium silicides were discovered: the expected $Li_{22}Si_5$, a small peak in the amorphous region, and $Li_{13}Si_4$, a species also predicted on the phase diagram and next closest in terms of stoichiometry. For the 30 wt% catalyst system LiF is also observed and has increased in intensity over the 20 wt% system indicating more has been formed during the decomposition. As no TiF_3 is observed this is an indication of a more complete reaction. Like the 20 wt% system the two lithium silicides, $Li_{22}Si_5$ and $Li_{13}Si_4$, were found along with evidence of a third species, $Li_{12}Si_7$. Even though the levels of TiF_3 in the system ($8.6LiBH_4$:TiF_3 atomic ratio) are not great enough to form the stoichiometric reaction $3LiBH_4 + TiF_3$, from these results the main decomposition reaction appears to be the formation of LiF with

the reaction of the lithium silicides a side-reaction.

5.2.4 Summary

The addition of elemental silicon to $LiBH_4$ does not provide any enhancement to the destabilisation of $LiBH_4$. Lithium silicides or silicon borides do not form readily with the addition of silicon. In both cases the decomposition does not occur above the melting point of the $LiBH_4$ which resulted in a severe foaming of the material. Predicted T(1bar) values do indicate a thermodynamic reaction should occur but it appears that the reaction could be kinetically limited. When a TiF_3 catalyst is added the foaming of the material was suppressed with some decomposition occurring before the melting point. Lithium silicides were observed when the catalyst was used but the primary decomposition reaction appears to be from the reaction between the $LiBH_4$ and TiF_3, with the formation of silicides as a side reaction that takes place at higher temperatures.

Table 5.2 shows the system parameters for the lithium borohydride and silicon systems compared against the DOE derived targets. While the overall storage capacities for the two systems exceed the system requirements once the criteria for low temperature decomposition is taken into account then the silicon system loses almost all of its capacity whilst the system containing the titanium catalyst maintaining 3.2 wt%. Reversibility was not studied for either of these two systems but decomposition temperature for the titanium system was superior, even though it was still

decomposing up to 585 °C.

5.3 Lithium Borohydride and Iron/Cobalt

5.3.1 Introduction

Section 4.4 of this work dealt with the addition of iron and cobalt to lithium borohydride to replicate a similar reaction observed when using nickel. When looking at the boron-iron phase diagram 5.14 [168], it can be seen that two different phases are predicted FeB and Fe_2B. Unlike the boron-nickel system no 3:1 ratio compound will be formed with a reaction between the two components. Similarly when looking at the boron-cobalt phase diagram, 5.15 [169], the two phases CoB and Co_2B are the

Table 5.2: Comparison of the two silicon systems against system targets for thermodynamic turning of $LiBH_4$.

System Parameter	Target	$6LiBH_4$:Si	$4.4LiBH_4$:Si (30 wt% TiF_3)
Gravimetric Capacity (wt%)	6.5	10	8
Gravimetric Capacity (wt%) in Solid State (< 300 °C)	6.5	0.5	3.2
Reversible storage capacity (wt%)	6.5	0	0
Decomposition Temperature (°C)	85	280-580	100-585

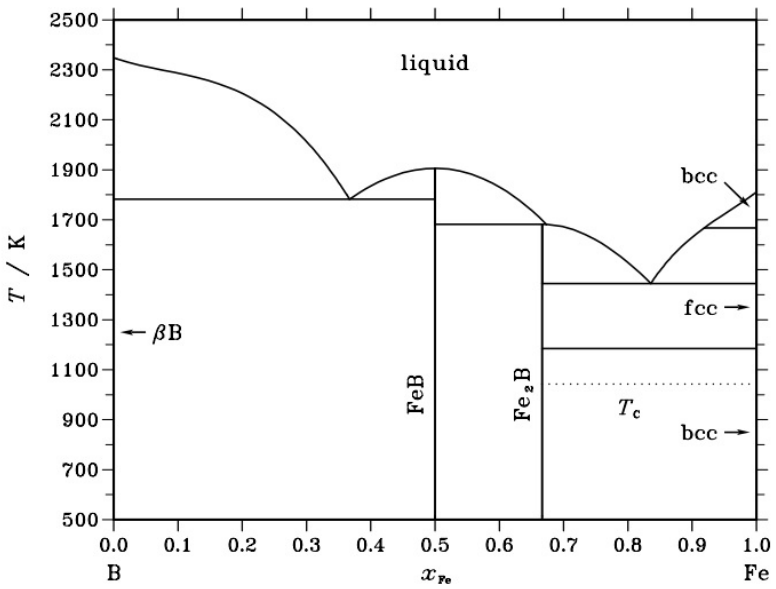

Figure 5.14: Phase diagram for the boron-iron system. [168]

primary phases predicted to form with Co_3B only forming at much higher temperatures (¿800 °C). For this reason research for these systems was focused upon the 1:1 and 2:1 metal to $LiBH_4$ ratio systems.

While the use of both cobalt and iron to destabilise $LiBH_4$ is scarce in the literature one paper did compare the use of $NiCl_2$, $FeCl_2$ and $CoCl_2$. The paper by Zhang *et al.* discovered that the chlorides of these three metals could destabilise $LiBH_4$ below 300 °C with $NiCl_2$ found to be most effective by desorbing 99 % of the stored hydrogen without the release of diborane [64]. It was found that the use of these chlorides did produce borides of the three metals while also forming LiCl during the reaction which is why almost 100 % of the stored hydrogen can be released. Interestingly it was also found that the use of the $CoCl_2$ resulted in a large formation of diborane

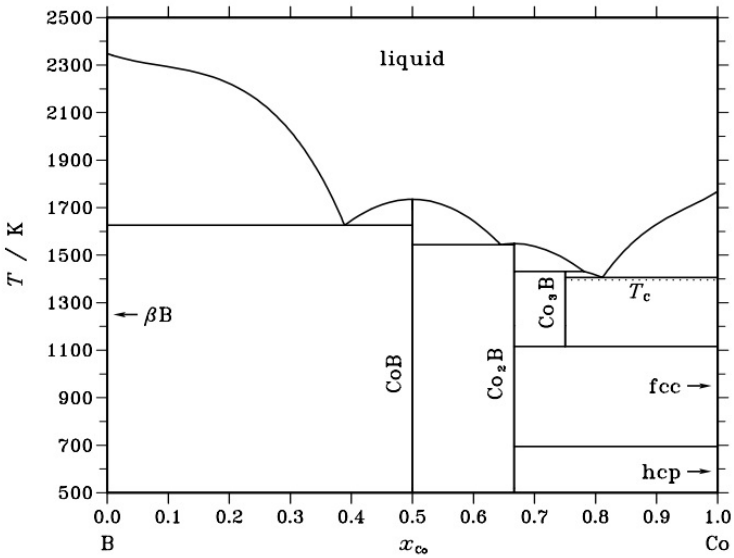

Figure 5.15: Phase diagram for the boron-cobalt system. [169]

during the decomposition, compared to the nickel and iron chlorides. Cai *et al.* investigated the use of preformed CoB to aid in the decomposition of $LiBH_4$ [170]. When milled in a 1:1 weight ratio it was found that significant decomposition could be accomplished at 350 °C with up to 10.4 wt% released. During the decomposition the CoB was transformed to Co_3B, even though Co_3B is an unfavoured product, it forms readily during $LiBH_4$ decomposition.

5.3.2 Decompostion Using Iron and Cobalt

Having successfully managed to destabilise $LiBH_4$ with nickel it was decided to try and achieve a similar reaction using other transition metals. Iron and cobalt were selected as they are both lighter than nickel, therefore reducing the impact on the

system storage capacity. According to phase diagrams both metals are predicted to form borides [168,169]. The phase diagrams suggest that, unlike a Ni-B system, the 1:1 ratio is favoured along with the 1:2 system ($LiBH_4$:Co/Fe).

From the XRD data for the as-received cobalt and iron, figure 4.47, it can be seen that for these two materials a large amount of fluorescence is taking place. The iron has a far more recognisable spectrum owing to the presence of its two distinct peaks. In contrast the cobalt spectrum is far less distinct as it comprises of only two small, broad peaks. For the $LiBH_4$:2Fe and $LiBH_4$:Fe systems it can be seen on the XRD data, figure 4.48, that the iron species is visible on both sets of data along with only a trace amount of the $LiBH_4$. Similarly to the nickel systems $LiBH_4$ is difficult to observe owing to both its poor ability to scatter x-rays and its dilute presence in the system. When the quantity of iron was increased for the $LiBH_4$:2Fe system it can be seen that the intensity of the peak has decreased and become more broad. While no distinct peaks for other species were observed at this time this reduction in peak size would indicate that some reaction between the $LiBH_4$ and iron has occurred during milling similarly to the $LiBH_4$:xNi (x=3, 2.5 and 2) systems. For the $LiBH_4$:2Co and $LiBH_4$:Co systems' XRD data, figure 4.52, it can be seen that the cobalt peaks are still present but owing to the greater fluorescence of the cobalt the observation of $LiBH_4$ is more obscured than both the iron and nickel systems. Cobalt peaks are observed to be more intense for the $LiBH_4$:Co system but with this system it can also be seen that CoB has been formed confirming that some reaction is occurring during

the milling process with the CoB formed for the $LiBH_4$:2Co system potentially not in a quantity great enough to appear on the XRD data.

Investigations into the decomposition of the $LiBH_4$:Fe and $LiBH_4$:2Fe systems was presented in figures 4.49 and 4.50 and A/B in figure 5.16. For both the $LiBH_4$:2Fe and $LiBH_4$:Fe systems it was observed that the phase change and melting of the $LiBH_4$ were still present. Unlike the nickel systems it did appear that the melting of the $LiBH_4$ occurring much closer to the as-received 295 °C at 270 and 280 °C for the $LiBH_4$:2Fe and $LiBH_4$:Fe systems respectively. Decomposition for the $LiBH_4$:2Fe system was observed to begin occurring at the lower temperature of 120 °C, along with the phase change, similarly to the $LiBH_4$:2Ni system. However, for the $LiBH_4$:Fe system decomposition did not proceed rapidly until after 240 °C. The decomposition of the $LiBH_4$:Fe system was observed to occur in one step whereas in comparison for the $LiBH_4$:Ni system it has at least two stages of decomposition occurring on the TGA data. The majority of the decomposition for the $LiBH_4$:2Fe system was observed to be complete by 360 °C, 60 °C higher than the $LiBH_4$:2Ni

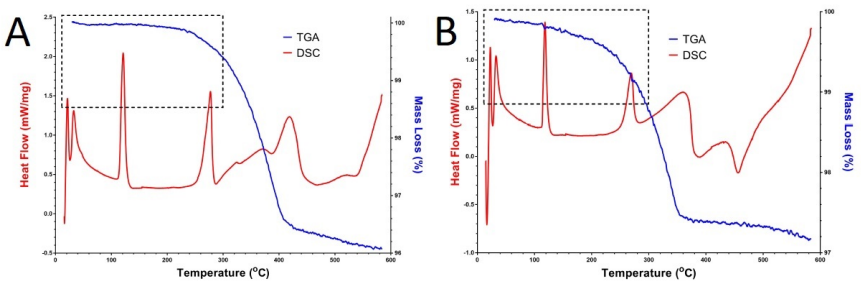

Figure 5.16: TGA/DSC data for the $LiBH_4$:Fe and $LiBH_4$:2Fe systems. A - $LiBH_4$:Fe B - $LiBH_4$:2Fe.

system, while the $LiBH_4$:Fe system had completed its primary decomposition by 400 °C, similar to that of the $LiBH_4$:Ni system. For the $LiBH_4$:2Ni system the decomposition peak on the DSC, figure 4.9, was observed as a broad peak occurring before and after the melting of the $LiBH_4$. However, for the $LiBH_4$:2Fe system decomposition was observed by DSC not to proceed rapidly until after the melting at 280 °C after which a broad peak is observed between 280 and 400 °C. For the $LiBH_4$:2Fe system a peak at 460 °C was observed, similar to that of the $LiBH_4$:2Ni system, possibly indicating a similar stoichiometric rearrangement reaction to form Fe_2B. For the $LiBH_4$:Fe system decomposition on the DSC is observed to occur primarily above the melting point with a broad peak forming at 300 °C. This broad peak appears to be superimposed by a second broad peak at 330 °C and a final, sharper peak 420 °C. This combination of peaks could indicate several different reactions contributing to the decomposition of the $LiBH_4$ and formation of several different iron borides: FeB, Fe_2B and Fe_3B. Total mass loss for the 2Fe and Fe systems respectively was 2.8 and 3.9 wt%. The theoretical storage capacity for the $LiBH_4$:2Fe and $LiBH_4$:Fe systems ,if LiH is formed, is 2.21 and 3.89 wt% respectively. The total experimental capacity at 585 °C for these two systems compares favourably to these values with the released hydrogen for the $LiBH_4$:2Fe reaching a capacity in which the LiH has fully decomposed. While these values seem to be an improvement over the use of nickel when looking at the mass loss below 300 °C, to minimise decomposition occurring in the molten state, the $LiBH_4$:Fe system only shows a decomposition of 1.2 wt % and $LiBH_4$:2Fe system 0.6 wt%. The

$LiBH_4$:2Ni and $LiBH_4$:Ni, by comparison, had decomposed 2.2 and 1.6 wt% by the same temperature.

The decomposition profiles for the $LiBH_4$:Co and $LiBH_4$:2Co systems, presented in figures 4.53 and 4.54 and A/B in figure 5.17, had distinct differences compared to the nickel and iron systems. For the $LiBH_4$:Co system it was observed from the TGA data that decomposition for the system occurred at temperatures as low as 60 °C. Although mass loss occurred at these relatively low temperatures both the phase change, at 120 °C, and the melting of the $LiBH_4$, at 274 °C, were still observed on the DSC data. No significant decomposition event was observed for the $LiBH_4$:Co system until the melting at 320 °C after which a broad endotherm appears which is finished by 500 °C. This broad endotherm was in the region usually associated with $LiBH_4$ decomposition and was accompanied by an increase in the rate of decomposition observed on the TGA data. However, there appears to be a smaller, sharper peak superimposed over the same region indicating that another reaction could be taking place at the temperature. For the $LiBH_4$:2Co system it

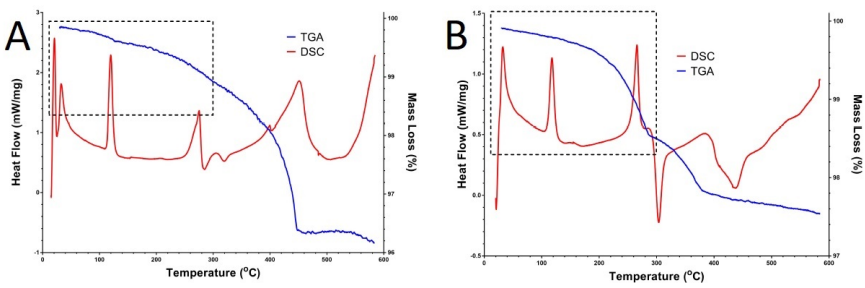

Figure 5.17: TGA/DSC data for the $LiBH_4$:Co and $LiBH_4$:2Co systems. A - $LiBH_4$:Co B - $LiBH_4$:2Co .

appears that, unlike previous 1:2 ratio systems for nickel and iron, the reaction taking place appears to occur in two stages. The phase change and melting are still observed for the $LiBH_4$:2Co system but the melting appears to show a more intense endotherm than that of the $LiBH_4$:Co system. Decomposition is observed to occur at the same low temperatures as the $LiBH_4$:Co system, <120 °C, and increases rapidly at 190 °C until 290 °C. This first rapid decomposition is accompanied by a shallow, broad endotherm on the DSC which is in the same region that the melting endotherm is superimposed over the top of it. After this first rapid decomposition a second step is observed at 300 °C and continues until 380 °C after which decomposition is much slower. During this second step a very sharp exotherm is observed followed by another broad endotherm between 330 and 400 °C. No evidence has been found to suggest what the reaction might be leading to the exotherm but it does appear to reduce the decomposition rate temporarily until the endotherm is formed. At 435 °C another exotherm is observed and this is most likely to be the result of a stoichiometric rearrangement reaction that has been seen previously for both the iron and nickel 1:2 ratio systems. Total mass loss for the two cobalt systems was found to be 2.5 and 3.9 wt% for the $LiBH_4$:2Co and $LiBH_4$:Co systems respectively and show an increased capacity over the theoretical capacities of 2.17 and 3.74 % indicating some decomposition of the LiH for each system. With the iron systems it was found that the total decomposition by 300 °C was inferior to that of the nickel systems and for the cobalt systems it can be seen that the mass loss at this temperature was 1.5 and 1.1 wt% for 2Co and Co respectively. While these values

are still inferior to those of the nickel systems it is an improvement over the iron systems capacities at this temperature.

To confirm end products formed during the decomposition XRD was utilised and the results are presented in figure 4.51 for the iron systems and figure 4.55 for the cobalt systems and summarised in figure 5.18. For both of the iron systems it was observed that a mix of several different iron borides were found. For the $LiBH_4$:2Fe system Fe_3B and FeB were both produced during the decomposition reaction and the expected Fe_2B was found to be the primary species formed during the reaction. No elemental lithium was observed on the XRD data but the mass loss on the TGA indicates that the decomposition has occurred. An reaction equation can be postulated (where square brackets are unknown quantities), equation 5.7:

$$LiBH_4 + 2Fe \rightarrow Li + [FeB + Fe_2B + Fe_3B] + 2H_2 \tag{5.7}$$

Similarly with the $LiBH_4$:Fe system a mix of the three borides was formed but the

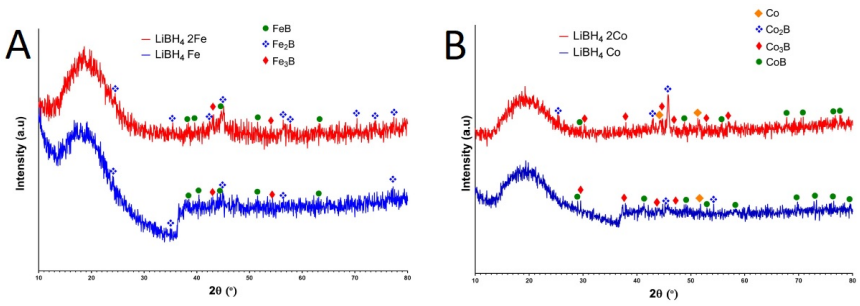

Figure 5.18: XRD data for the iron and cobalt systems. A - $LiBH_4$:Fe & $LiBH_4$:2Fe B - $LiBH_4$:Co & $LiBH_4$:2Co.

FeB peaks were marginally more intense than that of the other two borides and a reaction equation can be postulated, equation 5.8:

$$LiBH_4 + Fe \rightarrow LiH + [FeB + Fe_2B + Fe_3B] + \frac{3}{2}H_2 \tag{5.8}$$

For the formation of FeB Van Ende *et al.* were able to report a ΔH_f of -55 kJ $mol^{-1}(H_2)$ and a ΔS_f of 36 J mol^{-1} K^{-1} (H_2). The resultant enthalpy and entropy of destabilisation for the $LiBH_4$:Fe system would be ΔH_{rd} of 12 kJ $mol^{-1}(H_2)$ and a ΔS_{rd} 61.4 J mol^{-1} K^{-1} (H_2) with T(1 bar) calculated as -77 °C. From these values it would appear that the experimental thermodynamics would be much different to these literature values or the reaction is kinetically limited. No low temperature data for the entropy of Fe_2B formation could be found to calculate the T(1 bar) value.

For the cobalt systems a similar process has occurred during the decomposition in which a mix of three cobalt borides were found for both systems: CoB, Co_2B and Co_3B. For the $LiBH_4$:Co system the CoB peaks are clearly the most prominent while Co_2B and Co_3B are formed as trace species and the reaction is as follows, equation 5.9:

$$LiBH_4 + Co \rightarrow LiH + CoB + [Co_2B + Co_3B] + \frac{3}{2}H_2 \tag{5.9}$$

The $LiBH_4$:2Co system shows the clearest formation of a distinct species upon de-

composition with the Co_2B peak at 45.8 ° the most prominent. Interestingly for the 2Co system a trace amount of the elemental cobalt was found suggesting an incomplete reaction during the decomposition. The Zhang *et al.* paper did observe that the addition of $CoCl_2$ did encourage the formation of diborane [64] and if this is occurring here then the removal of boron from the system would result in elemental cobalt remaining. If a similar process has taken place with the 2Co system then it could explain why there is remaining elemental cobalt observed on the XRD data as it would be unable to react with the boron removed from the system. A reaction equation was postulated, equation 5.10:

$$LiBH_4 + 2Co \rightarrow LiH + Co_2B + [Co_3B + CoB + Co] + \frac{3}{2}H_2 \tag{5.10}$$

A possible contributing factor to the higher decomposition temperature for the iron and cobalt systems, versus the nickel systems, is the unfavourable formation of Fe_3B and Co_3B compared to Ni_3B. For the 2Ni system it was found that the formation of Ni_3B was more favourable at low temperatures after which a rearrangement reaction took place. If the formation of FeB, Fe_2B, CoB and Co_2B are the more favourable products in the reaction and they form at higher temperatures, such as Ni_2B, then this could be another cause for their poorer ability to destabilise compared to nickel.

5.3.3 Summary

The addition of cobalt and iron has provided a destabilising effect on $LiBH_4$. Both metals are able to reduce the decomposition temperature to start below 300 °C, the melting point of $LiBH_4$, and form several different borides in the process. When compared against the previous nickel systems it was found that while the use of these lighter transition metals could provide a higher system storage capacity when heated to 585 °C, but when looking only at decomposition occurring below 300 °C then nickel is the superior addition providing over 2 wt% compared to 1.5 and 1.2 wt% for the cobalt and iron respectively.

Table 5.3 shows the system parameters for the iron and cobalt systems compared against the system targets. While the $LiBH_4$:Fe and $LiBH_4$:Co systems show good overall storage capacities in total when the consideration of keeping the temperature of decomposition below 300 °C these values suddenly become very poor with the $LiBH_4$:2Fe and $LiBH_4$:2Co showing better values at these temperatures. The best decomposition temperatures of the four systems was observed to be for the $LiBH_4$:2Co system with some decomposition occurring as low as 100 °C which is not significantly higher than the system requirement of 85 °C.

Table 5.3: Comparison of the two iron systems and two cobalt systems against system targets for thermodynamic turning of $LiBH_4$.

System Parameter	Target	$LiBH_4$:Fe	$LiBH_4$:2Fe	$LiBH_4$:Co	$LiBH_4$:2Co
Gravimetric Capacity (wt%)	6.5	3.9	2.8	3.8	2.4
Gravimetric Capacity (wt%) in Solid State (< 300 °C)	6.5	0.6	1	1.1	1.5
Reversible storage capacity (wt%)	6.5	0	0	0	0
Decomposition Temperature (°C)	85	220-420	120-350	100-440	100-380

5.4 Overall Summary

This work has investigated three different approaches to destabilising lithium borohydride: using nickel, using silicon and using other transition metals. Table 5.4 shows the three best systems presented in this work compared against the system targets set out in chapter 1. From these results it can be seen that the system with the best overall storage capacity in total and in the solid state is the 4.4$LiBH_4$:Si with 30 % TiF_3 by mass with it maintaining 3.2 wt% when the temperature was kept below 300 °C. However, with this system the primary decomposition product formed was LiF which has been shown in the past to be irreversible when attempting to reform $LiBH_4$ from the end products. Out of the four iron and cobalt systems $LiBH_4$:2Co showed the best properties but when comparing this against the $LiBH_4$:2Ni system it was shown to have a similar overall storage capacity but an inferior capacity when temperatures were kept below 300 °C. Also the overall decomposition temperature range was lower for the $LiBH_4$:2Ni system even though it began to decompose at

Table 5.4: Comparison of the best systems against system targets for thermodynamic turning of $LiBH_4$.

System Parameter	Target	$4.4LiBH_4$:Si		
		$LiBH_4$:2Ni	(30 wt% TiF_3)	$LiBH_4$:2Co
Gravimetric Capacity (wt%)	6.5	2.3	8	2.4
Gravimetric Capacity (wt%) in Solid State (< 300 °C)	6.5	2.1	3.2	1.5
Reversible storage capacity (wt%)	6.5	1.42	0	0
Decomposition Temperature (°C)	85	140-280	100-585	100-380

the slightly higher temperature of 140 °C. The $LiBH_4$:2Ni system was found to be partly reversible with the equipment available but no reversibility data was gathered for the other two systems.

Chapter 6

Conclusions

The primary aim of this research was to determine if the addition of four different metallic, secondary components could provide a thermodynamic tuning reaction to decompose lithium borohydride ($LiBH_4$) at lower temperatures. Reversibility was also investigated and shown to be effective in the case of the nickel experiments.

6.1 Nickel Addition

It was shown that with the addition of nickel, $LiBH_4$ can be destabilised with the lowest decomposition temperatures observed for the $LiBH_4$:2Ni, $LiBH_4$:2.5Ni and $LiBH_4$:3Ni systems. When a 1:1 ratio was used, however, poorer decomposition was observed but the formation of NiB is thermodynamically unfavourable compared to Ni_2B and Ni_3B. Out of the other three systems the 1:2 ratio was chosen for

further investigation owing to its superior storage capacity and ability to still finish its primary decomposition before the usual melting point of $LiBH_4$ at 300 °C. From neutron diffraction studies it was determined that during decomposition the nickel and boron formed an amorphous species before crystallising into nickel borides at higher temperatures. While melting of the $LiBH_4$ was observed to occur at lower temperatures than for as-received samples it was determined that significant decomposition could still proceed at temperatures of 250 °C and lower. Reversibility was also found to occur at these low temperatures with up to 1.4 wt% hydrogen capacity. Full uptake for the system was thermodynamically limited by the available hydrogen pressure where pressures of greater than 120 bar would be needed to complete the PCI plateaus. Compared to the previously studied $CaNi_5$ system the weight capacity was found to be double for the 2Ni system but the decomposition effect was much greater and melting almost eliminated when using the alloy. Reversibility for these two systems was found to be similar with it shown to take take place at 200°C and pressures greater than 80 bar.

6.2 Silicon Addition

The investigations into the addition of silicon to destabilise $LiBH_4$ were two-fold: to form silicon borides or lithium silicides. The addition of silicon showed no lowering of the decomposition temperature even with up to four hours of intensive ball-milling combined with an hour of soft-milling. The determination of side-products

formed during the decomposition was difficult owing to the significant foaming of the material out of the sample pan but some evidence was seen on the DSC of them forming at high temperatures. The addition of a titanium fluoride catalyst did demonstrate a significant decrease in the decomposition temperature of the system, with it occurring as low as 60°C. When 20 and 30 wt% TiF_3 was used the foaming of the material was found to be suppressed and allowed analysis of the decomposed material. Post-decomposition it was found that traces of lithium silicides were formed during the decomposition but the primary species observed was LiF. From this it was determined that the primary cause of the decomposition was from the TiF_3 catalyst addition and not the silicon.

6.3 Iron and Cobalt Addition

It was demonstrated that both iron and cobalt could also be effective in destabilising $LiBH_4$ in a similar reaction to the nickel systems. All four systems investigated showed a significant reduction in the decomposition temperature where it was observed to occur below the melting point of $LiBH_4$. The total weight capacities for the 1:2 ratio systems were shown to be superior to that of the $LiBH_4$:2Ni system at 2.5 and 2.8 wt% (Fe and Co respectively) but more importantly the weight capacities at 300 °C were inferior. The inferior decomposition at low temperatures is attributed to the unfavourability of the formation of Fe_3B and Co_3B. XRD studies of the products formed showed a much greater mix of borides formed compared to

the nickel systems. For the $LiBH_4$:2Ni and $LiBH_4$3Ni systems it was observed that almost exclusively the only boride formed would be for the correct stoichiometric ratio but for the cobalt and iron systems a mix of several different borides were formed upon decomposition even at higher temperatures.

6.4 Final Conclusions

In conclusion it was found that the nickel containing systems showed the most potential in fulfilling the DOE's targets for hydrogen storage followed by the iron/cobalt and lastly the silicon systems. Even though the $LiBH_4$:2Ni systems showed an improved storage capacity over that of the previously studied $LiBH_4$:$CaNi_5$ system it still falls short of the DOE's target of 5.5 wt% by 2017. While the overall storage capacity of the $LiBH_4$:Ni ratio system comes closest to the DOE targets the decomposition reaction is not as effective as for those systems containing more nickel. One possible solution to this would be to investigate the 3$LiBH_4$:4Ni system which would theoretically store 4.35 wt% H_2, when LiH is formed, and Ni_4B_3 is an expected product predicted by the phase diagram between the components. Another possibility to meeting these targets would be to go back and investigate the Co/Fe systems further and look at the use of catalysts to bring down the decomposition temperature in line with the nickel systems and encourage formation of borides at lower temperatures.

Chapter 7

Future Work

While the $LiBH_4$:2Ni system showed an improvement of double the storage capacity of the $2LiBH_4$:$CaNi_5$ system it still does not meet the DOE's target of 5.5 wt% by 2017 or the 7 wt% ultimately. Investigations into the $3LiBH_4$:4Ni system would be the next logical step with it possessing a storage capacity of 4.35 wt% H_2 if LiH is formed. A full categorisation of this system is required including DSC/TGA studies to map to decomposition profile, XRD to confirm to formation of Ni_4B_3 and reversibility studies if the decomposition reaction shows promise. To further investigate the decomposition reaction of the $LiBH_4$:2Ni system by characterising products in amorphous states, magic angle spinning nuclear magnetic resonance (NMR) could be used to track to chemical environments that the elements in the system are residing in. The use of ^{11}B NMR with *in-situ* heating was attempted but unfortunately the highly magnetic nickel and limitations of the heater at the NMR

facilities at the University of Nottingham meant that no meaningful results could be gathered. To repeat these experiments again in future the spin speed of the sample must be kept low and the use of a facility that can heat the sample to above 300 °C would allow the full decomposition process to be observed. Finally further work required for the nickel systems is a full reversibility study of the $LiBH_4$:2Ni system with a Sieverts set-up which can handle pressures of greater than that of 120 bar. At these high pressures a complete PCI plot could be used to fully measure the reversible capacity of the system. Completed PCIs at three different temperatures would also allow the construction of a van't Hoff plot and extraction of thermodynamic data. Observation of reversibility during neutron diffraction experiments would also be useful to determine if $LiBH_4$ or other boride species are formed, as discovered by other research papers.

Further work is also needed on the cobalt and iron systems to investigate an improvement on the decomposition temperature and to determine the reversibility of the systems. As previously mentioned on possible solution to the poor decomposition at low temperatures would be to use a catalyst. This would result in some initial decomposition and to encourage low temperature formation of unfavourable borides. Reversibility of these two systems also needs to be investigated to determine if it is superior or inferior to that of the nickel systems both with and without a catalyst.

With transition metals (Ni, Co and Fe) demonstrating a significant impact on the

ability to alter the decomposition temperature of $LiBH_4$, with the formation of borides, the investigation of other, lighter elements in this series would be useful. Metals such as scandium, titanium, vanadium and chromium are all predicted to form borides. If exposed to the milling conditions presented here, and in appropriate stoichiometric ratios, then they could provide a destabilisation reaction similar to the three systems reported in this work.

Bibliography

[1] B. Dudley *et al.*, "BP statistical review of world energy 2015," 2015.

[2] C. on Climate Change, "Carbon budgets and targets - https://www.theccc.org.uk/tackling-climate-change/reducing-carbon-emissions/carbon-budgets-and-targets/."

[3] U. DECC, "Renewable energy roadmap," *Department of Energy and Climate Change, London*, 2011.

[4] R. Parkes, "Can the UK meet its renewables targets?," *Renewable Energy Focus*, vol. 13, no. 1, pp. 24 – 27, 2012.

[5] U. R. E. R. Update, "Department of energy & climate change," 2012.

[6] F. Kern, A. Smith, C. Shaw, R. Raven, and B. Verhees, "From laggard to leader: Explaining offshore wind developments in the UK," *Energy Policy*, vol. 69, pp. 635 – 646, 2014.

[7] F. Muhammad-Sukki, R. Ramirez-Iniguez, A. B. Munir, S. H. M. Yasin, S. H.

Abu-Bakar, S. G. McMeekin, and B. G. Stewart, "Revised feed-in tariff for solar photovoltaic in the United Kingdom: A cloudy future ahead?," *Energy Policy*, vol. 52, pp. 832 – 838, 2013. Special Section: Transition Pathways to a Low Carbon Economy.

[8] E. S. Trust, "Feed-in tariffs - http://www.energysavingtrust.org.uk/domestic/feed-tariffs-0."

[9] S. Singhal, "Advances in solid oxide fuel cell technology," *Solid State Ionics*, vol. 135, no. 1, pp. 305 – 313, 2000. Proceedings of the 12th International Conference on Solid State.

[10] B. C. Steele and A. Heinzel, "Materials for fuel-cell technologies," *Nature*, vol. 414, no. 6861, pp. 345–352, 2001.

[11] R. M. Ormerod, "Solid oxide fuel cells," *Chemical Society Reviews*, vol. 32, no. 1, pp. 17–28, 2003.

[12] A. L. Dicks, "Molten carbonate fuel cells," *Current Opinion in Solid State and Materials Science*, vol. 8, no. 5, pp. 379–383, 2004.

[13] J. Y. Lee, H. H. Lee, J. H. Lee, and D. M. Kim, "Alkaline fuel cell," Feb. 4 1997. US Patent 5,599,640.

[14] G. McLean, T. Niet, S. Prince-Richard, and N. Djilali, "An assessment of alkaline fuel cell technology," *International Journal of Hydrogen Energy*, vol. 27, no. 5, pp. 507–526, 2002.

[15] V. S. Bagotsky, "Phosphoric acid fuel cells," *Fuel Cells: Problems and Solutions, Second Edition*, pp. 99–106, 2012.

[16] B. Smitha, S. Sridhar, and A. Khan, "Solid polymer electrolyte membranes for fuel cell applicationsa review," *Journal of membrane science*, vol. 259, no. 1, pp. 10–26, 2005.

[17] US DOE, "Targets for onboard hydrogen storage systems for light-duty vehicles," 2017.

[18] L. Klebanoff and J. Keller, "5years of hydrogen storage research in the U.S. DOE Metal Hydride Center of Excellence (MHCoE)," *International Journal of Hydrogen Energy*, vol. 38, no. 11, pp. 4533 – 4576, 2013.

[19] T. Hua, R. Ahluwalia, J.-K. Peng, M. Kromer, S. Lasher, K. McKenney, K. Law, and J. Sinha, "Technical assessment of compressed hydrogen storage tank systems for automotive applications," *International Journal of Hydrogen Energy*, vol. 36, no. 4, pp. 3037 – 3049, 2011.

[20] T. Vezirolu and F. Barbir, "Hydrogen: the wonder fuel," *International Journal of Hydrogen Energy*, vol. 17, no. 6, pp. 391 – 404, 1992.

[21] V. P. Utgikar and T. Thiesen, "Safety of compressed hydrogen fuel tanks: Leakage from stationary vehicles," *Technology in Society*, vol. 27, no. 3, pp. 315 – 320, 2005.

[22] R. Ahluwalia and J. Peng, "Dynamics of cryogenic hydrogen storage in insu-

lated pressure vessels for automotive applications," *International Journal of Hydrogen Energy*, vol. 33, no. 17, pp. 4622 – 4633, 2008.

[23] R. Ahluwalia, T. Hua, and J. Peng, "On-board and off-board performance of hydrogen storage options for light-duty vehicles," *International Journal of Hydrogen Energy*, vol. 37, no. 3, pp. 2891 – 2910, 2012. 2010 {AIChE} Annual Meeting Topical Conference on Hydrogen Production and Storage Special Issue.

[24] S. Sherif, N. Zeytinoglu, and T. Vezirolu, "Liquid hydrogen: Potential, problems, and a proposed research program," *International Journal of Hydrogen Energy*, vol. 22, no. 7, pp. 683 – 688, 1997.

[25] J. L. Rowsell and O. M. Yaghi, "Metal–organic frameworks: a new class of porous materials," *Microporous and Mesoporous Materials*, vol. 73, no. 1, pp. 3–14, 2004.

[26] J. L. Rowsell and O. M. Yaghi, "Strategies for hydrogen storage in metal–organic frameworks," *Angewandte Chemie International Edition*, vol. 44, no. 30, pp. 4670–4679, 2005.

[27] L. J. Murray, M. Dincă, and J. R. Long, "Hydrogen storage in metal–organic frameworks," *Chemical Society Reviews*, vol. 38, no. 5, pp. 1294–1314, 2009.

[28] G. Liang, J. Huot, and R. Schulz, "Hydrogen storage properties of the mechanically alloyed LaNi5-based materials," *Journal of alloys and compounds*,

vol. 320, no. 1, pp. 133–139, 2001.

[29] W. Wallace, R. Karlicek, and H. Imamura, "Mechanism of hydrogen absorption by lanthanum-nickel (LaNi5)," *Journal of Physical Chemistry*, vol. 83, no. 13, pp. 1708–1712, 1979.

[30] B. Sakintuna, F. Lamari-Darkrim, and M. Hirscher, "Metal hydride materials for solid hydrogen storage: a review," *International Journal of Hydrogen Energy*, vol. 32, no. 9, pp. 1121–1140, 2007.

[31] M. Tanniru, H.-Y. Tien, and F. Ebrahimi, "Study of the dehydrogenation behavior of magnesium hydride," *Scripta Materialia*, vol. 63, no. 1, pp. 58–60, 2010.

[32] F. Schüth, B. Bogdanović, and M. Felderhoff, "Light metal hydrides and complex hydrides for hydrogen storage," *Chemical communications*, no. 20, pp. 2249–2258, 2004.

[33] P. Jena, "Materials for hydrogen storage: past, present, and future," *J. Phys. Chem. Lett*, vol. 2, no. 3, pp. 206–211, 2011.

[34] S.-i. Orimo, Y. Nakamori, J. R. Eliseo, A. Züttel, and C. M. Jensen, "Complex hydrides for hydrogen storage," *Chemical Reviews*, vol. 107, no. 10, pp. 4111–4132, 2007.

[35] H. I. Schlesinger and H. C. Brown, "Metallo borohydrides. III. lithium borohydride," *Journal of the American Chemical Society*, vol. 62, no. 12, pp. 3429–

3435, 1940.

[36] O. Friedrichs, A. Borgschulte, S. Kato, F. Buchter, R. Gremaud, A. Remhof, and A. Zttel, "Low-temperature synthesis of LiBH4 by gas-solid reaction," *Chemistry A European Journal*, vol. 15, no. 22, pp. 5531–5534, 2009.

[37] A. Züttel, S. Rentsch, P. Fischer, P. Wenger, P. Sudan, P. Mauron, and C. Emmenegger, "Hydrogen storage properties of LiBH4," *Journal of Alloys and Compounds*, vol. 356357, pp. 515 – 520, 2003. Proceedings of the Eighth International Symposium on Metal-Hydrogen Systems, Fundamentals and Applications (MH2002).

[38] A. Züttel, P. Wenger, S. Rentsch, P. Sudan, P. Mauron, and C. Emmenegger, "LiBH4 a new hydrogen storage material," *Journal of Power Sources*, vol. 118, no. 12, pp. 1 – 7, 2003. Scientific Advances in Fuel Cell Systems.

[39] N. Ohba, K. Miwa, M. Aoki, T. Noritake, S.-i. Towata, Y. Nakamori, S.-i. Orimo, and A. Züttel, "First-principles study on the stability of intermediate compounds of LiBH4," *Phys. Rev. B*, vol. 74, p. 075110, Aug 2006.

[40] S.-I. Orimo, Y. Nakamori, N. Ohba, K. Miwa, M. Aoki, and A. Towata, ShinichA. Züttel, "Experimental studies on intermediate compound of LiBH4," *Applied Physics Letters*, vol. 89, no. 2, 2006.

[41] . Son-Jong Hwang, *, J. Robert C. Bowman, J. W. Reiter, J. Rijssenbeek, G. L. Soloveichik, J.-C. Zhao, . Houria Kabbour, , and C. C. Ahn, "NMR

confirmation for formation of [B12H12]2- complexes during hydrogen desorption from metal borohydrides," *The Journal of Physical Chemistry C*, vol. 112, no. 9, pp. 3164–3169, 2008.

[42] O. Friedrichs, A. Remhof, S.-J. Hwang, and A. Züttel, "Role of Li2B12H12 for the formation and decomposition of LiBH4," *Chemistry of Materials*, vol. 22, no. 10, pp. 3265–3268, 2010.

[43] . Philippe Mauron, . Florian Buchter, O. Friedrichs, . Arndt Remhof, . Michael Bielmann, C. N. Zwicky, , and A. Züttel, "Stability and reversibility of LiBH4," *The Journal of Physical Chemistry B*, vol. 112, no. 3, pp. 906–910, 2008. PMID: 18088111.

[44] S. Orimo, Y. Nakamori, G. Kitahara, K. Miwa, N. Ohba, S. Towata, and A. Züttel, "Dehydriding and rehydriding reactions of LiBH4," *Journal of Alloys and Compounds*, vol. 404406, pp. 427 – 430, 2005. Proceedings of the 9th International Symposium on Metal-Hydrogen Systems, Fundamentals and Applications (MH2004)The International Symposium on Metal-Hydrogen Systems, Fundamentals and Applications, {MH2004}.

[45] G. Walker, *Solid-state hydrogen storage: materials and chemistry.* Elsevier, 2008.

[46] X.-D. Kang, P. Wang, L.-P. Ma, and H.-M. Cheng, "Reversible hydrogen storage in LiBH4 destabilized by milling with Al," *Applied Physics A*, vol. 89,

no. 4, pp. 963–966, 2007.

[47] O. Friedrichs, J. Kim, A. Remhof, F. Buchter, A. Borgschulte, D. Wallacher, Y. Cho, M. Fichtner, K. Oh, and A. Züttel, "The effect of Al on the hydrogen sorption mechanism of LiBH4," *Physical Chemistry Chemical Physics*, vol. 11, no. 10, pp. 1515–1520, 2009.

[48] M. Meggouh, D. Grant, and G. Walker, "Optimizing the destabilization of LiBH4 for hydrogen storage and the effect of different Al sources," *The Journal of Physical Chemistry C*, vol. 115, no. 44, pp. 22054–22061, 2011.

[49] D. B. Ravnsbæk and T. R. Jensen, "Mechanism for reversible hydrogen storage in LiBH4-Al," *Journal of Applied Physics*, vol. 111, no. 11, p. 112621, 2012.

[50] B. R. Hansen, D. B. Ravnsbæk, D. Reed, D. Book, C. Gundlach, J. Skibsted, and T. R. Jensen, "Hydrogen storage capacity loss in a LiBH4-Al composite," *The Journal of Physical Chemistry C*, vol. 117, no. 15, pp. 7423–7432, 2013.

[51] J. Yang, A. Sudik, and C. Wolverton, "Destabilizing LiBH4 with a metal (M= Mg, Al, Ti, V, Cr, or Sc) or metal hydride (MH2= MgH2, TiH2, or CaH2)," *The Journal of Physical Chemistry C*, vol. 111, no. 51, pp. 19134–19140, 2007.

[52] F. Kuijpers and H. Van Mal, "Sorption hysteresis in the LaNi5-H and SmCo5-H systems," *Journal of the Less Common Metals*, vol. 23, no. 4, pp. 395–398, 1971.

[53] D. Grant, J. Murray, and M. Post, "The thermodynamics of the γ-and δ-

hydrides and deuterides of CaNi5," *The Journal of Chemical Thermodynamics*, vol. 19, no. 11, pp. 1217–1226, 1987.

[54] A. Ibikunle, A. Goudy, and H. Yang, "Hydrogen storage in a CaH2/LiBH4 destabilized metal hydride system," *Journal of Alloys and Compounds*, vol. 475, no. 1, pp. 110–115, 2009.

[55] M. Meggouh, D. M. Grant, O. Deavin, M. Brunelli, T. C. Hansen, and G. S. Walker, "Investigation of the dehydrogenation behavior of the 2LiBH4:CaNi5 multicomponent hydride system," *International Journal of Hydrogen Energy*, vol. 40, no. 7, pp. 2989–2996, 2015.

[56] J. J. Vajo, W. Li, and P. Liu, "Thermodynamic and kinetic destabilization in LiBH4/Mg2NiH4: promise for borohydride-based hydrogen storage," *Chemical Communications*, vol. 46, no. 36, pp. 6687–6689, 2010.

[57] W. Li, J. J. Vajo, R. W. Cumberland, P. Liu, S.-J. Hwang, C. Kim, and R. C. Bowman Jr, "Hydrogenation of magnesium nickel boride for reversible hydrogen storage," *The Journal of Physical Chemistry Letters*, vol. 1, no. 1, pp. 69–72, 2009.

[58] X. Zhao, S.-m. Han, Y. Li, X.-c. Chen, and D.-d. Ke, "Effect of CeH2.29 on the microstructures and hydrogen properties of LiBH4-Mg2NiH4 composites," *International Journal of Minerals, Metallurgy, and Materials*, vol. 22, no. 4, pp. 423–428, 2015.

[59] M. Au and A. Jurgensen, "Modified lithium borohydrides for reversible hydrogen storage," *The Journal of Physical Chemistry B*, vol. 110, no. 13, pp. 7062–7067, 2006.

[60] M. Au, A. Jurgensen, and K. Zeigler, "Modified lithium borohydrides for reversible hydrogen storage (2)," *The Journal of Physical Chemistry B*, vol. 110, no. 51, pp. 26482–26487, 2006.

[61] M. Au, A. R. Jurgensen, W. A. Spencer, D. L. Anton, F. E. Pinkerton, S.-J. Hwang, C. Kim, and R. C. Bowman Jr, "Stability and reversibility of lithium borohydrides doped by metal halides and hydrides," *The Journal of Physical Chemistry C*, vol. 112, no. 47, pp. 18661–18671, 2008.

[62] Y. Nakamori, H. Li, K. Miwa, S.-i. Towata, and S.-i. Orimo, "Syntheses and hydrogen desorption properties of metal-borohydrides M(BH4)n (M= Mg, Sc, Zr, Ti, and Zn; n= 2-4) as advanced hydrogen storage materials," *Materials transactions*, vol. 47, no. 8, pp. 1898–1901, 2006.

[63] L. Mosegaard, B. Møller, J.-E. Jørgensen, Y. Filinchuk, Y. Cerenius, J. C. Hanson, E. Dimasi, F. Besenbacher, and T. R. Jensen, "Reactivity of LiBH4: in situ synchrotron radiation powder X-ray diffraction study," *The Journal of Physical Chemistry C*, vol. 112, no. 4, pp. 1299–1303, 2008.

[64] B. J. Zhang and B. H. Liu, "Hydrogen desorption from LiBH4 destabilized by chlorides of transition metal Fe, Co, and Ni," *international journal of hydrogen*

energy, vol. 35, no. 14, pp. 7288–7294, 2010.

[65] Y. Zhang, W.-S. Zhang, M.-Q. Fan, S.-S. Liu, H.-L. Chu, Y.-H. Zhang, X.-Y. Gao, and L.-X. Sun, "Enhanced hydrogen storage performance of LiBH4-SiO2-TiF3 composite," *The Journal of Physical Chemistry C*, vol. 112, no. 10, pp. 4005–4010, 2008.

[66] X. Yu, D. Grant, and G. Walker, "Low-temperature dehydrogenation of LiBH4 through destabilization with TiO2," *The Journal of Physical Chemistry C*, vol. 112, no. 29, pp. 11059–11062, 2008.

[67] M. Au, W. Spencer, A. Jurgensen, and C. Zeigler, "Hydrogen storage properties of modified lithium borohydrides," *Journal of Alloys and Compounds*, vol. 462, no. 1, pp. 303–309, 2008.

[68] X. Yu, D. Grant, and G. Walker, "Dehydrogenation of LiBH4 destabilized with various oxides," *The Journal of Physical Chemistry C*, vol. 113, no. 41, pp. 17945–17949, 2009.

[69] J. J. Vajo, S. L. Skeith, and F. Mertens, "Reversible storage of hydrogen in destabilized LiBH4," *The Journal of Physical Chemistry B*, vol. 109, no. 9, pp. 3719–3722, 2005.

[70] U. Bösenberg, S. Doppiu, L. Mosegaard, G. Barkhordarian, N. Eigen, A. Borgschulte, T. R. Jensen, Y. Cerenius, O. Gutfleisch, T. Klassen, *et al.*, "Hydrogen sorption properties of MgH2-LiBH4 composites," *Acta Materialia*,

vol. 55, no. 11, pp. 3951–3958, 2007.

[71] X. Yu, D. Grant, and G. Walker, "A new dehydrogenation mechanism for reversible multicomponent borohydride systemsthe role of Li–Mg alloys," *Chemical communications*, no. 37, pp. 3906–3908, 2006.

[72] T. Price, D. Grant, I. Telepeni, X. Yu, and G. Walker, "The decomposition pathways for LiBD4–MgD2 multicomponent systems investigated by in situ neutron diffraction," *Journal of Alloys and Compounds*, vol. 472, no. 1, pp. 559–564, 2009.

[73] G. S. Walker, D. M. Grant, T. C. Price, X. Yu, and V. Legrand, "High capacity multicomponent hydrogen storage materials: Investigation of the effect of stoichiometry and decomposition conditions on the cycling behaviour of LiBH4–MgH2," *Journal of Power Sources*, vol. 194, no. 2, pp. 1128–1134, 2009.

[74] T. E. Price, D. M. Grant, V. Legrand, and G. S. Walker, "Enhanced kinetics for the LiBH4:MgH2 multi-component hydrogen storage system–the effects of stoichiometry and decomposition environment on cycling behaviour," *international journal of hydrogen energy*, vol. 35, no. 9, pp. 4154–4161, 2010.

[75] D. J. Siegel, C. Wolverton, and V. Ozoliņš, "Thermodynamic guidelines for the prediction of hydrogen storage reactions and their application to destabilized hydride mixtures," *Physical review B*, vol. 76, no. 13, p. 134102, 2007.

[76] S.-A. Jin, Y.-S. Lee, J.-H. Shim, and Y. W. Cho, "Reversible hydrogen storage in LiBH4- MH2 (M= Ce, Ca) composites," *The Journal of Physical Chemistry C*, vol. 112, no. 25, pp. 9520–9524, 2008.

[77] F. Pinkerton and M. Meyer, "Reversible hydrogen storage in the lithium borohydridecalcium hydride coupled system," *Journal of Alloys and Compounds*, vol. 464, no. 1, pp. L1–L4, 2008.

[78] J.-H. Lim, J.-H. Shim, Y.-S. Lee, Y. W. Cho, and J. Lee, "Dehydrogenation behavior of LiBH4/CaH2 composite with NbF5," *Scripta Materialia*, vol. 59, no. 12, pp. 1251–1254, 2008.

[79] J.-H. Lim, J.-H. Shim, Y.-S. Lee, J.-Y. Suh, Y. W. Cho, and J. Lee, "Rehydrogenation and cycle studies of LiBH4-CaH2 composite," *International journal of hydrogen energy*, vol. 35, no. 13, pp. 6578–6582, 2010.

[80] S.-A. Jin, J.-H. Shim, Y. W. Cho, K.-W. Yi, O. Zabara, and M. Fichtner, "Reversible hydrogen storage in LiBH 4–Al–LiH composite powder," *Scripta materialia*, vol. 58, no. 11, pp. 963–965, 2008.

[81] P. Mauron, M. Bielmann, A. Remhof, A. Z?ttel, J.-H. Shim, and Y. W. Cho, "Stability of the LiBH4/CeH2 composite system determined by dynamic PCT measurements," *The Journal of Physical Chemistry C*, vol. 114, no. 39, pp. 16801–16805, 2010.

[82] J.-H. Shim, J.-H. Lim, S.-u. Rather, Y.-S. Lee, D. Reed, Y. Kim, D. Book, and

Y. W. Cho, "Effect of hydrogen back pressure on dehydrogenation behavior of LiBH4-based reactive hydride composites," *The Journal of Physical Chemistry Letters*, vol. 1, no. 1, pp. 59–63, 2009.

[83] J. Mao, Z. Guo, H. Liu, and X. Yu, "Reversible hydrogen storage in titanium-catalyzed LiAlH4–LiBH4 system," *Journal of Alloys and Compounds*, vol. 487, no. 1, pp. 434–438, 2009.

[84] D. Blanchard, Q. Shi, C. Boothroyd, and T. Vegge, "Reversibility of Al/Ti modified LiBH4," *The Journal of Physical Chemistry C*, vol. 113, no. 31, pp. 14059–14066, 2009.

[85] Q. Shi, X. Yu, R. Feidenhansl, and T. Vegge, "Destabilized LiBH4-NaAlH4 mixtures doped with titanium based catalysts," *The Journal of Physical Chemistry C*, vol. 112, no. 46, pp. 18244–18248, 2008.

[86] D. Liu, Q. Liu, T. Si, Q. Zhang, F. Fang, D. Sun, L. Ouyang, and M. Zhu, "Superior hydrogen storage properties of LiBH4 catalyzed by Mg(AlH 4)2," *Chemical Communications*, vol. 47, no. 20, pp. 5741–5743, 2011.

[87] D. Liu, C. Gao, Z. Qian, T. Si, and Q. Zhang, "Reversible hydrogen storage in LiBH4/Ca(AlH 4)2 systems," *international journal of hydrogen energy*, vol. 38, no. 8, pp. 3291–3296, 2013.

[88] M. Aoki, K. Miwa, T. Noritake, G. Kitahara, Y. Nakamori, S. Orimo, and S. Towata, "Destabilization of LiBH4 by mixing with LiNH2," *Applied Physics*

A, vol. 80, no. 7, pp. 1409–1412, 2005.

[89] F. E. Pinkerton, G. P. Meisner, M. S. Meyer, M. P. Balogh, and M. D. Kundrat, "Hydrogen desorption exceeding ten weight percent from the new quaternary hydride Li3BN2H8," *The Journal of Physical Chemistry B*, vol. 109, no. 1, pp. 6–8, 2005.

[90] Y. E. Filinchuk, K. Yvon, G. P. Meisner, F. E. Pinkerton, and M. P. Balogh, "On the composition and crystal structure of the new quaternary hydride phase Li4BN3H10," *Inorganic chemistry*, vol. 45, no. 4, pp. 1433–1435, 2006.

[91] G. P. Meisner, M. L. Scullin, M. P. Balogh, F. E. Pinkerton, and M. S. Meyer, "Hydrogen release from mixtures of lithium borohydride and lithium amide: a phase diagram study," *The Journal of Physical Chemistry B*, vol. 110, no. 9, pp. 4186–4192, 2006.

[92] F. E. Pinkerton, M. S. Meyer, G. P. Meisner, and M. P. Balogh, "Improved hydrogen release from LiB0.33N0.67H2.67 with noble metal additions," *The Journal of Physical Chemistry B*, vol. 110, no. 15, pp. 7967–7974, 2006.

[93] F. Pinkerton and M. Meyer, "Hydrogen desorption behavior of nickel-chloride-catalyzed stoichiometric Li4BN3H10," *The Journal of Physical Chemistry C*, vol. 113, no. 25, pp. 11172–11176, 2009.

[94] X. Zheng, Z. Xiong, Y. Lim, G. Wu, P. Chen, and H. Chen, "Improving effects of LiH and co-catalyst on the dehydrogenation of Li4BN3H10," *The Journal*

of Physical Chemistry C, vol. 115, no. 17, pp. 8840–8844, 2011.

[95] C. C. Koch, "Synthesis of nanostructured materials by mechanical milling: problems and opportunities," *Nanostructured Materials*, vol. 9, no. 1, pp. 13–22, 1997.

[96] L. Zaluski, A. Zaluska, and J. Ström-Olsen, "Nanocrystalline metal hydrides," *Journal of alloys and compounds*, vol. 253, pp. 70–79, 1997.

[97] A. Zaluska, L. Zaluski, and J. Ström-Olsen, "Structure, catalysis and atomic reactions on the nano-scale: a systematic approach to metal hydrides for hydrogen storage," *Applied Physics A*, vol. 72, no. 2, pp. 157–165, 2001.

[98] J. Huot, G. Liang, S. Boily, A. Van Neste, and R. Schulz, "Structural study and hydrogen sorption kinetics of ball-milled magnesium hydride," *Journal of Alloys and Compounds*, vol. 293, pp. 495–500, 1999.

[99] H. Reule, M. Hirscher, A. Weißhardt, and H. Kronmüller, "Hydrogen desorption properties of mechanically alloyed MgH2 composite materials," *Journal of Alloys and Compounds*, vol. 305, no. 1, pp. 246–252, 2000.

[100] W. C. Conner Jr and J. L. Falconer, "Spillover in heterogeneous catalysis," *Chemical Reviews*, vol. 95, no. 3, pp. 759–788, 1995.

[101] U. Roland, T. Braunschweig, and F. Roessner, "On the nature of spilt-over hydrogen," *Journal of Molecular Catalysis A: Chemical*, vol. 127, no. 1, pp. 61–84, 1997.

[102] J. Xu, X. Yu, Z. Zou, Z. Li, Z. Wu, D. L. Akins, and H. Yang, "Enhanced dehydrogenation of LiBH4 catalyzed by carbon-supported Pt nanoparticles," *Chemical Communications*, no. 44, pp. 5740–5742, 2008.

[103] J. Xu, Z. Qi, J. Cao, R. Meng, X. Gu, W. Wang, and Z. Chen, "Reversible hydrogen desorption from LiBH4 catalyzed by graphene supported Pt nanoparticles," *Dalton Transactions*, vol. 42, no. 36, pp. 12926–12933, 2013.

[104] J. Xu, X. Yu, J. Ni, Z. Zou, Z. Li, and H. Yang, "Enhanced catalytic dehydrogenation of LiBH4 by carbon-supported Pd nanoparticles," *Dalton Transactions*, no. 39, pp. 8386–8391, 2009.

[105] B. Weng, X. Yu, Z. Wu, Z. Li, T. Huang, N. Xu, and J. Ni, "Improved dehydrogenation performance of LiBH4/MgH2 composite with Pd nanoparticles addition," *Journal of Alloys and Compounds*, vol. 503, no. 2, pp. 345–349, 2010.

[106] J. Mao, Z. Guo, X. Yu, and H. Liu, "Enhanced hydrogen sorption properties in the LiBH4–MgH2 system catalysed by Ru nanoparticles supported on multiwalled carbon nanotubes," *Journal of Alloys and Compounds*, vol. 509, no. 15, pp. 5012–5016, 2011.

[107] P. Ngene, M. R. van Zwienen, and P. E. de Jongh, "Reversibility of the hydrogen desorption from LiBH4: a synergetic effect of nanoconfinement and Ni addition," *Chemical Communications*, vol. 46, no. 43, pp. 8201–8203, 2010.

[108] P. Ngene, M. H. Verkuijlen, Q. Zheng, J. Kragten, P. J. M. van Bentum, J. H. Bitter, and P. E. de Jongh, "The role of Ni in increasing the reversibility of the hydrogen release from nanoconfined LiBH4," *Faraday discussions*, vol. 151, pp. 47–58, 2011.

[109] H.-W. Li, Y. Yan, E. Akiba, and S.-i. Orimo, "Improved dehydrogenation and rehydrogenation properties of LiBH4 by nanosized Ni addition," *Materials Transactions*, vol. 55, no. 8, pp. 1134–1137, 2014.

[110] J. Xu, Y. Li, J. Cao, R. Meng, W. Wang, and Z. Chen, "Preparation of graphene-supported highly dispersed nickel nanoparticles for the improved generation of hydrogen from ball-milled LiBH4," *Catalysis Science & Technology*, vol. 5, no. 3, pp. 1821–1828, 2015.

[111] J. Mao, Z. Guo, X. Yu, and H. Liu, "Improved reversible dehydrogenation of 2LiBH4 + MgH2 system by introducing Ni nanoparticles," *Journal of Materials Research*, vol. 26, no. 09, pp. 1143–1150, 2011.

[112] J. Shao, X. Xiao, L. Chen, X. Fan, L. Han, S. Li, H. Ge, and Q. Wang, "Enhanced hydriding–dehydriding performance of a 2LiH–MgB2 composite by the catalytic effects of Ni–B nanoparticles," *Journal of Materials Chemistry A*, vol. 1, no. 35, pp. 10184–10192, 2013.

[113] S. Li, P. Jena, and R. Ahuja, "Dehydrogenation mechanism in catalyst-activated MgH2," *Physical Review B*, vol. 74, no. 13, p. 132106, 2006.

[114] O. Friedrichs, J. C. Sánchez-López, C. López-Cartes, T. Klassen, R. Bormann, and A. Fernandez, "Nb2O5 pathway effect on hydrogen sorption in Mg," *The Journal of Physical Chemistry B*, vol. 110, no. 15, pp. 7845–7850, 2006.

[115] M.-Q. Fan, L.-X. Sun, Y. Zhang, F. Xu, J. Zhang, and H.-l. Chu, "The catalytic effect of additive Nb2O5 on the reversible hydrogen storage performances of LiBH4–MgH2 composite," *International Journal of Hydrogen Energy*, vol. 33, no. 1, pp. 74–80, 2008.

[116] H. Kou, X. Xiao, J. Li, S. Li, H. Ge, Q. Wang, and L. Chen, "Effects of fluoride additives on dehydrogenation behaviors of 2LiBH 4+ MgH2 system," *international journal of hydrogen energy*, vol. 37, no. 1, pp. 1021–1026, 2012.

[117] X. Xiao, J. Shao, L. Chen, H. Kou, X. Fan, S. Deng, L. Zhang, S. Li, H. Ge, and Q. Wang, "Effects of NbF5 addition on the de/rehydrogenation properties of 2LiBH4/MgH2 hydrogen storage system," *International Journal of Hydrogen Energy*, vol. 37, no. 17, pp. 13147–13154, 2012.

[118] S. Sabitu and A. Goudy, "Dehydrogenation kinetics and modeling studies of 2LiBH4 + MgH2 enhanced by NbF5 catalyst," *The Journal of Physical Chemistry C*, vol. 116, no. 25, pp. 13545–13550, 2012.

[119] J. Mao, Z. Guo, X. Yu, and H. Liu, "Combined effects of hydrogen backpressure and NbF5 addition on the dehydrogenation and rehydrogenation kinetics of the LiBH4–MgH2 composite system," *International Journal of Hy-*

drogen Energy, vol. 38, no. 9, pp. 3650–3660, 2013.

[120] J. J. Vajo and G. L. Olson, "Hydrogen storage in destabilized chemical systems," *Scripta Materialia*, vol. 56, no. 10, pp. 829–834, 2007.

[121] Y. Zhang, W.-S. Zhang, A.-Q. Wang, L.-X. Sun, M.-Q. Fan, H.-L. Chu, J.-C. Sun, and T. Zhang, "LiBH4 nanoparticles supported by disordered mesoporous carbon: hydrogen storage performances and destabilization mechanisms," *International Journal of Hydrogen Energy*, vol. 32, no. 16, pp. 3976–3980, 2007.

[122] A. F. Gross, J. J. Vajo, S. L. Van Atta, and G. L. Olson, "Enhanced hydrogen storage kinetics of LiBH4 in nanoporous carbon scaffolds," *The Journal of Physical Chemistry C*, vol. 112, no. 14, pp. 5651–5657, 2008.

[123] Z. Fang, P. Wang, T. Rufford, X. Kang, G. Lu, and H. Cheng, "Kinetic-and thermodynamic-based improvements of lithium borohydride incorporated into activated carbon," *Acta Materialia*, vol. 56, no. 20, pp. 6257–6263, 2008.

[124] S. Cahen, J.-B. Eymery, R. Janot, and J.-M. Tarascon, "Improvement of the LiBH4 hydrogen desorption by inclusion into mesoporous carbons," *Journal of power sources*, vol. 189, no. 2, pp. 902–908, 2009.

[125] X. Liu, D. Peaslee, C. Jost, and E. Majzoub, "Controlling the decomposition pathway of LiBH4 via confinement in highly ordered nanoporous carbon," *The Journal of Physical Chemistry C*, vol. 114, no. 33, pp. 14036–14041, 2010.

[126] L. Guo, L. Jiao, L. Li, Q. Wang, G. Liu, H. Du, Q. Wu, J. Du, J. Yang,

C. Yan, *et al.*, "Enhanced desorption properties of LiBH4 incorporated into mesoporous tio 2," *International Journal of Hydrogen Energy*, vol. 38, no. 1, pp. 162–168, 2013.

[127] H. Liu, L. Jiao, Y. Zhao, K. Cao, Y. Liu, Y. Wang, and H. Yuan, "Improved dehydrogenation performance of LiBH4 by confinement into porous TiO2 microtubes," *Journal of Materials Chemistry A*, vol. 2, no. 24, pp. 9244–9250, 2014.

[128] Y. Zhao, H. Liu, Y. Liu, Y. Wang, H. Yuan, and L. Jiao, "Synergistic effects of des tabilization, catalysis and nanoconfinement on dehydrogenation of LiBH4," *International Journal of Hydrogen Energy*, 2016.

[129] H. Liu, L. Jiao, Y. Zhao, K. Cao, Y. Liu, Y. Wang, and H. Yuan, "Improved dehydrogenation performance of LiBH4 by confinement into porous TiO2 microtubes," *Journal of Materials Chemistry A*, vol. 2, no. 24, pp. 9244–9250, 2014.

[130] T. K. Nielsen, U. Bosenberg, R. Gosalawit, M. Dornheim, Y. Cerenius, F. Besenbacher, and T. R. Jensen, "A reversible nanoconfined chemical reaction," *ACS nano*, vol. 4, no. 7, pp. 3903–3908, 2010.

[131] R. Gosalawit-Utke, T. K. Nielsen, I. Saldan, D. Laipple, Y. Cerenius, T. R. Jensen, T. Klassen, and M. Dornheim, "Nanoconfined 2LiBH4–MgH2 prepared by direct melt infiltration into nanoporous materials," *The Journal of Physical Chemistry C*, vol. 115, no. 21, pp. 10903–10910, 2011.

[132] R. Gosalawit-Utke, T. K. Nielsen, K. Pranzas, I. Saldan, C. Pistidda,

F. Karimi, D. Laipple, J. Skibsted, T. R. Jensen, T. Klassen, *et al.*, "2LiBH4–MgH2 in a resorcinol–furfural carbon aerogel scaffold for reversible hydrogen storage," *The Journal of Physical Chemistry C*, vol. 116, no. 1, pp. 1526–1534, 2011.

[133] K. Wang, X. Kang, Y. Zhong, C. Hu, J. Ren, and P. Wang, "Unexpected dehydrogenation behaviors of the 2LiBH4–MgH2 composite confined in a mesoporous carbon scaffold," *The Journal of Physical Chemistry C*, vol. 118, no. 46, pp. 26447–26453, 2014.

[134] G. Xia, Y. Guo, Z. Wu, and X. Yu, "Enhanced hydrogen storage performance of LiBH4-Ni composite," *Journal of Alloys and Compounds*, vol. 479, no. 1, pp. 545–548, 2009.

[135] G. Höhne, W. Hemminger, and H.-J. Flammersheim, *Differential scanning calorimetry.* Springer Science & Business Media, 2003.

[136] NETZSCH, "Functional principle of a heat-flux DSC - https://www.netzsch-thermal-analysis.com/en/landing-pages/principle-of-a-heat-flux-dsc/."

[137] NETZSCH, "Tga 209 f1 - https://www.netzsch-thermal-analysis.com/en/products-solutions/thermogravimetric-analysis/tg-209-f1-libra/."

[138] R. E. Dinnebier, *Powder diffraction: theory and practice.* Royal Society of Chemistry, 2008.

[139] E. H. Kisi and C. J. Howard, *Applications of neutron powder diffraction*, vol. 15. Oxford University Press, 2012.

[140] ILL, "D1b instrument layout - https://www.ill.eu/instruments-support/instruments-groups/instruments/d1b/description/instrument-layout/c."

[141] B. C. Smith, *Fundamentals of Fourier transform infrared spectroscopy.* CRC press, 2011.

[142] J. Torrent and V. Barron, "Diffuse reflectance spectroscopy," *Methods of soil analysis. Part*, vol. 5, pp. 367–387, 2008.

[143] J. P. Blitz, "Diffuse reflectance spectroscopy," *Modern Techniques in Applied Molecular Spectroscopy*, pp. 185–219, 1998.

[144] T. Blach and E. Gray *Journal of Alloys and Compounds*, vol. 446447, no. 0, pp. 692 – 697, 2007. Proceedings of the International Symposium on Metal-Hydrogen Systems, Fundamentals and Applications (MH2006).

[145] L. Schlapbach and A. Züttel, "Hydrogen-storage materials for mobile applications," *Nature*, vol. 414, no. 6861, pp. 353–358, 2001.

[146] C. Lexcellent and G. Gondor, "Analysis of hydride formation for hydrogen storage: Pressure-composition isotherm curves modeling," *Intermetallics*, vol. 15, no. 7, pp. 934 – 944, 2007.

[147] J. Goldstein, D. E. Newbury, P. Echlin, D. C. Joy, A. D. Romig Jr, C. E. Lyman, C. Fiori, and E. Lifshin, *Scanning electron microscopy and X-ray microanalysis: a text for biologists, materials scientists, and geologists*. Springer Science & Business Media, 2012.

[148] V. DAnna, A. Spyratou, M. Sharma, and H. Hagemann, "FTIR spectra of inorganic borohydrides," *Spectrochimica Acta Part A: Molecular and Biomolecular Spectroscopy*, vol. 128, pp. 902–906, 2014.

[149] P. Franke, D. Neuschütz, S. G. T. E. (SGTE, *et al.*, "B-ni," in *Binary systems. Part 2: Elements and Binary Systems from B–C to Cr–Zr*, pp. 1–4, Springer.

[150] S. Gomes, H. Hagemann, and K. Yvon, "Lithium boro-hydride libh4: Ii. raman spectroscopy," *Journal of Alloys and Compounds*, vol. 346, no. 1-2, pp. 206–210, 2002.

[151] O. Teppa and P. Taskinen, "Thermodynamic assessment of NiB phase diagram," vol. 9, pp. 205–212, 03 1993.

[152] K. Nasako, Y. Ito, N. Hiro, and M. Osumi, "Stress on a reaction vessel by the swelling of a hydrogen absorbing alloy," *Journal of Alloys and Compounds*, vol. 264, no. 1-2, pp. 271–276, 1998.

[153] B. Charlas, O. Gillia, P. Doremus, and D. Imbault, "Experimental investigation of the swelling/shrinkage of a hydride bed in a cell during hydrogen absorption/desorption cycles," *international journal of hydrogen energy*, vol. 37,

no. 21, pp. 16031–16041, 2012.

[154] P. Franke, D. Neuschütz, *et al.*, "B-Si," in *Binary systems. Part 2: Elements and Binary Systems from B–C to Cr–Zr*, pp. 1–4, Springer, 2000.

[155] B. Predel, "Li-si (lithium-silicon)," in *Li-Mg–Nd-Zr*, pp. 1–3, Springer, 1997.

[156] T. Minami, *Solid state ionics for batteries*. Springer Science & Business Media, 2006.

[157] Z. Fang, L. Ma, X. Kang, P. Wang, P. Wang, H. Cheng, *et al.*, "In situ formation and rapid decomposition of Ti(BH (4))(3) by mechanical milling LiBH (4) with TiF (3)," 2009.

[158] Y. Guo, X. Yu, L. Gao, G. Xia, Z. Guo, and H. Liu, "Significantly improved dehydrogenation of LiBH4 destabilized by TiF 3," *Energy & Environmental Science*, vol. 3, no. 4, pp. 464–469, 2010.

[159] R. Olesinski and G. Abbaschian, "The B-Si (boron-silicon) system," *Bulletin of alloy phase diagrams*, vol. 5, no. 5, pp. 478–484, 1984.

[160] M. A. Abbas, D. M. Grant, M. Brunelli, T. C. Hansen, and G. S. Walker, "Reducing the dehydrogenation temperature of lithium hydride through alloying with germanium," *Physical Chemistry Chemical Physics*, vol. 15, no. 29, pp. 12139–12146, 2013.

[161] M. Van Setten and M. Fichtner, "On the enthalpy of formation of aluminum diboride, AlB2," *Journal of Alloys and Compounds*, vol. 477, no. 1, pp. L11–

L12, 2009.

[162] D. Mirković, J. Gröbner, R. Schmid-Fetzer, O. Fabrichnaya, and H. L. Lukas, "Experimental study and thermodynamic re-assessment of the Al–B system," *Journal of alloys and compounds*, vol. 384, no. 1, pp. 168–174, 2004.

[163] E. Domalski and G. Armstrong, "Heats of formation of aluminum diboride and alpha- aluminum dodecaboride," *J RES–PHYS CHEM*, vol. 71, no. 4, pp. 307–315, 1967.

[164] E. S. Domalski and G. T. Armstrong, "Heats of formation of metallic borides by fluorine bomb calorimetry," tech. rep., DTIC Document, 1964.

[165] A. Zaitsev and A. Kodentsov, "Thermodynamic properties and phase equilibria in the Si-B system," *Journal of phase equilibria*, vol. 22, no. 2, pp. 126–135, 2001.

[166] S. Gordienko, "Enthalpies of formation for boron silicides," *Powder Metallurgy and Metal Ceramics*, vol. 34, no. 11-12, pp. 660–662, 1996.

[167] T. Price, D. Grant, I. Telepeni, X. Yu, and G. Walker, "The decomposition pathways for LiBD4-MgD2 multicomponent systems investigated by in situ neutron diffraction," *Journal of Alloys and Compounds*, vol. 472, no. 1, pp. 559–564, 2009.

[168] P. Franke, D. Neuschütz, *et al.*, "B-Fe," in *Binary systems. Part 2: Elements and Binary Systems from B–C to Cr–Zr*, pp. 1–3, Springer, 2004.

[169] P. Franke, D. Neuschütz, *et al.*, "B-Co," in *Binary systems. Part 2: Elements and Binary Systems from B–C to Cr–Zr*, pp. 1–3, Springer, 2004.

[170] W. Cai, H. Wang, J. Liu, L. Jiao, Y. Wang, L. Ouyang, T. Sun, D. Sun, H. Wang, X. Yao, *et al.*, "Towards easy reversible dehydrogenation of LiBH4 by catalyzing hierarchic nanostructured CoB," *Nano Energy*, vol. 10, pp. 235–244, 2014.